Deriving Dust Properties in Star Forming Clumps: a Look Across the Perseus Molecular Cloud with Herschel and SCUBA-2

by

Michael Chun-Yuan Chen
B.Sc., University of British Columbia, 2012

A Thesis Submitted in Partial Fulfillment of the
Requirements for the Degree of

MASTER OF SCIENCE

in the Department of Physics and Astronomy

Deriving Dust Properties in Star Forming Clumps: a Look Across the Perseus Molecular Cloud with Herschel and SCUBA-2

by

Michael Chun-Yuan Chen
B.Sc., University of British Columbia, 2012

Supervisory Committee

Dr. J. Di Francesco, Co-Supervisor
(Physics and Astronomy)

Dr. D. Johnstone, Co-Supervisor
(Physics and Astronomy)

Dr. J. Willis, Co-Supervisor
(Physics and Astronomy)

Supervisory Committee

Dr. J. Di Francesco, Co-Supervisor
(Physics and Astronomy)

Dr. D. Johnstone, Co-Supervisor
(Physics and Astronomy)

Dr. J. Willis, Co-Supervisor
(Physics and Astronomy)

ABSTRACT

Herschel and JCMT surveys of nearby star-forming regions have provided excellent images of cold dust emission across several wavelengths with unprecedented dynamic range and resolutions. Here we present spectral emissivity index and temperature maps of dust in the star-forming clumps of the Perseus molecular cloud determined from fitting SEDs to the combined Herschel and JCMT observations in the 160 μm, 250 μm, 350 μm, 500 μm, and 850 μm bands, employing the technique developed by Sadavoy et al. (2013). In NGC1333, the most complex and active star-forming clump in Perseus, we demonstrate that CO line contamination in the JCMT SCUBA-2 850 μm band is typically insignificant. The derived spectral emissivity index, β, and dust temperature, T_d, ranges between 0.8 - 3.0 and 7 - 50 K, respectively. Throughout Perseus, we see indications of heating from B stars and embedded protostars, and smooth β variations on the smaller scales. The distribution of β values seen in each clump differs from one clump to another, and is in general different from the diffuse ISM values (i.e., ~ 2), suggesting that dust grain evolution is significant in star-forming clumps. We also found coincidences between low β regions and local temperature peaks as well as locations of outflows, which may provide hints to the origins of these low β value grains, and dust grain evolution in star-forming clumps in general.

Contents

List of Tables

List of Figures

ACKNOWLEDGEMENTS

I would like to thank my supervisors, James Di Francesco and Doug Johnstone, for taking me in as a student and providing me with such an exciting opportunity to do research in astronomy. I appreciate the insights and advice that they have given me, as well as their tremendous support when I struggled with my thesis writing. I would also like to extend this gratitude to my scientific collaborators, particularly the JCMT GBS team members, who have provided me with many help and insights on my project.

To my fellow graduate students, for being incredible friends who have made graduate school a very delightful place to be. I will not forget all those stimulating discussions and cookie snatching. A special thanks to Steve Mairs for being such a close and supportive friend, who has been poking star formation with a stick with me since we were undergrads.

And of course, many thanks to my supportive, loving family, who I love very much.

DEDICATION

To my loving parents, who have always been incredibly supportive of me in my pursue for science.

And to my grandma, who was excited that I got into graduate school for studying astronomy/astrophysics but did not have the chance to see me finish.

Chapter 1

Introduction

Stars are one of the most important constituents of galaxies, and consequently the Universe. They are the main source of optical light in galaxies and the main driver of chemical evolution in the Universe, converting hydrogen and helium into heavier elements such as silicon and iron, the main components of terrestrial planets, and carbon, the fundamental building block of life as we know it. To begin this process of chemical evolution, stars have to be condensed out of large bodies of gas that aggregated with the formation of galaxies. Only towards the end of stellar existence can the heavier elements produced deep inside the stars, along with the unprocessed gas, be returned into interstellar space through powerful stellar winds or supernovae before new generations of stars are formed out of the newly enriched interstellar gas. This stellar life cycle is repeated as a galaxy evolves.

Most stars in galaxies, however, are low-mass stars that live for billions of years. Given that our Universe is only around 14 billion years old, most of these stars have not yet reached the end of their existences. Thus, higher mass stars must have contributed significantly to the elemental abundances in galaxies. How they are replenished in a galaxy will depend on the star-forming rate of the galaxy. Given that stars are one of the main constituents of a galaxy, and potential hosts for planets, a detailed knowledge of star-forming processes will have profound impact on our understanding of the chemical and structural evolution of galaxies, as well as the origin of our own planet and other potentially habitable planets.

In the simplest picture, stars are formed out of the densest and coldest gas of a molecular cloud, the largest unit of molecular gas in a galaxy. When a gravitationally bounded sub-structure within the cloud can no longer support itself against its own weight, it will either fragment into smaller structures or collapse directly into a

very compact and opaque object, depending on the initial conditions of the original structure. If the total mass collapsed onto the compact object is enough to support the nuclear fusion of protons into nuclei of helium-4 (i.e., hydrogen burning) in its centre, i.e., $\gtrsim 0.07$ $M_\odot$, then a star will be formed. If the compact object fails to reach this minimum mass requirement for hydrogen burning, then it will end up as a brown dwarf (or a planet under certain definitions).

In working towards a complete star formation theory, we aim to answer many key questions such as:

1. Is there a threshold for star formation, such as a minimum gas density, and what determines the efficiency at which gas above this threshold forms into stars?

2. How do star-forming environments vary, and how does this affect star formation? Does star formation affect its own environment significantly and thus is it a self-regulating process?

3. Why do galaxies preferentially favor the production of lower mass stars in a very specific distribution, i.e., the initial mass function (IMF)? What are the underlying physics responsible for this distribution?

4. What determines whether stars form in clusters or in isolation, and whether clusters will stay bound after their formation?

5. How do circumstellar disks form and evolve with star formation, and what initial conditions do they provide for planets to form within them?

A critical step towards answering these questions is to determine the masses of star-forming structures accurately, allowing us to derive the gravitational stability parameters for these structures and to estimate their associated star formation efficiencies. In this thesis, we address this topic by investigating thermal dust emission, one of the most important tracers of star-forming structures, in a nearby molecular cloud. By modelling the spectral energy distribution (SED) of the emission, we derive temperatures, optical properties, and column densities of the dust within star-forming structures simultaneously to provide accurate mass estimates. Specifically, we probe the potential evolution of star-forming environments by studying the variation of derived optical properties in various star-forming regions across a cloud.

1.1 Molecular Cloud Structure

Molecular clouds are the largest reservoirs of cold gas in a galaxy. They are typically 0.1 - 100 pc in size and $10^3 - 10^6$ $M_\odot$ in mass. In our own Milky Way, these molecular clouds can make up $\sim 10-20\%$ of the galactic disk by mass (Shull & Beckwith 1982). The mean density of a molecular cloud is typically $n \sim 10^2$ cm^{-3}, but densities in some compact regions can be orders of magnitude higher. While these densities are extremely low by any terrestrial standards, they are still very "dense" in comparison to the typical densities in the interstellar medium (ISM) which are ~ 1 cm^{-3}. Molecular clouds tend to be relatively cool, typically having temperatures of < 50 K, due to being well shielded from the interstellar radiation field (ISRF) by the dust within the cloud, and being radiatively cooled through thermal dust emission and molecular line emission (Stahler & Palla 2005).

The structure of a molecular cloud is complex and hierarchical in nature. While molecular clouds have been observed to be self-similar on larger scales (e.g., Bazell & Desert 1988; Williams et al. 2000), such behavior breaks down in gravitationally bounded regions which Williams et al. defined as clumps, the sites of star-cluster formation. On the next scale below clumps, many prominent, parsec-scale filamentary structures have been found in star-forming clouds (e.g., Bally et al. 1987; Abergel et al. 1994; Cambrésy 1999), and recent surveys with the Herschel Space Observatory have also revealed that filaments, typically $\gtrsim 1$ pc in length and ~ 0.1 pc in width, are ubiquitous within molecular clouds (e.g., André et al. 2010; Men'shchikov et al. 2010). At still smaller scales, there exist dense cores which are typically 0.01 - 0.1 pc, a few solar masses, and ~ 10 K. Towards the centre of dense cores, the density can reach as high as 10^6 cm^{-3} while the temperature drops to ~ 7 K. Recent Herschel studies have discovered that gravitationally bounded cores and deeply embedded young stellar objects (YSOs) are preferentially found inside filaments (e.g., Men'shchikov et al. 2010), suggesting filaments play an important role in dense core formation.

Observations of the nearby star-forming clouds have revealed that only a very small fraction of cloud masses are turned into stars, about $\sim 5\%$ over the past 2 Myrs, and $\lesssim 30\%$ in 10 Myrs if the current star forming rate (SFR) sustains (Evans et al. 2009). Even at dense core scales, the amount of mass that goes from a collapsing core into a star is only $\sim 25\%$ (Enoch et al. 2008). Evidently, star formation is a very inefficient process, and to understand the physics that is driving such a process, we will need to be able to observe star-forming structures, environments, and dynamics

at spatial scales that are smaller than the typical size of a core. Due to the need for high spatial resolution observations, the molecular clouds that are closest to us are often the best places to study star formation.

1.2 Perseus Molecular Cloud

The Perseus molecular cloud (hereafter referred to simply as 'Perseus'), the focus of our study, is one of the closest star-forming clouds to us that is actively forming low- to intermediate-mass stars (Ungerechts & Thaddeus 1987; Sun et al. 2006). It is located in the Perseus constellation and is about 10^4 $M_\odot$ in mass. Due to Perseus' proximity to us and its star-formation activity, it has been the subject of various large survey studies (e.g., Hatchell et al. 2005; Walawender et al. 2005; Kirk et al. 2006; Jørgensen et al. 2006b; Sadavoy et al. 2014), and numerous detailed case studies (e.g., Snell & Bally 1986; Blake et al. 1995; Di Francesco et al. 2001; Pineda et al. 2011).

Perseus is found near a greater association of stars that consists of about a dozen higher mass stars (O and B type) and more than a thousand lower mass stars all younger than 6 Myr old (de Zeeuw et al. 1999). This group of stars, known as the Perseus OB 2 (Per OB2) association, represents the first generation of stars that were formed within this large star-forming complex. A recent supernova from the Per OB2 association has been driving a large expanding shell of atomic hydrogen (HI) towards its surroundings, and may potentially have trigged current star formation within Perseus, which lies within the shell. Since the eastern region of Perseus is closer to the centre of the Per OB2 association, it may be significantly influenced by the energetic activities originating from the Per OB2 association, including ionizing radiation, stellar winds, and supernovae. Most of Perseus, however, appears to be well shielded from the UV radiation fields expected from the Per OB2 association, perhaps due to the fact that the most massive stars in Per OB2 have already evolved off the main sequence (Bally et al. 2008).

Several prominent star-forming clumps in Perseus have been identified and studied in detail: IC 348, B5, NGC 1333, B1, L1448, and L1455 (Bally et al. 2008). Other clumps have also been observed in Perseus, but the number of stars that are forming out of them is small. CO observations toward Perseus have found several discrete velocity jumps across the cloud, suggesting that the eastern and western halves of Perseus are composed of at least two distinct structures (Bally et al. 2008).

IC 348 and B5 are located in the eastern portion of Perseus, about 320 pc from

the Sun (Herbig 1998). IC 348 contains several hundred young stars which have a mean age of $\sim$ 2 Myr (Muench et al. 2003). IC 348 has a relatively low fraction of circumstellar disks compared to other star-forming clumps (Luhman et al. 1998), and has a low number of active outflows, suggesting that IC 348 is relatively old and may be at the end of its star-forming phase. The fact that IC 348 is closer to the centre of the Per OB2 association relative to most of the Perseus clumps suggests that its star formation was first triggered by the expanding shell before the shell reached the western portion of the overall cloud.

NGC 1333, B1, L1448, and L1455 are located on the western portion of the Perseus cloud, and are about 220 pc away from us (Cernis 1990; Hirota et al. 2008). NGC 1333, containing $\sim$ 150 stars, is currently the most active star-forming clump in Perseus. It is also one of the best studied star-forming sites within 500 pc of the sun, containing an extremely young cluster of low and intermediate mass (Lada et al. 1996). Due to its activity, NGC 1333 is not only rich in YSOs and dense cores, but also energetic phenomena such as outflows, shock fronts, and masers. The complexity and crowdedness of NGC 1333 can make the study of individual objects or phenomena fairly difficult due to confusion. Nevertheless, the study of NGC 1333 has been very useful in understanding the collective effect of clustered star formation and uncovering how feedback may impact the local star-forming environment, leading to the self-regulation of star formation. In particular, studies of outflows in NGC 1333, and Perseus in general, have revealed a great deal about the contributions of outflows to the overall turbulent motions of a star-forming clump (Bally et al. 2008).

1.3 Tracing the Gas Structures

Molecular clouds are mostly made of molecular hydrogen (H_2). We, however, cannot observe H_2 directly because it emits very poorly in molecular clouds. The typical temperatures within a molecular cloud ($T \sim 10 - 60$ K) are generally insufficient to excite H_2 molecules to induce rotational emission, especially given that H_2 has a very low mass. While carbon monoxide (CO) is abundant in clouds (relative to other molecules, at least) and emits very strong lines, it is only a good tracer of cloud structure over a limited range of column densities (i.e., density integrated along the line-of-sight). In low column density environments, CO could either be photo-dissociated due to inadequate shielding from the ISRF, or not sufficiently excited to emit due to low density. At high column densities, on the other hand, CO emission

can become optically thick very quickly and thus one is unable to trace its emission deeply into gas structures. The emission lines of other molecular species could in principle be used, but molecular abundances can vary from place to place and the excitations of various lines are also density dependent.

Dust, primarily silicates and carbonaceous grains (Draine 2003) less than a micron in size (Draine & Lee 1984), only makes up about 1% of the ISM by mass (Goldsmith et al. 1997). Despite this small mass contribution, however, dust is a very important player in regulating radiative processes within a cloud. Dust opacities at shorter wavelengths tend to be high, making molecular clouds appear dark against background star light. Such extinction allows the cloud structure and column density to be mapped at typically low ($\sim 5'$) resolutions over large areas of sky (e.g., Lada et al. 1994; Cambrésy 1999; Alves et al. 2001). Since dust opacities are lower at longer wavelengths, dust emission is usually optically thin in the sub-millimetre and longer wavelengths. This property allows sub-millimetre dust emission to be an excellent tracer of gas structure in molecular clouds, but especially in the coldest ($\sim$ 10 K) star-forming structures since thermal emission from such cold material peaks in the sub-millimetre regime. With the recent technological breakthroughs in sub-millimetre instrumentation (i.e., bolometric cameras) many large-scale sub-millimetre continuum surveys of star-forming regions have been conducted in recent decades (e.g., Johnstone & Bally 1999; Ward-Thompson et al. 2007; André et al. 2010).

1.4 Modified Blackbody Radiation and Dust Opacity

At sub-millimetre and millimetre wavelengths, the optical depths towards star-forming clumps are much less than unity and thus such emission is optically thin. In that regime, we can approximate the thermal dust emission with an optically thin, isothermal modified blackbody curve:

$$I_\nu = \kappa_\nu B_\nu(T_d)\Sigma \tag{1.1}$$

where Σ is the gas mass column density, κ_ν is the opacity at frequency ν, and B_ν is the blackbody function at the dust temperature T_d:

$$B_\nu(T_d) = \frac{2h\nu^3}{c^2}\left[\exp\left(\frac{h\nu}{k_B T}\right) - 1\right]^{-1}. \tag{1.2}$$

The constants h, c, and k_B are the Planck constant, the speed of light, and the Boltzmann constant, respectively. The frequency dependency of dust opacity is often modelled as a power law over sub-millimetre and millimetre wavelengths, i.e.,

$$\kappa_\nu = \kappa_{\nu_0}\left(\nu/\nu_0\right)^\beta. \tag{1.3}$$

The value of the emissivity spectral index, β, is dependent on the physical properties of the grains. If the spectral energy distribution (SED) of dust emission can be well sampled with multi-wavelength observations, Equation 1.1 and 1.3 can be used to derive simultaneously the dust temperature, mass column density, and β by assuming a reference dust opacity κ_{ν_0}. With some simple geometric assumptions, the total mass and gravitational stability of gas structures can be derived from the mass column density and temperature. Therefore modelling the thermal dust emission well can have a profound impact on our understanding of the structure and stability of star-forming gas.

In the absence of well-sampled SEDs, a β value of 2 for the ISM has commonly being adopted in the literature, motivated by both observations (e.g., Hildebrand 1983) and models (e.g., Draine & Lee 1984). Observations of protostellar disks, however, have found $\beta \simeq 1$ (e.g., Beckwith & Sargent 1991), indicating that these β values must have evolved with the dust at some point during the star-forming process as the dust and gas flow from the ISM into protostellar systems. Indeed, β values of $1 \lesssim \beta \lesssim 3$ have been reported in many observations of star-forming regions on smaller scales (~ 0.1 pc; e.g., Shirley et al. 2005, 2011; Friesen et al. 2005; Kwon et al. 2009; Schnee et al. 2010), as well as a few lower resolution observations on larger scales (e.g., Dupac et al. 2003; Planck Collaboration XXV et al. 2011).

To first order, the larger a dust grain is, the lower its β value will be. Photons of wavelength comparable to or greater than the size of the dust grain have less accessible modes of emission than their shorter wavelength counterparts have, and thus are less likely to be emitted. As the size of the dust grain increases, however, emission of longer wavelength photons becomes correspondingly easier. Hence, the emissivity, or rather,

the opacity at a given wavelength increases with grain size. Low β values observed towards protoplanetary disks, for example, have often been interpreted as evidence of grain growth through dust coagulation (Miyake & Nakagawa 1993; Mannings & Emerson 1994; Henning et al. 1995).

In reality, the value of β can also depend on various other factors such as grain composition, morphology, and surface structure. The growth of an ice mantle on the surface of dust grains, for example, can push β upwards (e.g., Aannestad 1975), as opposed to the downward trend in β expected from the growth of a bare grain. While icy fluffy silicate grains (e.g., Kruegel & Siebenmorgen 1994) and silicate or graphitic grains (e.g., Draine & Lee 1984), which are expected in cold environments, can have $\beta \sim 2$, silicate, porous graphite, or amorphous carbon grains, which are expected in the warmer regions, could give rise to $\beta \sim 1$ (Mathis & Whiffen 1989). In addition, laboratory measurements have found that β can be intrinsically temperature dependent (e.g., Agladze et al. 1996; Mennella et al. 1998; Boudet et al. 2005), further complicating the expected behavior of β.

Much like β , the reference dust opacity κ_{ν_0} also depends on the physical properties of the dust grain. In some detailed models, κ_{ν_0} can vary by as much as a factor of seven (e.g., Ossenkopf & Henning 1994). Since β and κ_{ν_0} are both the optical properties of dust, being able to measure β precisely can provide some constraints on κ_{ν_0} based on models. Furthermore, if the column density can be measured independently through observations of dust extinction, then κ_{ν_0} can also be estimated from Equation 1.1 and 1.3, provided that β and T_d are themselves well measured.

1.5 Constraining Spectral Emissivity Index

As mentioned earlier in Section 1.4, many prior studies that attempted to measure T_d and column densities with thermal dust emission have assumed a β value ~ 2 when their data have been insufficient to constrain β. If the true β value associated with the observed emission is significantly different from 2, e.g., due to grain evolution, then T_d and column density derived from such SED fitting will be erroneous. Being able to determine β accurately is thus very beneficial for improving the accuracy of the T_d and column density measurements. While the flux ratio taken from observations made at two different wavelengths can be used to derive T_d using Equation 1.1 without having to deal with column density, a prior assumption on β is still needed, and vice versa if the aim is to measure β. Therefore, being able to have a set of multi-wavelength

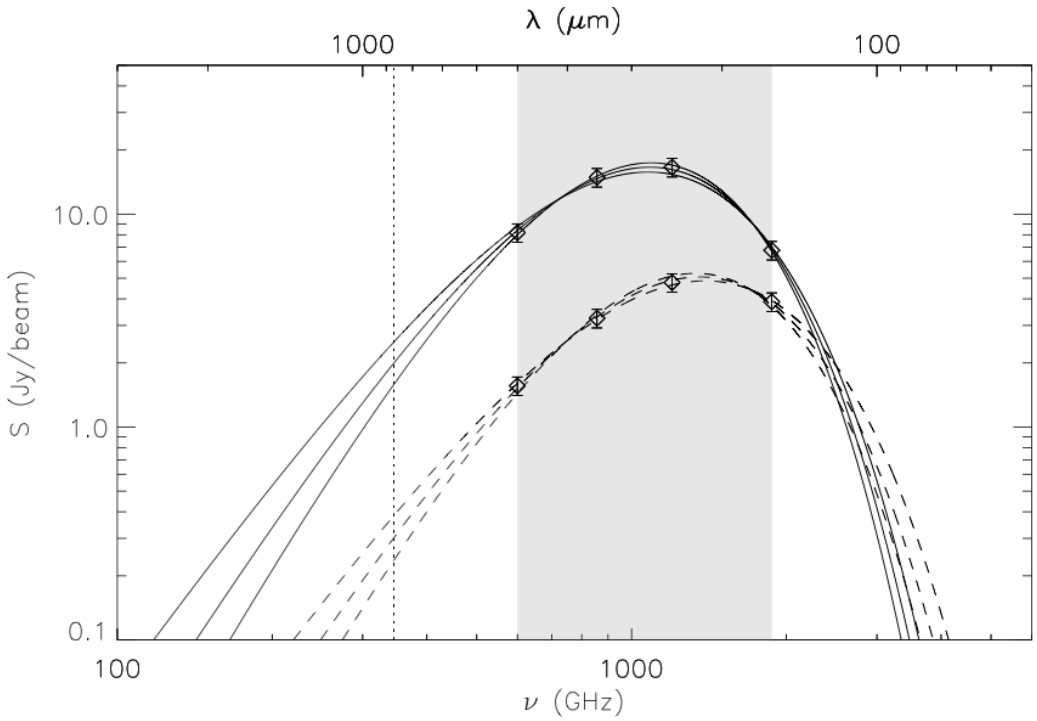

Figure 1.1 Examples of model SEDs based on Herschel data, represented by the diamonds, fit with various modified blackbody curves (Sadavoy et al. 2013, Figure 5). The temperatures and β values of the model SEDs are $T_d = 10$ K and $\beta = 2.25$ (top) and $T_d = 14$ K and $\beta = 1.75$ (bottom). The modified blackbody curves (dash for $T_d = 10K$; solid for $T_d = 14K$) have β values of 1.5, 2.0, and 2.5 starting from the left to the right. The shaded area represents the wavelength coverage of the Herschel 160-500 μm bands, and the vertical dotted line corresponds to the wavelength of the JCMT 850 μm band.

observations that is sufficient to constrain β is highly desirable.

Herschel observations of nearby molecular clouds have provided unprecedented views of star-forming regions at far-infrared and sub-millimetre wavelengths, both in terms of the dynamic range and the areal coverage of the data (André et al. 2010). Due to the high opacity of the Earth's atmosphere at wavelengths of $\sim$ 70 μm - 500 μm, similar observations cannot be be achieved by using ground-based telescopes. The typical temperatures found in star-forming regions are fairly low ($T_d \sim 10-20$ K), and thus the SEDs of the dust emission coming from these regions usually peak at $\sim$ 100 μm - 200 μm, within the wavelength range that the Herschel bands cover. As a result, Herschel's ability to observe simultaneously in multiple bands in the far-infrared and sub-millimetre makes it ideal for observing the dust emission of star-forming regions.

Herschel data are themselves not sufficient to constrain β. Figure 1.1 shows two examples of model SEDs observed with Herschel overlaid with a few modified blackbody curves with various β values. The temperatures of these modified blackbody curves are same as those used to synthesize the model SEDs. As can be seen, at least one longer wavelength observation in addition to the Herschel data further down the Rayleigh-Jeans tail is necessary to provide further constraints on β (Sadavoy et al. 2013). For this reason, Herschel studies usually assume $\beta = 2$ everywhere when performing SED fitting to their data to determine T_d and column densities.

The James Clerk Maxwell Telescope (JCMT) is currently the largest single-dish sub-millimetre telescope in the world and is capable of performing broadband continuum observations simultaneously in the 450 μm and 850 μm bands using SCUBA-2, the world's largest bolometer array. Not only is JCMT's $\sim 14''$ resolution at 850 μm comparable to Herschel's resolution at 160 μm ($13.5''$), JCMT has also recently performed a large survey of nearby molecular clouds that overlaps with many clouds surveyed by Herschel (Ward-Thompson et al. 2007; André et al. 2010). These two attributes make the JCMT data excellent longer-wavelength complements to the Herschel data for constraining β through SED fitting.

Sadavoy et al. (2013) did a thorough investigation on how to combine Herschel and JCMT data to constrain β using observations of the B1 star-forming clump in Perseus. In our study, we employed the best technique determined by Sadavoy et al. to combine Herschel and JCMT data and fit the SED of dust emission over the most active and complex star-forming clump in Perseus, NGC 1333. Following this investigation, we fit SEDs to dust emission over the six major star-forming clumps in Perseus to determine simultaneously the β , T_d, and column density. With this new information, we study potential β evolution as well as structures of these clumps.

Chapter 2

Observational Data

2.1 JCMT: SCUBA-2 Data

Wide-band 850 μm and 450 μm observations of Perseus were taken simultaneously with the Sub-millimetre Common User Bolometer Array 2 (SCUBA-2) instrument (Holland et al. 2013) on the James Clerk Maxwell Telescope (JCMT)[1] as part of the JCMT Gould Belt Survey (GBS) program (Ward-Thompson et al. 2007). We included observations that were taken in the SCUBA-2 science verification (S2SV) and the main SCUBA-2 campaign of the GBS program, i.e., in October 2011, and between July 2012 and February 2014 , respectively. Perseus regions were individually mapped using a standard PONG1800 pattern (Holland et al. 2013, Dempsey et al. 2013) that covers a circular region $\sim 30'$ in diameter. PONG patterns are constructed by sweeping SCUBA-2's on-sky footprint diagonally across a square region, at an angle of 45° to edges of the region, and "bouncing" off the boundaries into new trajectories until the region is filled. The process is repeated several times with the square region rotated to different angles to form a complete, roughly circular PONG.

Using previous sub-millimetre observations as references, our observations covered the brightest star-forming clumps found in Perseus, namely NGC 1333, B1, L1448, L1455, IC348, and B5. Table 2.1 shows the names and centre coordinates of the observed PONG1800 maps, along with the weather grades in which they were observed. Based on priority, each planned PONG target was observed either four times under

[1]The James Clerk Maxwell Telescope has historically been operated by the Joint Astronomy Centre on behalf of the Science and Technology Facilities Council of the United Kingdom, the National Research Council of Canada and the Netherlands Organisation for Scientific Research. Additional funds for the construction of SCUBA-2 were provided by the Canada Foundation for Innovation.

the driest conditions (Grade 1; $\tau_{225} < 0.05$) or six times under slightly less dry conditions (Grade 2; $\tau_{225} = 0.05 - 0.07$) to reach the targeted survey depth of 5.4 mJy beam^{-1} for 850 μm. The 'northern' PONG region of NGC 1333 is the only exception; it contains one extra S2SV observation made under Grade 2 weather.

Scan Name	**RA**	**DEC**	**Clump**	**Weather Grade**	**Number of Scans**
NGC1333-N	03:29:06.47	+31:22:27.7	NGC 1333	1	4
NGC1333-S	03:28:39.67	+30:53:32.6	NGC 1333	2	6
NGC1333	03:28:59.18	+31:17:22.0	NGC 1333	2	1
B1	03:33:10.75	+31:06:37.0	B1	1	4
L1448-N	03:25:24.56	+30:41:41.5	L1448	1	4
L1448-S	03:25:21.48	+30:15:22.9	L1448	2	6
L1455-S	03:27:59.43	+30:09:02.1	L1455	1	4
IC348-E	03:44:23.05	+32:01:56.1	IC 348	1	4
IC348-C	03:42:09.99	+31:51:32.5	IC 348	2	6
B5	03:47:36.92	+32:52:16.5	B5	2	6

Table 2.1 The names, centre coordinates, targeted clump names, and the weather grades of the individual observations made with the PONG1800 scan pattern. The weather grades 1 and 2 correspond to the sky opacity measured at 225 GHz of $\tau_{225} < 0.05$ and $\tau_{225} = 0.05 - 0.07$, respectively.

All SCUBA-2 data observed for the JCMT GBS program were reduced with the *makemap* task from the *Starlink* SMURF package (Version 1.5.0; Jenness et al. 2011; Chapin et al. 2013). This task iteratively models the SCUBA-2 measurements as an ensemble of various signal and noise components until the model converges. To avoid falsely modelling spurious noise as astronomical signal, the task utilizes masks to constrain models of astronomical signals to zero outside masked areas for all but the final iteration. For an initial reduction, a mask is automatically generated over pixel regions where the signal-to-noise ratio (SNR) is greater than 5 at each iteration. Once all the observations were individually reduced with these "auto-masks," we mosaicked (i.e., co-added) the reduced maps together and created an 'external' mask based on this SNR criteria with the mosaicked map. This new mask was then used for a second reduction on individual observations, and the individually reduced maps were again mosaicked to produce a final map. The 850 μm data were gridded into $6'' \times 6''$ pixels. Due to the 450 μm data being much more susceptible to atmospheric variability and thus having higher calibration uncertainties, as Sadavoy et al. (2013) found, we excluded the 450 μm data from our analysis.

We calibrated the 850 μm maps assuming a flux conversion factor (FCF) of 537 Jy beam^{-1} pW^{-1}, based on observations made with various sub-millimetre calibrators,

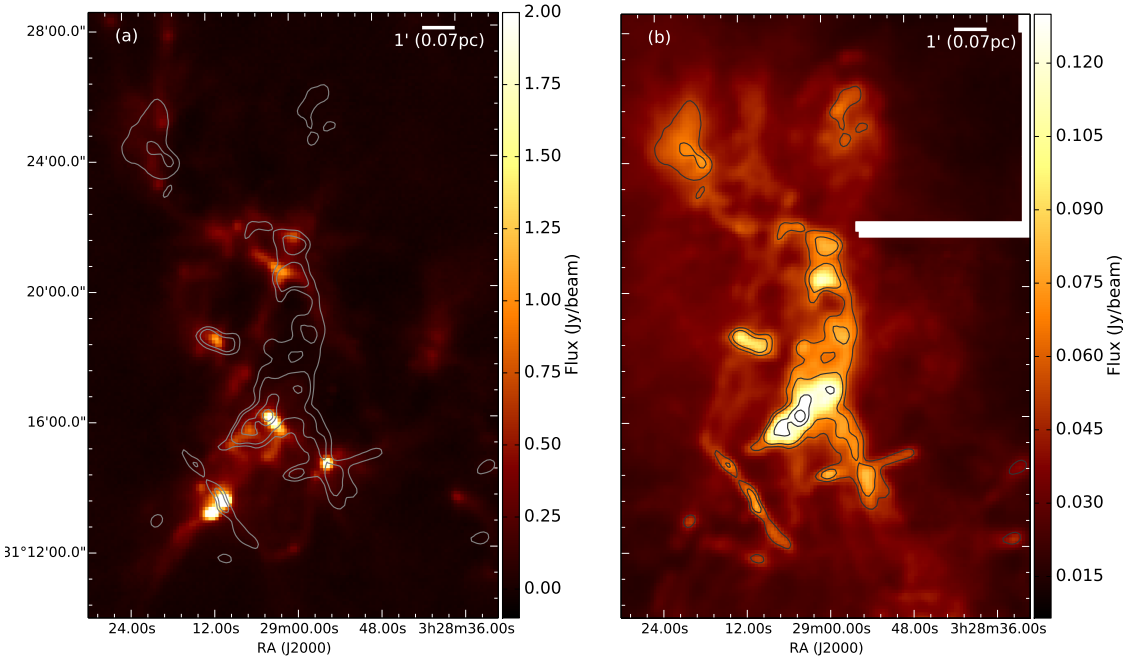

Figure 2.1 a) The SCUBA-2 850 μm map and b) the HARP integrated ^{12}CO 3-2 map of NGC 1333. Contours of spatially filtered, integrated HARP ^{12}CO 3-2 emission at levels of 15 mJy/beam, 30 mJy/beam, 80 mJy/beam, and 110 mJy/beam are overlaid on the maps.

with a calibration uncertainty of 10% throughout our maps (Dempsey et al. 2013). We adopted the effective FWHM beam size of 14.2" used by Sadavoy et al. (2013) to approximate the two Gaussian components of the JCMT beam, consistent with what Dempsey et al. (2013) found (14.1"). Our mosaic map of Perseus has a pixel-to-pixel rms noise of 4.3 mJy beam^{-1}, similar to the targeted 5.4 mJy beam^{-1} set for the JCMT GBS program (Ward-Thompson et al. 2007). Figure 2.1a shows a region of the final SCUBA-2 850 μm map of NGC 1333 as an example of our reduced SCUBA-2 data.

2.2 JCMT: HARP Data

The ^{12}CO $J = 3 - 2$ line was observed over the star-forming clumps of NGC 1333, L1448, L1455, IC348, and B1 in Perseus with the Heterodyne Array Receiver Program (HARP; Buckle et al. 2009) instrument on the JCMT. NGC 1333 was observed in 2007 January; L1448, L1448, and IC348 in December 2007; and B1 in June 2012

under good to excellent weather. The observations were made with the raster or 'basket-weaved' scan maps (Curtis et al. 2010a), split into two sub-bands with the Auto-Correlation Spectral Imaging System (ACSIS; Jenness et al. 2008; Jenness & Economou 2014). The two sub-bands were both centred at $\sim$ 345 GHz, one with a band width of $\sim$ 1 GHz consisting of 977 kHz wide channels and another with a band width of $\sim$ 250 MHz consisting of 61 kHz wide channels. For more details of the observations, see Curtis et al. 2010a and Sadavoy et al. 2013 (for B1).

The HARP data were processed with the automated data reduction pipeline *Starlink* ORAC-DR for ACSIS (Cavanagh et al. 2008; Jenness et al. 2008; Currie 2013), utilizing the SMURF package (Version 1.5.0; Jenness et al. 2011). The reduced HARP data were gridded to $6'' \times 6''$ pixels and were spatially smoothed with a $9''$ Gaussian kernel, giving the data an effective FWHM resolution of $16.8''$. The 1 GHz-wide sub-band data were smoothed and gridded into 1 km s^{-1} channels. The 1-σ RMS in these channels was found to be around 0.05 - 0.1 K. We created the integrated CO emission map using ORAC-DR by masking out the non-emission regions in the data cube and integrating the cube along the spectral axis. ORAC-DR identifies emission in the cube by clump-finding signals that are 3 times that of the 1-σ RMS noise seen in the cube that was spectrally, then spatially, smoothed. We only used the 1 GHz-wide sub-band data to create our integrated CO emission map because they have much wider channels than the 250 MHz wide sub-band data and thus have less noisy channels to perform clump-finding on. Though the 1 GHz-wide sub-band data also have a wider velocity coverage than the 250 MHz-wide sub-band, most of the clumps observed in Perseus can be sufficiently covered by the 250 MHz-wide sub-band. Our final maps are converted from the antenna temperature, T_A^* to the main-beam temperature, T_{MB}, assuming a main-beam antenna efficiency of $\eta_{MB} = 0.61$ (Buckle et al. 2009). The details of the ORAC-DR reduction recipe can be found in the online documentation of the *Starlink* software package. Figure 2.1b shows a region of the final, integrated HARP ^{12}CO 3-2 map of NGC 1333 as an example of our reduced HARP data.

2.3 JCMT: Removing CO Contamination

Wide-band observations of dust continuum emission are susceptible to molecular line contamination. For the SCUBA-2 850 μm band, the ^{12}CO J=3-2 line in particular can be a problem because it can be fairly strong and is spectrally located in the middle of the band (Johnstone et al. 2003, Drabek et al. 2012). Despite its potential to

contaminate continuum observations, Johnstone et al. found that ^{12}CO 3-2 contamination is only significant when the CO line is broadened or brightened by kinematic activity such as turbulence, outflows, or shocks. Therefore, active star-forming regions with powerful outflows are most susceptible to ^{12}CO 3-2 contamination when observed at 850 μm with SCUBA-2. Johnstone et al., however, only looked toward peaks of sources, and thus our test here will address the effect of such contamination over wider regions.

For the JCMT Gould Belt Survey (GBS), spectroscopic surveys of ^{12}CO 3-2 emission were taken with HARP over many regions also covered by SCUBA-2 observations. This spatial correspondence allowed us to compare the integrated ^{12}CO 3-2 line map with the SCUBA-2 850 μm map, which have similar angular resolutions, to assess the severity of such contamination. The two resolutions are not exactly matched because the ^{12}CO 3-2 line data were slightly smoothed spatially during data reduction.

The atmospheric transmission conditions of the two data sets, however, are not the same. First, the width of the SCUBA-2 850 μm band is much larger than the line width of the ^{12}CO 3-2 line and the transmission function varies significantly within the band as a function of wavelength. Second, the transmission function is dependent on the amount of precipitable water vapour (PWV) present in the atmosphere, and is thus dependent on the weather at the time of the observation (Drabek et al. 2012). For the GBS, this discrepancy in transmission is addressed by applying weather dependent conversion factors calculated by Drabek et al. Since the ^{12}CO 3-2 line is the dominant line that concerns SCUBA-2 at 850 μm, we refer to it from now on as "CO contamination."

On the upper limit, SCUBA-2 observations are insensitive to structures that are larger than the 8′ on-sky footprint of its bolometer array due to its inability to distinguish them from common-mode signals, such as atmospheric emission. In practice, this cutoff sensitivity is closer to 5′ due to the structures outside of the data reduction mask (over the identified astronomical signals) being 'flattened out' in the final data product. HARP observations, on the other hand, can be sensitive to larger-scale emission as the sky references are typically 1 degree from its targets. Given this difference, the HARP CO map obtained from integrating the data cube alone may significantly overestimate the levels of CO contamination in SCUBA-2 data (see Appendix A for details). To address this issue, the integrated HARP CO maps have to be spatially filtered in the same manner as the SCUBA-2 maps. We accomplished this task by artificially inserting the CO maps as negative astronomical sources into

the time series of the raw SCUBA-2 data during the map-making process. In doing so, we were able to filter spatially and remove the integrated CO emission from the SCUBA-2 map simultaneously. We retrieved the filtered CO maps by subtracting the CO-removed SCUBA-2 map from the original, reduced SCUBA-2 map. The filtered CO map was used for a detailed analysis of CO contamination levels described in Appendix A. Contours of the filtered CO map are overlaid on the SCUBA-2 850 μm map and non-filtered CO map in Figure 2.1.

2.4 Herschel: PACS and SPIRE Data

The Perseus region was observed with the PACS (Photodetector Array Camera and Spectrometer; Poglitsch et al. 2010) instrument and the SPIRE instrument (Spectral and Photometric Imaging Receiver; Griffin et al. 2010; Swinyard et al. 2010; André et al. 2010) as part of the Herschel GBS program (André & Saraceno 2005; André et al. 2010; Sadavoy et al. 2012, 2014), simultaneously covering the 70 μm, 160 μm, 250 μm, 350 μm, and 500 μm wavelengths using the parallel observing mode. The observation of the western and the eastern portions of Perseus took place in February 2010 and February 2011, respectively, covering a total area of ~ 10 deg^2. We reduced our data with the Version 10.0 of the Herschel Interactive Processing Environment (HIPE; Ott 2010) using modified scripts written by M. Sauvage (PACS) and P. Panuzzo (SPIRE) and PACS Calibration Set v56 and the SPIRE Calibration Tree 10.1. Version 20 of the Scanamorphos was used to produce the final maps, which have resolutions of $8.4''$, $13.5''$, $18.2''$, $24.9''$, and $36.3''$ in order of shortest to the longest wavelength bands. For more details on the Herschel observations of Perseus, see Pezzuto et al. (2012), Sadavoy (2013), and Pezzuto et al. (2015, in prep.). Figure 2.2 shows a region of the Herschel 160 μm and 500 μm map of NGC 1333 as examples of our reduced Herschel data.

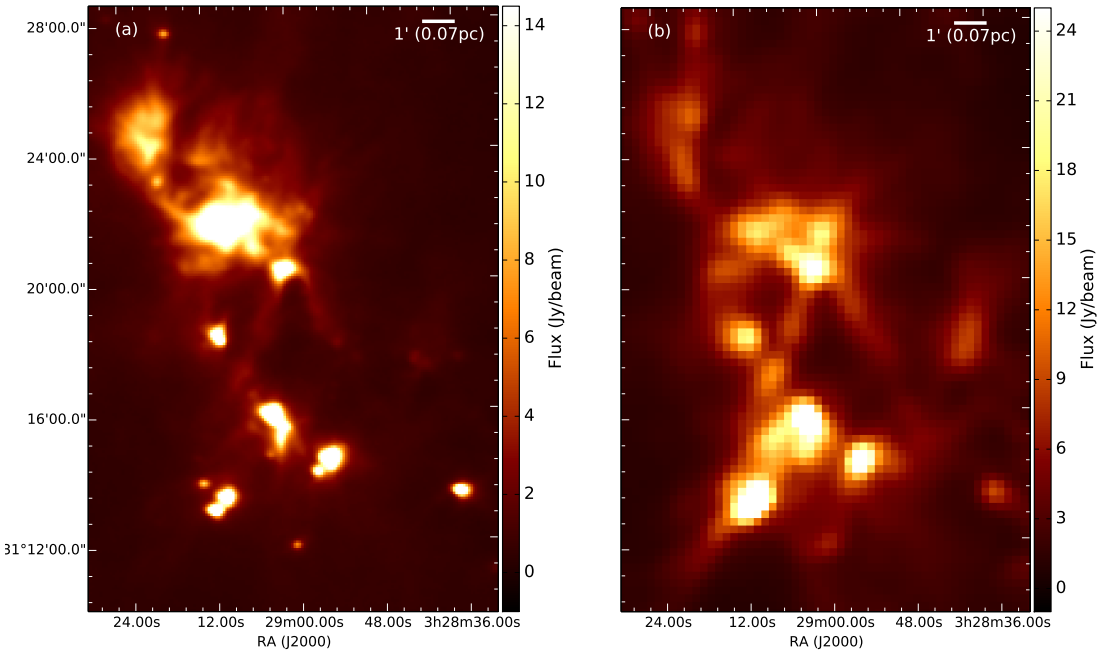

Figure 2.2 The Herschel a) 160 μm map and b) 500 μm map of NGC 1333.

2.5 Herschel: Filtering Data Spatially

Like HARP observations, Herschel observations are sensitive to larger-scale structures than SCUBA-2 observations. Unlike HARP observations, however, Herschel observations were made in space where there is no need to remove any atmospheric emission. Herschel observations, nevertheless, are insensitive to emission on scales larger than each map, and thus lower-resolution all-sky Planck data are used in most Herschel papers to recover the missing offset. Since these offsets will be removed along with other larger-scale emission when the Herschel data are filtered to match the spatial sensitivity of SCUBA-2 data, we did not apply the Planck offset to our data. The process of filtering Herschel data using the SCUBA-2 map-maker is similar to performing the CO-subtraction. In this case, we inserted a scaled Herschel-band map into the raw SCUBA-2 data stream as a 'fakemap' instead of an integrated CO map. The SCUBA-2 map-maker then spatially filters the Herschel data as a part of its standard reduction. Once the reduced SCUBA-2 map containing the Herschel data was made, we subtracted the reduced, original SCUBA-2 map from SCUBA-2 map with the Herschel insertion to obtain the filtered Herschel maps.

One assumption that is necessary for CO-subtraction and the Herschel data filtering to work is that the map-making process remains fairly linear throughout the procedure. The manner in which the map-maker is filtering the SCUBA-2 map and the fakemap should ideally be the same regardless of whether they are reduced individually or combined as a co-added map. This issue was not a significant concern for our CO-subtraction process (see section 2.3) because the CO flux calibrated to the SCUBA-2 observation is typically fairly small compared to the original flux in the SCUBA-2 map and behaves like a small perturbation in the filtering process. Since Herschel data are only inserted into the SCUBA-2 map as an intermediate step to filter spatially the Herschel data, the Herschel data do not have a specific value to which they are scaled against the 850 μm SCUBA-2 observations. Our tests detailed in Appendix B.1 show that the uncertainty associated with the choice of scaling factor is negligible relative to the intrinsic Herschel flux calibration uncertainty. For our analysis, we adopted a scaling factor of 0.1 for the Herschel filtering process.

Chapter 3

SED-fitting

After CO-subtraction and appropriate spatial filtering, we modelled our dust spectral energy distributions as a modified blackbody function in the optically thin regime in the form of

$$I_\nu = \tau_{\nu_0} \left(\nu/\nu_0\right)^\beta B_\nu(T_d) \tag{3.1}$$

where τ_{ν_0} is the optical depth at frequency ν_0, β is the dust emissivity power law index, and $B_\nu(T_d)$ is the blackbody function at the dust temperature T_d (see Equation 1.2). This particular form of modified blackbody function is slightly rearranged from Equation 1.1 and 1.3 to eliminate the need to assume a dust opacity in our SED fittings. By adopting a dust opacity value, κ_{ν_0}, the τ_{ν_0} values determined from the SED fitting can be use to derive gas column densities as the following:

$$N(H_2) = \frac{\tau_{\nu 0}}{\mu m_{H_2} \kappa_{\nu 0}} \tag{3.2}$$

where μ is the mean molecular weight of the observed gas and m_{H_2} is the mass of a molecular hydrogen in grams. For this study, we adopted a reference frequency $\nu_0 = 1$ THz (300 μm), $\mu = 2.8$, and $\kappa_{\nu_0} = 0.1$ cm^{2}g^{-1}, consistent with the assumptions made by the Herschel GBS papers. The assumed $\mu = 2.8$ comes from a cloud mass composition of 71% molecular hydrogen, 27% helium, and 2% metals (see Kauffmann et al. 2008). Our assumed κ_{ν_0} is similar to the empirically derived value used by Hildebrand (Hildebrand 1983), assuming $\beta = 2$, and is similar to the popular OH5 model (Ossenkopf & Henning 1994), which has $1.1 \lesssim \beta \lesssim 2.1$. The uncertainties associated with this assumption in deriving column density are discussed in Appendix

C.

The CO-removed SCUBA-2 data and the spatially-filtered Herschel data were convolved to a common resolution of 36.3″ to match that of the 500 μm Herschel map, the lowest of our data set. We registered and re-gridded the convolved maps to the original 500 μm Herschel map, which has 14″ × 14″ pixels. The 70 μm data were excluded from our SED fittings because that emission may trace a population of very small dust grains that are not in thermal equilibrium with the dust traced by the longer wavelength emission (Martin et al. 2012). We also did not include in the SEDs the SCUBA-2 450 μm data, which were observed simultaneously with the 850 μm data, because they are much more susceptible to atmospheric variability and have much higher calibration uncertainty (see Sadavoy et al. 2013).

PACS and SPIRE observations were calibrated under the assumption that observed SEDs have a flat νF_ν spectrum (Poglitsch et al. 2010; Griffin et al. 2010), which is quite different from modified blackbody curves. Since we cannot know a priori the shape of the SED we aim to observe, Sadavoy et al. (2013) computed a set of modified blackbody curves over a temperature range of 10 K - 15 K and a β range of 1.5 - 2.5 to calculate a set of colour corrections for the SPIRE calibration by integrating over these modified blackbody curves weighted by the relative spectral response function of each of the SPIRE filters (e.g., see Pezzuto et al. 2012). For PACS calibration, Sadavoy et al. extrapolated the suitable colour corrections from the tabulated values calculated by Müller et al. (2011)[1] using the same method. These colour correction factors, which we applied to the Herschel data, are 1.01, 1.02, 1.01, and 1.03 for 160 μm, 250 μm, 350 μm, and 500 μm, respectively. The colour uncertainties associated with these colour correction factors are 0.05, 0.008, 0.01, and 0.02, respectively.

After respective colour corrections, we fitted each pixel of the map with the modified blackbody function in Equation 3.1 using the minimization of χ^2 method to get best estimates of β, T_d, and $\tau_{\nu 0}$. The fitting was implemented in *Python* with the *optimize.curve_fit* routine from the *SciPy* software package, which uses the Levenberg-Marquardt algorithm for minimization. The flux uncertainties were calculated as the quadrature sum of the colour calibration uncertainties and the map sensitivities (see Table 3.1), and were adopted as standard errors for the χ^2 calculation. The map

[1]PACS Photometer Passbands and Color Correction Factors for Various Source SEDs, PICC-ME-TN-038, ver. 1.0,
http://herschel.esac.esa.int/twiki/pub/Public/PacsCalibrationWeb/cc_report_v1.pdf.

Band	**160 μm**	**250 μm**	**350 μm**	**500 μm**	**850 μm**
NGC 1333	50	60	30	20	30
B1	80	90	60	30	30
L1448	60	50	30	20	30
L1455	60	70	50	20	30
IC348	150	110	50	20	40
B5	60	50	30	20	20

Table 3.1 The approximate 1-σ rms noise level (mJy beam^{-1}) of the convolved, spatially filtered maps at the resolution of 36.3" for different Perseus clumps. The rms noise values were measured in a relatively emission free region of each clump's map.

sensitivities were measured individually for each Perseus clump by taking the 1-σ rms noise from the relatively empty regions in each filtered and convolved map. In addition to the colour correction uncertainties described, PACS and SPIRE also have flux calibration uncertainties of about 5% and 7% respectively. To account for the elongated Herschel beam resulting from the fast ($60''$ s^{-1}) scan rate, we followed Sadavoy et al. (2013) in adopting a conservative 10% as the flux uncertainties associated with both instruments, the same value associated with the SCUBA-2 850 μm data.

We treated uncertainties in our SED fittings by generating 1000 random flux values in each pixel following a Gaussian distribution centred on the observed flux value with a HWHM of 10%. Since flux calibration uncertainties within an instrument are correlated, we let the bands observed with the same instrument share the same set of randomly generated calibration corrections. SEDs were fitted to each pixel for every instance of random calibration offset, and the distribution of the fitted temperature and β were then fitted with a Gaussian curve to determine the best-fit temperature and β along with their calibration-based uncertainties. Unlike temperature and β, the fitted τ_{300} values have a non-Gaussian distribution. To find the best-fit τ_{300}, we performed another SED fitting with temperature and β fixed to their previously determined best-fit value. The τ_{300} and the square root of its variance obtained from the fitting was adopted as the best-fit value and uncertainties.

Chapter 4

Results: A Detailed Look at NGC1333

In this chapter, we present the T_d, β, and τ_{300} that we derived from SED fits in NGC 1333, the most active and complex star-forming clump in Perseus. In particular, we comment in detail on the morphologies of the probability and spatial distribution of these derived parameters, as well as any discernible relations between the parameters themselves. The locations of B stars, embedded YSOs, and outflows are presented in conjunction with the maps of these parameters to illustrate any spatial correlation between them. We examine critically the minimization of χ^2 method we used to fit SEDs and demonstrate that our fits are robust against noise in our data and do not introduce significant uncertainties that are correlated between derived parameters. We also present column densities estimated from the derived τ_{300}, and compare them with those derived from SED fits assuming fixed temperature and β.

In Chapter 5, we extend our analysis presented here to the rest of the five Perseus clumps and comment on the commonality and differences between all Perseus clumps, as well as any noticeable trend. In Chapter 6, we discuss these results in terms of self-regulation in star formation and evolution in dust grains.

4.1 Overall Distributions of T_d, β, and τ_{300}

Figure 4.1 shows histograms of best-fit T_d, β, and τ_{300} values derived from SED fits to all pixels with signal-to-noise ratio (SNR) greater than 10 at each wavelength associated with the NGC 1333 clump. The mean uncertainty in derived temperature

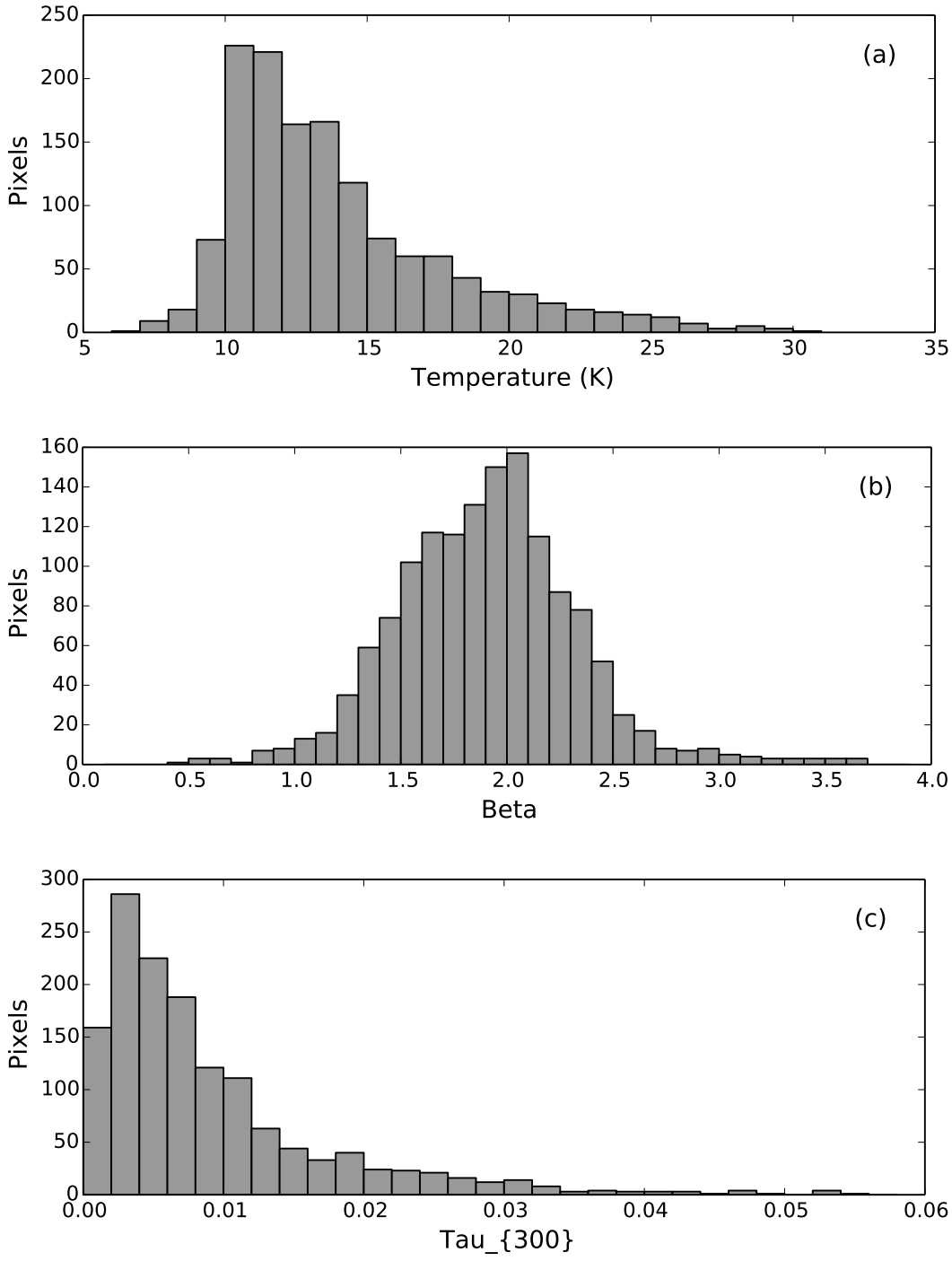

Figure 4.1 Histograms of derived a) temperature b) β, and c) τ_{300} in NGC 1333.

due to flux uncertainties is around 1 K, and the RMS noise levels were determined from relatively emission free regions of the filtered, convolved maps in each band. The dust temperature distribution of NGC 1333 peaks around 10.5 K, consistent with the common temperatures of filaments and ambient cloud material previously found in NGC 1333 (10 K; Hatchell et al. 2013) and the typical 10 K temperature of cold dense ISM seen in the literature (Evans et al. 2001). The dust temperature distribution is fairly asymmetric around the peak, however, with a sharp drop off towards the lower temperature end, and a long extended tail towards the higher temperature end.

The distribution of derived β appears Gaussian overall with a slightly skewed peak. Ignoring the skewness, the distribution appears to be centered around 1.8 and has a HWHM of ~ 0.4. The mean β uncertainty due to flux uncertainties is ~ 0.2, which is about half the width of the β distribution seen in Figure 4.1. As we demonstrate in Appendix A.1, the effect of CO contamination is fairly negligible to SED fits. Even if we conservatively assume an error of 20% for our CO flux estimates, the typical systematic uncertainty associated with such error will only be ~ 0.04 in β. With these uncertainties accounted for, it is evident that β does vary significantly over the NGC 1333 clump. The median β value of ~ 1.8 is consistent with the well-accepted OH5 model of $\beta = 1.85$ (Ossenkopf & Henning 1994). The "skewed" peak of the β distribution has a value of 2.0, which is slightly higher than than the central value of 1.8. A β value of 2 has been adopted by the widely used Hildebrand dust opacity law (Hildebrand 1983), for $\lambda > 250$ μm, based on earlier observations (Erickson et al. 1981; Schwartz 1982). Since the difference between these two β values is no larger than the flux uncertainties of β, the distinction between these two values is not significant, especially given that the HWHM of the distribution is $\sim$0.4.

Figure 4.1c shows the distribution of optical depth measured at 300 μm, τ_{300}. The distribution has a peak of 5×10^{-3} with a very rapid drop towards lower optical depths. Since our SED fitting is only performed over wavelengths where each flux value has a minimum SNR of 10, we do not expect the lower τ_{300} values to be completely sampled. The highest τ_{300} seen in the map is less than 0.06, indicating that 300 μm emission is optically thin everywhere.

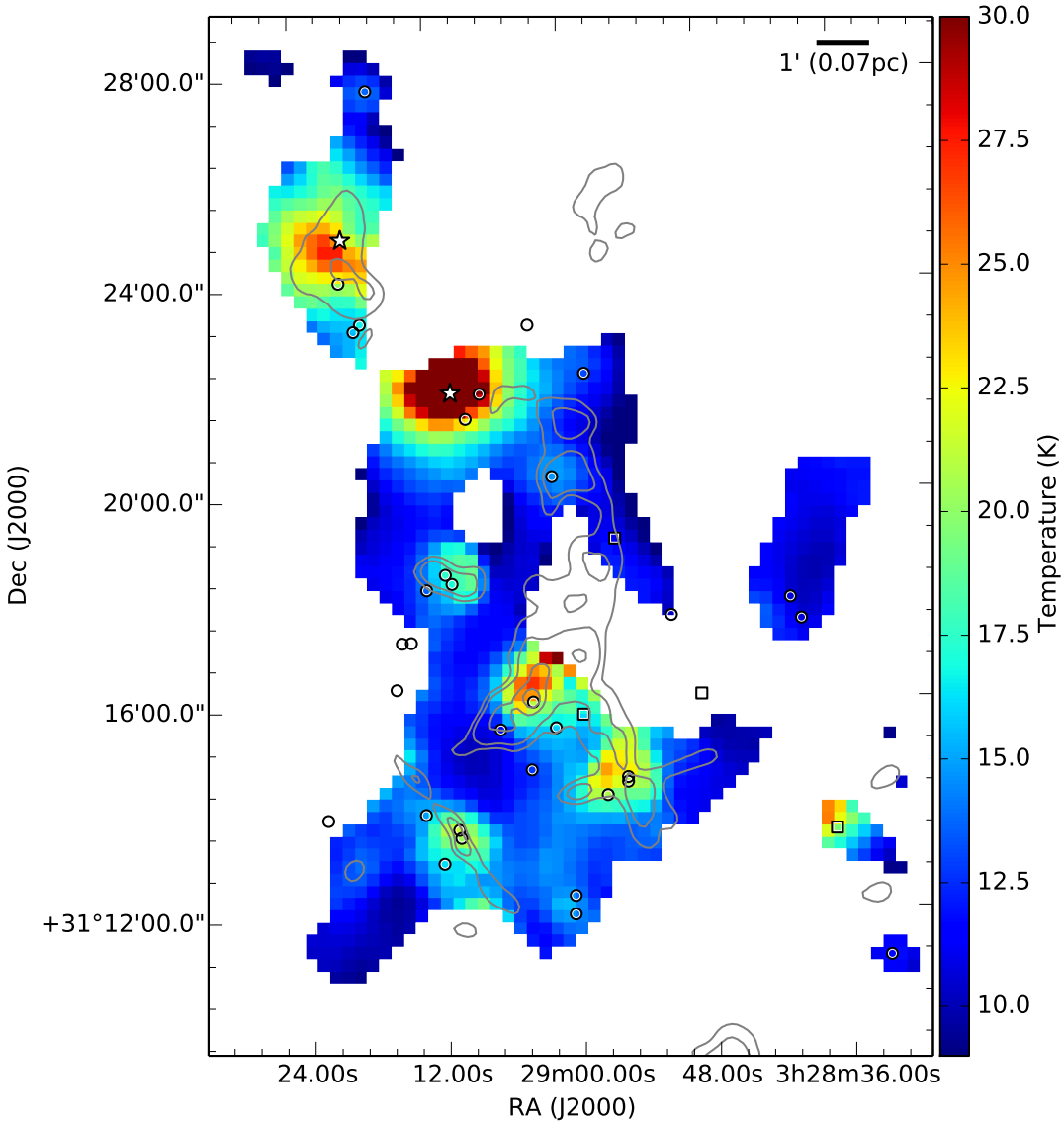

Figure 4.2 Derived dust temperatures in the NGC 1333 clump. B stars in the region are labeled with star symbols. Class 0/I and I/Flat YSOs are labelled by circles and squares, respectively. Contours of spatially filtered, integrated ^{12}CO 3-2 emission at levels of 15 mJy/beam, 30 mJy/beam, 80 mJy/beam, and 110 mJy/beam are overlaid on the map.

4.2 Local Structures

4.2.1 Local Structures: Temperature

Figures 4.2, 4.3, and 4.4 show the derived dust temperature, β, and τ_{300} in NGC 1333 overlaid with positions of embedded YSOs, B stars, and filtered, integrated CO emission. The YSOs shown here are Class 0/I and Class I/Flat protostars identified from Spitzer mid-infrared point sources in the C2D catalogue (Evans et al. 2009) or Gutermuth's catalogue (Gutermuth et al. 2009). The B star that is further to the northeast is spectrally classified as B8 and is known as BD +30 549 or NGC 1333 IRAS 9 (van den Bergh 1966; Racine 1968; Jennings et al. 1987). The other B star is known as SVS3 and is classified as B5 (Strom et al. 1976). The filtered, integrated ^{12}CO 3-2 HARP data are contoured at 15 mJy/beam, 30 mJy/beam, and 80 mJy/beam. Most of the structures seen in the filtered CO map correspond to well-known outflows in NGC 1333 (Walawender et al. 2008).

Overall, the temperature map in Figure 4.2 appears as a fairly flat region overlaid with local peaks. Almost all local peaks in the map contain at least an embedded YSO or a B star along their lines of sight, indicating local heating by these sources. The high temperature tail seen in Figure 4.1 is thus the result of local heating by these sources. Not all embedded YSOs, however, are located within local temperature peaks. This result indicates that these YSOs are either too faint, embedded, or young to have warmed their surrounding dust significantly, in agreement with Hatchell et al.'s analysis (2013). Alternatively, they could be more evolved, less-embedded YSOs misidentified as Class 0/I or Class I/F objects. Out of the 34 Class I/0 and Class I/F YSOs found within derived temperature map of NGC 1333, 14 of these YSOs are located near centers/peaks of warmer regions and 10 are unambiguously outside of these warmer regions. The remaining 10 YSOs are located within or on edges of warm regions, which make identifying these YSOs as sources of heating difficult.

As expected, Class II and III YSOs are not seen towards any of these local peaks. Class II and III YSOs are more evolved YSOs and should have no circumstellar envelope in their surroundings to heat. Class II and III YSOs typically have luminosities of $\sim 0.1 - 20$ $L_\odot$ (Ward-Thompson & Whitworth 2011). A spherical blackbody in thermal equilibrium with a 20 $L_\odot$ point source in an isolated system would have a temperature of ≤ 10 K when the two are separated by ≥ 3500 AU, i.e., $\sim 16''$ when observed in NGC 1333. For a 0.1 $L_\odot$ YSO, this distance would be only ~ 250 AU,

i.e., $\sim 1.1''$ in NGC 1333. The distance to which a Class II or III YSO can heat up its surrounding dust above the typical cold dense ISM value of 10 K is thus smaller than the typical size of a dense core (i.e. circumstellar envelope) of $\sim$ 15000 AU (i.e., $\sim 68''$ in NGC 1333). The fact we do not see any signs of heating associated with Class II or III YSOs suggests that the space surrounding these YSOs are devoid of dust. Given that there is nothing to stop a collapsing circumstellar envelope from falling towards the YSO that is embedded in it, and surrounding it in the process, the lack of dust surrounding Class II or III YSOs demonstrates that these YSOs are indeed more evolved objects that have already accreted most, if not all, of their envelopes.

Our derived temperatures do not consistently dropoff near map edges, which indicates that our temperatures are less susceptible to the edge effects seen in Hatchell et al.'s map (Hatchell et al. 2013) due to large-scale filtering of SCUBA-2 data. The central peaks of our locally heated regions are all far away from map edges, suggesting that most of the high temperature tail pixels seen in Figure 4.1 are not the result of systematic errors associated with filtering. We improved temperature derivation in NGC 1333 with respect to Hatchell et al's by using using less spatial filtering in our data reduction, and by observing with the full SCUBA-2 array instead of just one sub-array. Additionally, we have more sensitive (i.e., deeper) 850 μm observations of NGC 1333 complemented by four additional bands from Herschel.

Assuming a baseline temperature of 10 K, we found the FWHM of locally heated regions to be typically $\sim 70''$ in diameter ($\sim$5 pixels), with the exception of the region near BD +30 549, which is $\sim 112''$ ($\sim$ 8 pixels). In addition to compact regions heated by protostars, we have also found less prominent warm regions that extend from these compact regions. Some of these extensions coincide with outflows, suggesting that outflows are potentially sources of heating as well. Many of these extensions, however, sit near map edges, and may be subjected to some systematic errors associated with spatial filtering.

The temperature map outside of local temperature peaks appears relatively featureless and flat. The dust temperatures in these regions are between 9 K and 12 K, which correspond to the most common values seen in Figure 4.1a. This temperature population peaks around 10 K and accounts for about half of the overall map by area. This result is consistent with dust temperatures (Hatchell et al. 2013) and dense core ammonia temperatures (Rosolowsky et al. 2008; Schnee et al. 2009) found in NGC 1333, as well as with typical temperatures of cold dense interstellar medium (Evans et al. 2001). Interestingly, the temperatures seen towards the south-eastern end of

SVS13, along where HH7-11 are located (Herbig 1974; Herbig & Jones 1983), are locally the lowest ($\sim$ 10 K). As we discuss in Section 4.2.3, this region also has the highest τ_{300} found in NGC 1333. The low temperatures observed here likely result from dust being well shielded from interstellar radiation field (ISRF).

4.2.2 Local Structures: β

Figure 4.3 shows the map of derived β. Pixels with similar β values are found in well defined structures, and β variations larger than β uncertainties ($\sim$ 0.2) can be seen throughout the map. The lower β regions tend to resemble and coincide with heated regions seen in Figure 4.2. Nearly all the localized decreases in β correspond to a local temperature peak, but the converse is not true. Upon close examination, the local β minima also appear less circular in shape than their temperature counterparts and share a closer resemblance to some of the prominent outflows to which they coincide. The fact that similar β values tend to form well defined structures that correlate with local environments suggests that β variations seen here are not noise artifacts.

As discussed earlier and in Appendix A, the errors associated with CO subtraction are rather small compared to the β variations seen here, and thus the resemblance between some of the β minima and outflow structures is unlikely an artifact due to incomplete CO decontamination. While no study of free-free emission has been conducted over these outflows to assess whether free-free emission can be a significant contaminant in our data, free-free emission at centimetre wavelengths observed in radio jets is generally $<$ 1 mJy (Anglada 1996) and is relatively weak at 850 μm compared to the RMS noise of our 850 μm data, considering that these jets have widths much smaller than the JCMT beam. High angular resolution observations of the outflow sources SVS 13 (Rodríguez et al. 1997; Bachiller et al. 1998) and IRAS 4A (Choi et al. 2011) with the Very Large Array (VLA) have also shown that free-free emission is negligible below $\lambda \sim 3$ mm at these locations, suggesting that free-free emission is unlikely a contaminant to our data in regions near protostars.

Most of the β values at the two extremes of the β distribution in Figure 4.1b are located near map edges and may be subject to systematic errors associated with spatial filtering at these locations. Only the pixels with flux 10 times that of RMS noise in all five bands are SED fitted, and thus lower SNRs found towards edges of our mask are likely an insignificant source of error in comparison to filtering systematics. Interestingly, very low β values ($\sim$ 1) have also been found well inside the mask in

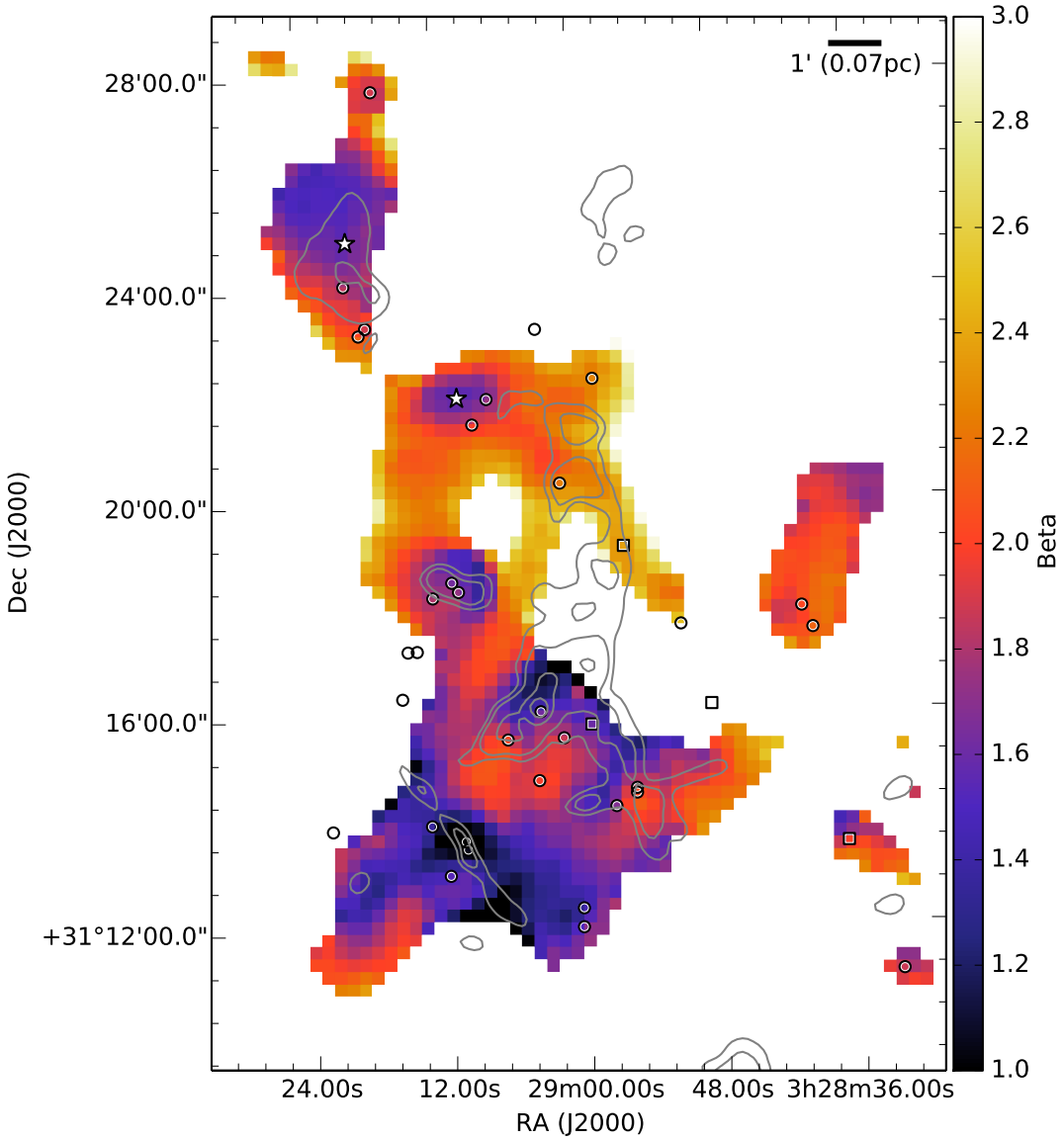

Figure 4.3 Derived β in NGC 1333 overlaid with the same symbols as in Figure 4.2.

regions surrounding the protostars IRAS 4A and B, where 4A is the source driving the most collimated outflow in NGC 1333. A significant number of pixels, $\sim$ 20%, also have β values lower than 1.5, which is significantly lower than the classically assumed value of 2 but consistent with some recent measurements (e.g. Kwon et al. 2009; Schnee et al. 2014) and within β ranges found in several studies (e.g. Dupac et al. 2003; Shirley et al. 2011).

4.2.3 Local Structures: Optical Depth

Figure 4.4 shows the NGC 1333 map of derived τ_{300} values overlaid with positions of embedded YSOs and integrated CO emission contours. Since the dust opacity we adopted is defined at 300 μm (see Section 4.3 for details), the τ_{300} values derived here are linearly proportional to column density, i.e., independent of β as long as κ_{ν_0} is constant. The column density uncertainties associated with our adopted κ_{ν_0} are discussed further in Appendix C.

Several filamentary structures containing prominent knot-like τ_{300} peaks can be seen in Figure 4.4. Most of the embedded YSOs appear to be associated with these higher τ_{300} structures, though a few are found in lower τ_{300} regions. Interestingly, many embedded YSOs found towards higher τ_{300} structures appear to be spatially offset from the actual τ_{300} peaks, often by about half a beam width. In addition, many local, lower τ_{300} regions in the map coincide with locations of CO outflow lobes, suggesting that these lower τ_{300} features were carved out by outflows, similar to what was found previously in NGC 1333 (e.g., Sandell & Knee 2001) and in L1551 (Moriarty-Schieven et al. 2006). The lower τ_{300} regions that coincide with the western lobe of the IRAS7 outflow (Liseau et al. 1988), the northwestern lobe of the SVS13 outflow (Snell & Edwards 1981), and the eastern lobe of IRAS2 outflow (Sandell et al. 1994; Bachiller et al. 1998), as traced by integrated CO emission contours in Figure 4.4, are some of the most prominent examples.

The highest τ_{300} peak in the map also coincides with the southeastern end of the bipolar outflow driven by SVS13, suggesting that the peak was formed from compressed material. The fact that HH7-11 (Herbig 1974) also coincides with this high τ_{300} region further suggests that the SVS13 outflow is colliding with higher density material at this location. The unusually cold ($\sim$ 10 K) temperature found here, in comparison to the surroundings, may be explained by high column density material in the region shielding the region's interior from the ISRF. As Sandell and Knee (2001)

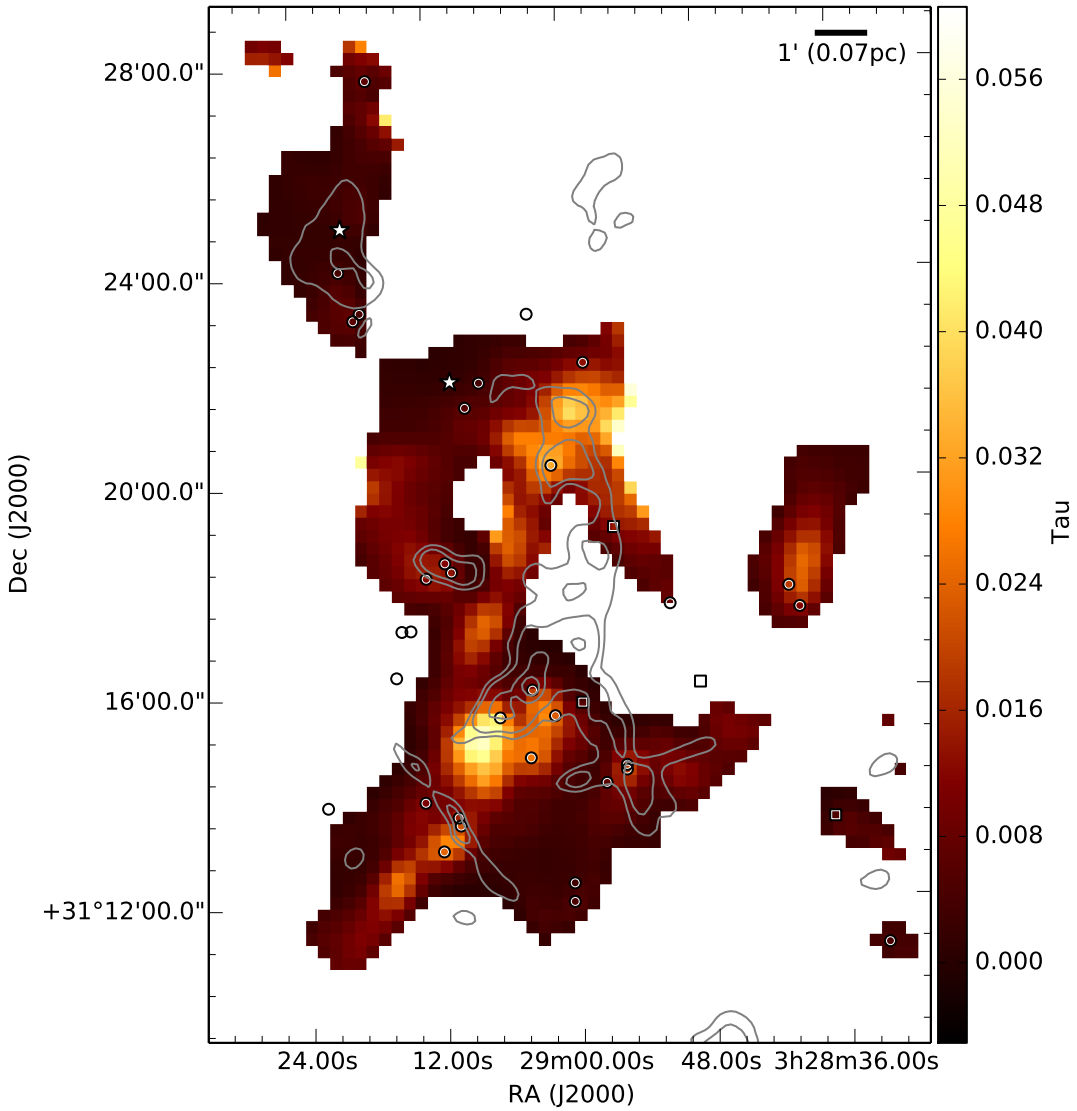

Figure 4.4 Derived optical depth, τ_{300}, in NGC 1333 overlaid with the same symbols as in Figure 4.2

found in NGC 1333 looking at large sub-millimetre cavities/shells, outflows may be a significant player in shaping local structures in NGC 1333.

4.3 Column Density Estimation

We derived column densities from the fitted τ_{300} using Equation 3.2 by adopting a dust opacity value at 300 μm, $\kappa_{300} = 0.1$ cm^{-2} g^{-1}. Based on Ossenkopf and Henning's dust model (OH5; 1994), our assumed κ_{300} has uncertainties between -20 to +200% for all ice mantle thickness assumed in OH5, and translates into column density uncertainties of -70% and $+20\%$. For more details, please refer to Appendix C.

Figure 4.5a shows the corresponding map of column density in NGC 1333 derived from SED-fitted τ_{300} values, assuming $\kappa_{300} = 0.1$ cm^{-2} g^{-1} and $\mu = 2.8$, i.e., the same values assumed in Herschel GBS papers. Figure 4.5a also shows contours of CO-subtracted SCUBA-2 850 μm emission and the locations of B stars and embedded YSOs. Since our adopted κ_ν is referenced at the same wavelength as our fitted τ_ν, the column density presented in Figure 4.5 is simply a re-scaled version of the derived τ_{300} map presented in Figure 4.4.

At first glance, the morphologies of derived column densities resemble those of 850 μm emission, indicting that sub-millimetre emission is a reasonable proxy for tracing the amount of material along a line of sight, and thus the physical structure of a cloud. The resemblance of the two, however, breaks down in regions near the two B stars where sub-millimetre emission is dominated by effects of heating rather the amount of material present. To a lesser extent, the same behavior is found in regions locally heated by embedded YSOs.

In the absence of multi-wavelength data, the column densities, and consequently masses, of star-forming structures have often been derived from observed dust emission by assuming a particular dust temperature and opacity κ_{ν_0} across a single wavelength map. When the wavelength of the adopted opacity is different from the wavelength of the single band data, a β value is assumed to extrapolate the opacity to the wavelength of the data. To understand the consequences of these assumptions, we also modelled SEDs of NGC 1333 by allowing τ_{300} to be a free parameter and fixing temperature, β, and κ_{300} at 10 K, 2.0, and 0.1 cm^{-2} g^{-1}, respectively, i.e., values commonly adopted in the literature.

Figure 4.5b shows the corresponding column density map overlaid with the same

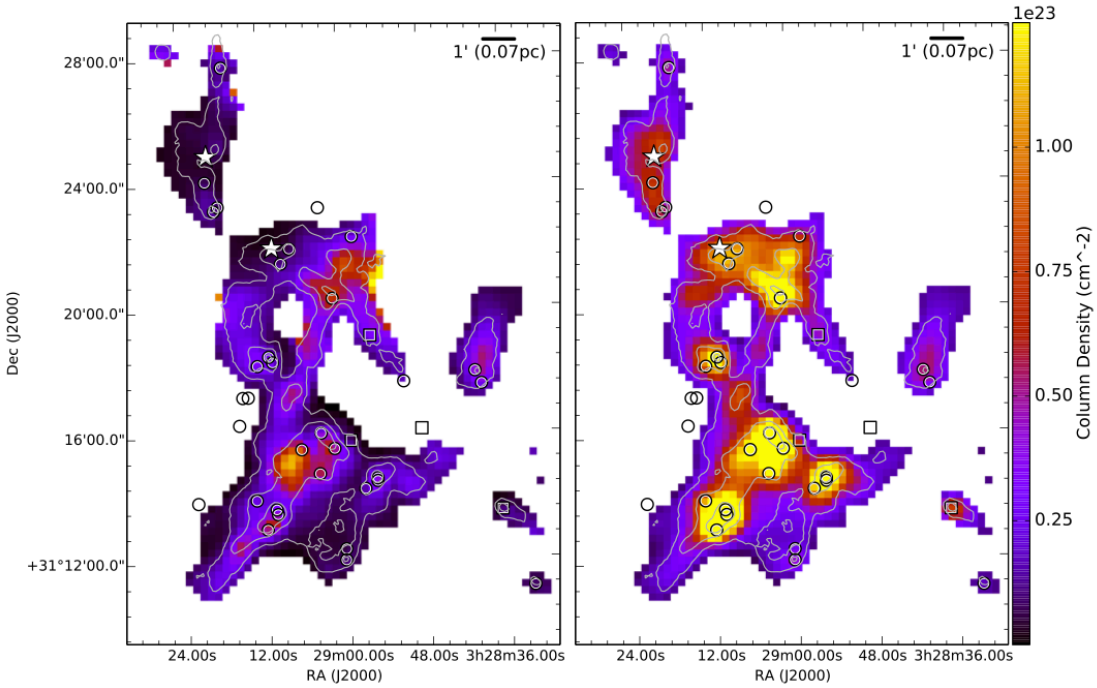

Figure 4.5 a) Column density derived from having temperature and β as free parameters and b) Column density derived from fixing temperature and β at 10 K and 2.0, respectively. Both maps are derived assuming a dust opacity $\kappa_{300} = 0.1$ cm^{-2} g^{-1}. Contours of CO-subtracted SCUBA-2 850 μm flux at 100, 300, and 900 Jy/beam are overlaid over both maps. B stars, Class 0/I YSOs, and Class I/Flat YSOs are labelled with stars, circles and squares, respectively.

contours and symbols as in Figure 4.4. The column densities derived assuming fixed temperature and β have substantially higher values than found when temperature and β are free parameters, especially at locations where derived temperatures are substantially higher than 10 K. The column densities estimated in the constant T_d and β case are typically 6 to 17 times that of the free T_d and β case towards regions heated by B stars and embedded YSOs, and about 2.5 times when averaged over NGC 1333. The morphology of derived column densities also resembles more the observed 850 μm emission in the constant T_d and β case than in the free T_d and β case. Given that our derived β values peak at the same value as our assumed $\beta = 2$, as demonstrated in Figure 4.1, most of the differences found in derived column densities are due to variations in temperature rather than β. For example, at $T_d = 10$ K, the column density estimated from $\beta = 2$ is only 6% higher than when $\beta = 1.8$, but when β is fixed at 2, the column density estimated from $T_d = 10$ K is 101% higher than when $T_d = 12$ K.

4.4 Relations between T_d, β, and τ_{300}

Figure 4.6 shows the derived β plotted against temperature for each pixel in Figure 4.2 and Figure 4.3. The distribution displays an anti-correlation at $T_d < 20$ K that gradually flattens at higher temperatures. Anti-correlation between β and T_d, however, can be an artifact of SED fitting using minimization of χ^2 method due to β - T_d degeneracy. Indeed, Shetty et al. (2009a; 2009b) demonstrated that SED fitting using the minimization of χ^2 method can lead to such an anti-correlation when modest amounts of noise are present in data, and such anti-correlations due to erroneous fittings have been noted in previous works (e.g., Keene et al. 1980; Blain et al. 2003; Sajina et al. 2006; Kelly et al. 2012; Sadavoy et al. 2013).

The anti-correlation due to β and T_d uncertainties arises naturally from both β and T_d's ability to shift the peak of a modified blackbody SED (see Equation 3.1). While β is responsible for producing the power-law slope of the SED's Rayleigh-Jeans tail, it can also shift the SED peak independent of temperature. An underestimation of β, for example, leads to a flatter power-law tail that pulls the SED peak lower in frequency. Temperature, on the other hand, shifts the SED peak through Wien's displacement law, which acts on the blackbody component of the SED. The position of the SED peak can thus be maintained at a constant value by anti-correlating β and T_d, resulting in a degeneracy in reduced χ^2 SED fitting, when the height of the SED

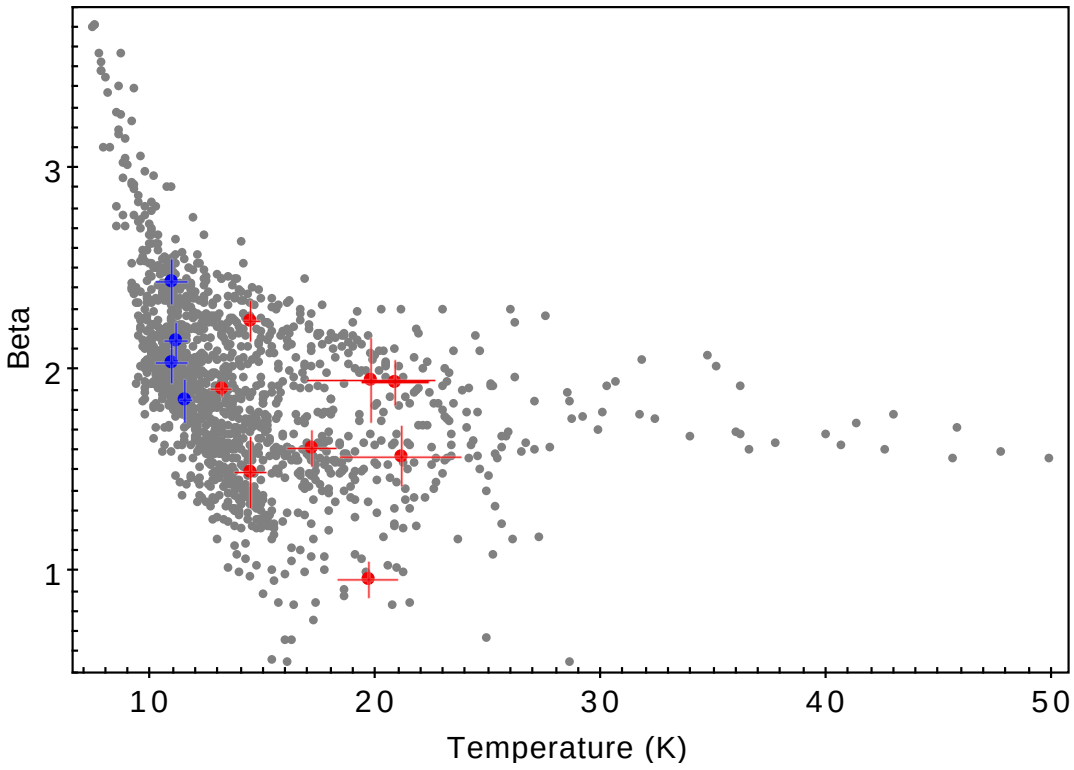

Figure 4.6 Scatter plot of derived β v.s. temperature in NGC 1333. Values of individual pixels in the region are shown in grey. The beam-averaged values at the locations of embedded YSOs are labeled in red if the YSO is located at the center of a heated region and in blue if the YSO is located in a region with no visible signs of heating. The error bars shown correspond to the standard deviation of the respective beam-averaged values.

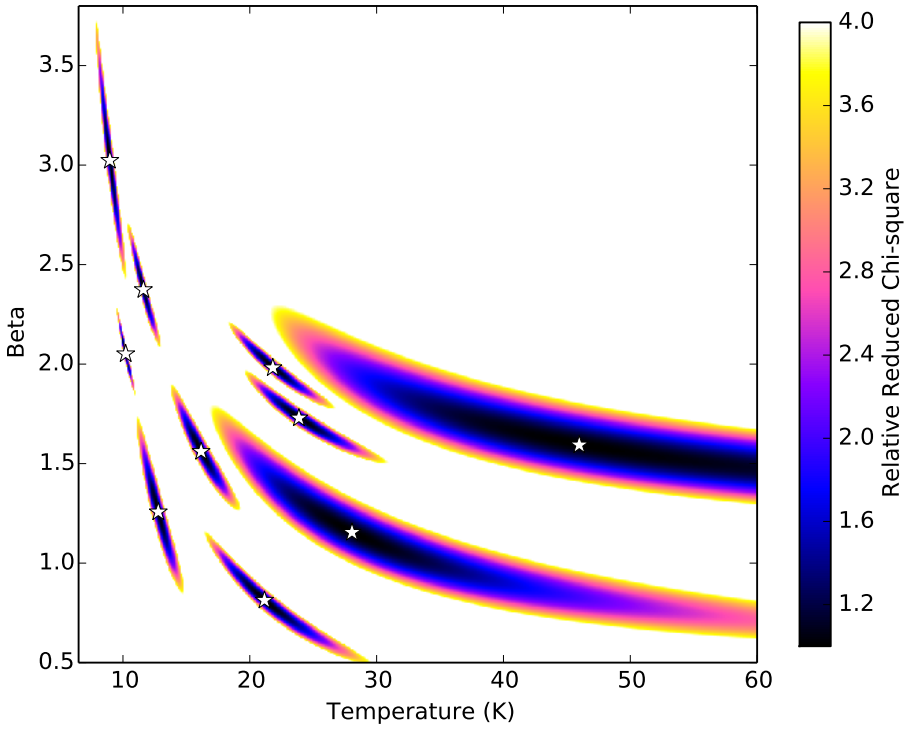

Figure 4.7 The relative reduced χ^2 values of a few pixels in the NGC 1333 SEDs fitted with a given β and temperature, and a best fitted τ_{300}. The values shown are relative to the minimum reduced χ^2 found in each pixel, and the minima of each pixel are labelled with stars. Unlike for our best-fitted SEDs, the fluxes used in these fittings are not randomly corrected to simulate calibration errors.

can be arbitrary scaled by a free τ parameter.

Figure 4.7 shows the relative reduced χ^2 contours for a few selected pixels from NGC 1333 fitted with respect to specific β and T_d and free τ_{300}. Collectively, the reduced χ^2 distributions of these pixels greatly resembles the distribution of best fitted pixels in Figure 4.6. This resemblance demonstrates that the anti-correlated shape of the β - T_d distribution seen in Figure 4.6 is significantly influenced by β - T_d degeneracy, especially in the sharp increase in β towards lower temperatures and in the flattening of β towards higher temperatures.

At lower temperatures, ~ 10 K, our observed bands well sample the SED peak but less of the Rayleigh-Jeans tail, resulting in a stronger constraint on T_d relative to β. At higher temperatures, however, the SED peak shifts upwards in frequency, causing our observed bands to sample less of the SED peak and more of the Rayleigh-Jeans tail. This sampling provides us with a stronger constraint on β relative to T_d at higher temperatures. Figure 4.7 well demonstrates such behavior. At temperatures $\gtrsim 30$ K, the χ^2 distributions seen in Figure 4.7 appears to have larger spreads in the β -T_d phase space relative to their colder counterparts. The broadening of these distributions results from SEDs being noisier at these sample pixels. In short, performing SED fits with the minimization of χ^2 method tends to result in more precise temperature estimates towards lower temperatures, and more precise β estimates towards higher temperatures.

While degeneracy plays a strong role in shaping the β - T_d distribution, the location of individual pixels' χ^2 distribution in Figure 4.7 would suggest that an underlying β - T_d correlation exists in Figure 4.6 in addition to that caused by degeneracy alone. The β and T_d uncertainties attributed from flux calibration uncertainties are typically ~ 0.2 and ~ 1 K, respectively, which are smaller than the typical β - T_d spread of χ^2 within 4 times the minimum χ^2 of each pixels in Figure 4.7. This comparison indicates that degeneracy in our fits are less severe than Figure 4.7 suggests. Even for ranges of β that are degenerate within 4 times the minimum χ^2, the variation of β within NGC 1333 is unmistakeable, given that the $4\chi^2_{min}$ contours of pixels with derived $\beta \lesssim 1.2$ do not overlap with $4\chi^2_{min}$ contours of pixels with $\beta \gtrsim 2.5$.

Figure 4.6 also shows beam-averaged values of pixels surrounding embedded YSOs. Red circles represent those YSOs found towards a local temperature peak, and blue circles represent YSOs not associated with local T_d peaks. An anti-correlation between β and temperature can be seen in these beam-averaged values as well. Overall, the cold, non-heated envelopes of embedded YSOs have higher β values than heated

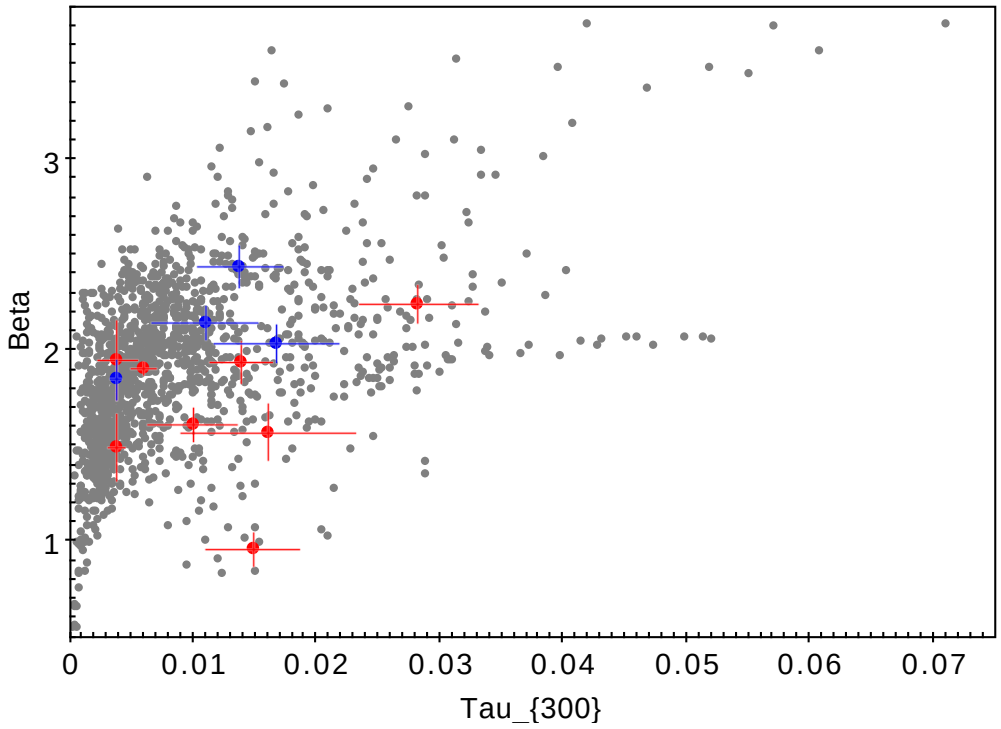

Figure 4.8 Scatter plot of derived β v.s. τ_{300} in NGC 1333. Symbols here are defined as in Figure 4.6.

envelopes of YSOs.

Figure 4.8 shows the derived β values plotted against the respective τ_{300} for each pixel in NGC 1333. The distribution appears to be mostly scattered, with perhaps a slight positive correlation. The beam-averaged values for envelopes of embedded YSOs are also fairly scattered and show no discernible trend. Interestingly, the non-heated envelopes of embedded YSOs have the same range of τ_{300} as heated envelopes, indicating that these two populations of dense cores have similar column densities, and thus masses.

Chapter 5

Results: Perseus in General

5.1 Perseus Clumps: Temperature

Having looked in detail at NGC 1333, the most active and complex star-forming clump in Perseus, we now extend our analysis to five other star-forming clumps in Perseus. Figure 5.1 shows histograms of derived temperatures in each of the Perseus clumps, namely B1, L1448, L1455, IC 348, and B5. These temperature distributions all share a characteristic shape: a primary low temperature peak and a high temperature tail. With the exception of IC 348, which has a temperature peak at $\sim$ 12 K, all clumps have their primary temperature peaks located at $\sim$ 10 K. The latter is consistent with the typical kinetic temperatures that have been observed towards dense cores in Perseus with ammonia lines (Rosolowsky et al. 2008; Schnee et al. 2009) and the isothermal dust temperature of prestellar cores in other clouds (Evans et al. 2001).

In NGC 1333, we found the higher end tail of the temperature distribution to be the result of local heating by embedded YSOs and B-stars. Since NGC 1333 and IC 348 are the only two clumps to have produced several B stars recently (Bally et al. 2008), higher temperature tails seen in other regions are likely to be from embedded YSOs. Indeed, as illustrated in temperature maps of these clumps in Figure 5.2, most local temperature peaks coincide with locations of embedded YSOs. Notably, the B1, L1455, and B5 clumps each have a prominent, secondary temperature peak $\sim 13 - 16$ K located in their high temperature tails in Figure 5.1. This temperature range agrees with the isothermal dust temperatures that Shirley et al. (2002) found towards protostellar cores containing Class 0 YSOs.

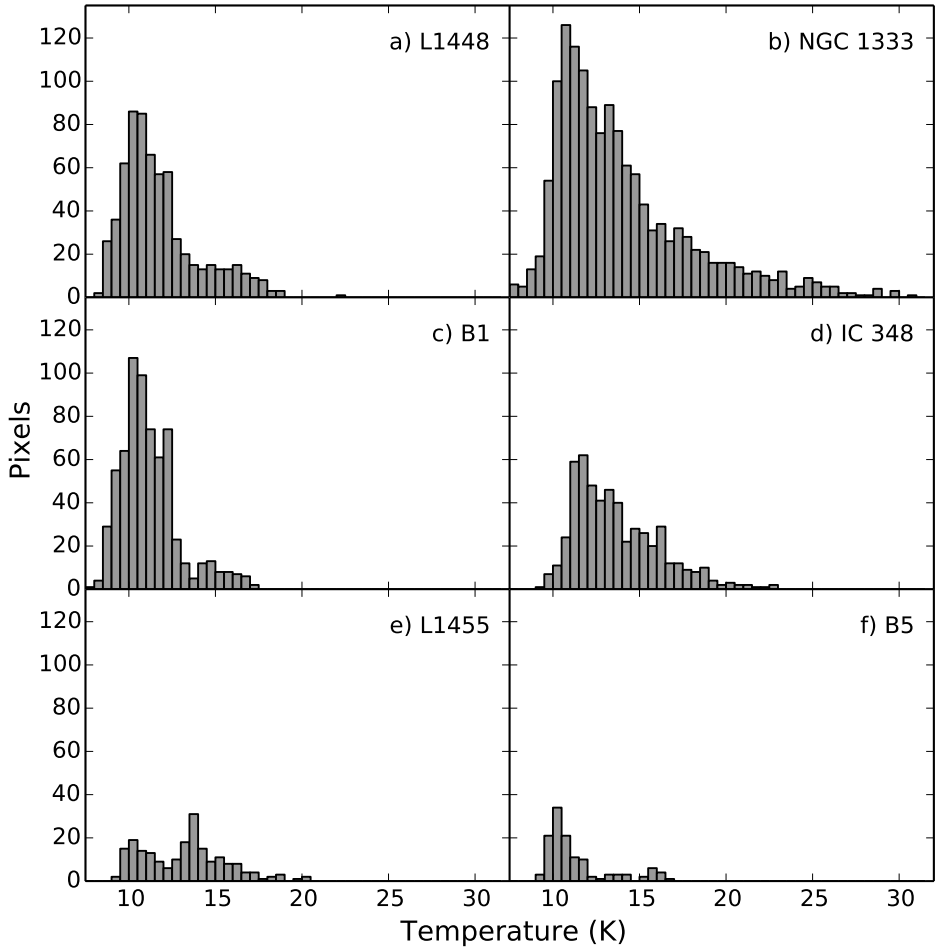

Figure 5.1 Histograms of derived temperatures in different Perseus clumps.

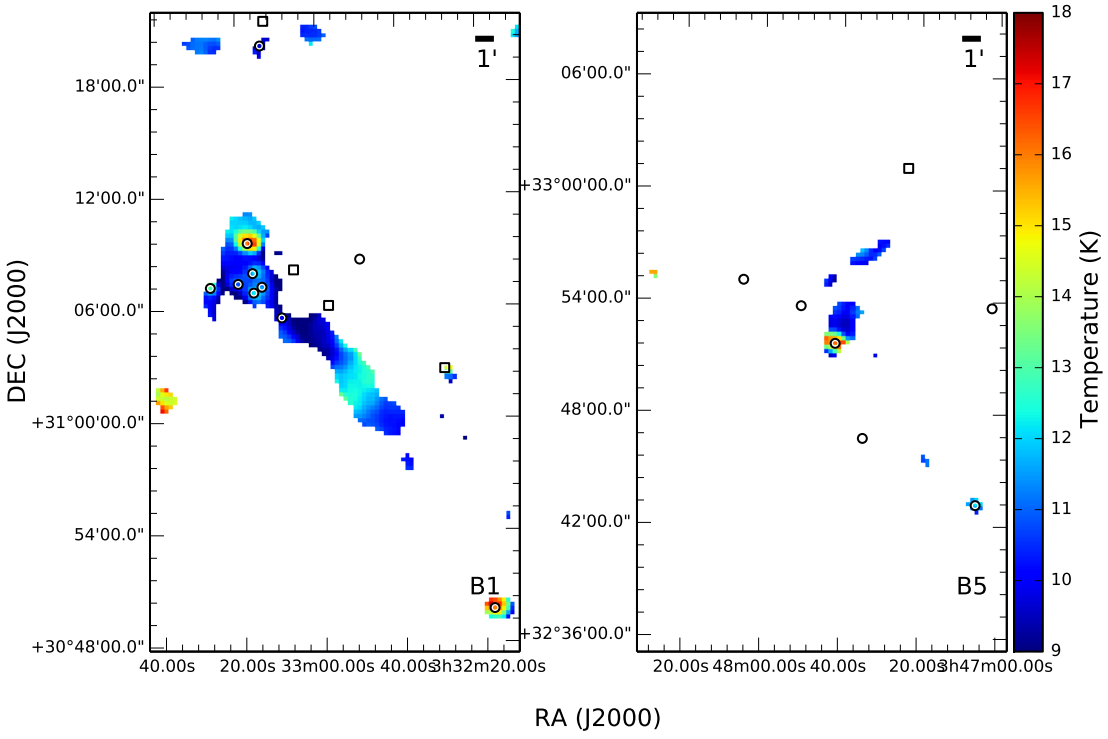

Figure 5.2 (Panels a and b.) Derived temperatures in the B1 and B5 clumps. Class 0/I and I/Flat YSOs are labelled by circles and squares respectively.

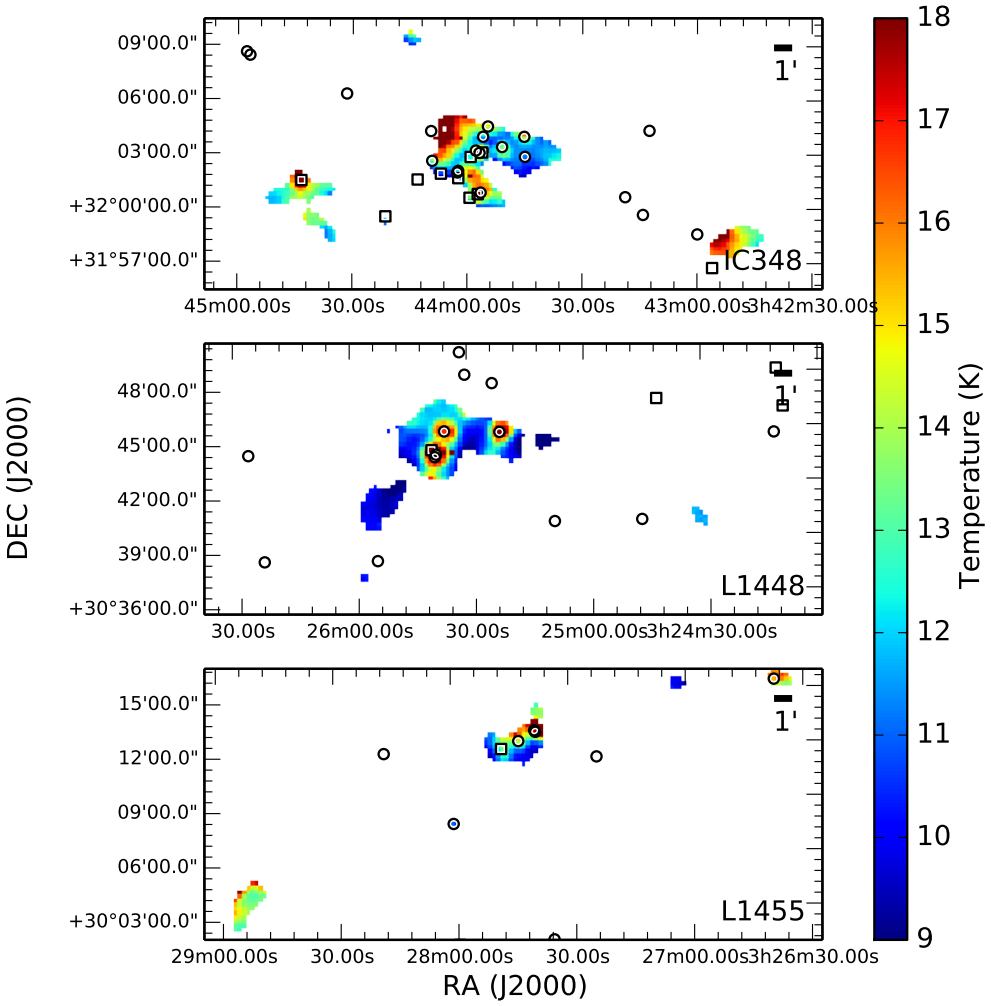

Figure 5.2 (Panels c, d, and e.) Derived temperatures in the IC348, L1448, and L1455 clumps overlaid with same symbols as in Figure 5.2a and b.

5.2 Perseus Clumps: β and τ_{300}

Figure 5.3 shows the histograms of derived β values from various clumps in Perseus. Unlike temperature, the β distributions of different clumps do not share a similar shape. While half of all six clumps in Perseus appear to have a single peak (i.e., NGC 1333, IC 348, and B5), the rest of Perseus (i.e., B1, L1455, and L1448) appears to have two or even three peaks. The separations between these peaks are larger than the typical uncertainty (~ 0.1), suggesting that these peaks are not artifacts. The β distributions of L1455 and B1 each contain a small, secondary peak centered on $\beta \sim 1$. This value is similar to what Schnee et al. (2014) found in the Orion Molecular Cloud regions 2 & 3 ($\beta \sim 0.9$), as well as recent measurements towards a few protostellar cores ($\beta \sim 0.5 - 1.0$, Kwon et al. 2009; $\beta \sim 0.9$, Chiang et al. 2012; $\beta \sim 0.6 - 0.8$, Miotello et al. 2014), but is on the lower end of many previous findings in star-forming regions (e.g., $1.0 \leq \beta \leq 2.5$, Dupac et al. 2003; $1.0 \leq \beta \leq 2.4$, Shirley et al. 2011). The β value ~ 1 is more typically found in protostellar disks (e.g., Beckwith & Sargent 1991).

NGC 1333 also has a similar number of pixels with $\beta \sim 1$ as L1455 and B1. Unlike the other two clumps, however, these low β values in NGC 1333 appear more like an extension to the main distribution than a separate bump. In NGC 1333, we found that local regions with the lowest β values appear to be spatially correlated with some of the most prominent outflow lobes in the clump (e.g., from IRAS4 and SVS13; see section 4.2).

Figure 5.4 shows maps of derived β in the B1, B5, IC 348, L1448, and L1455 clumps. Like in NGC 1333 (see Figure 4.2), pixels with similar β values tend to form well defined local structures, indicating that β variations seen in these clumps are indeed not noise artifacts and are correlated with local environment. Low β structures tend to coincide with local temperature peaks and share similar shapes. In some locations, however, such as around embedded YSOs and their outflows in L1448 and NGC 1333, low β regions can be much more extended than locally heated regions.

We found three local low-β, high-temperature structures in B1 and L1455 with β values ~ 1. One such region located in the southwest corner of the B1 map coincides with an embedded YSO. Interestingly, however, no embedded YSO identified by Spitzer is found inside the other two $\beta \sim 1$ regions. Since CO contamination has been removed over the $\beta \sim 1$ region on the east end of B1 and in general CO contamination

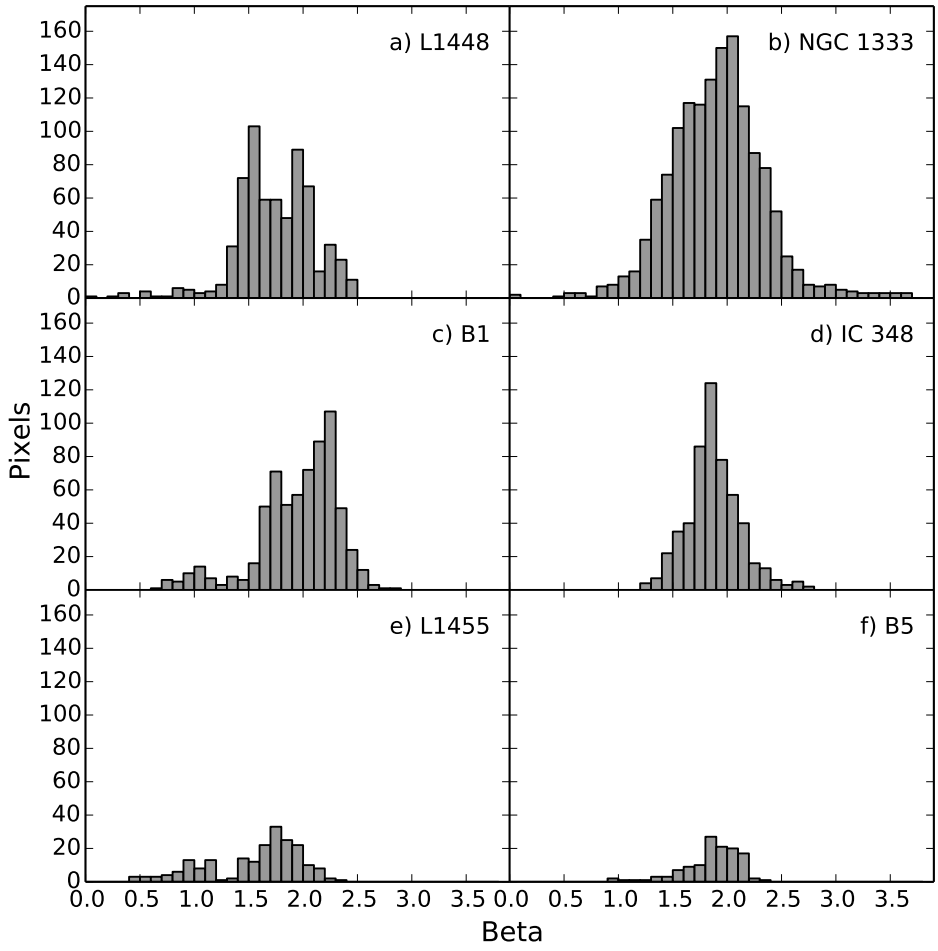

Figure 5.3 Histograms of derived β of different Perseus clumps.

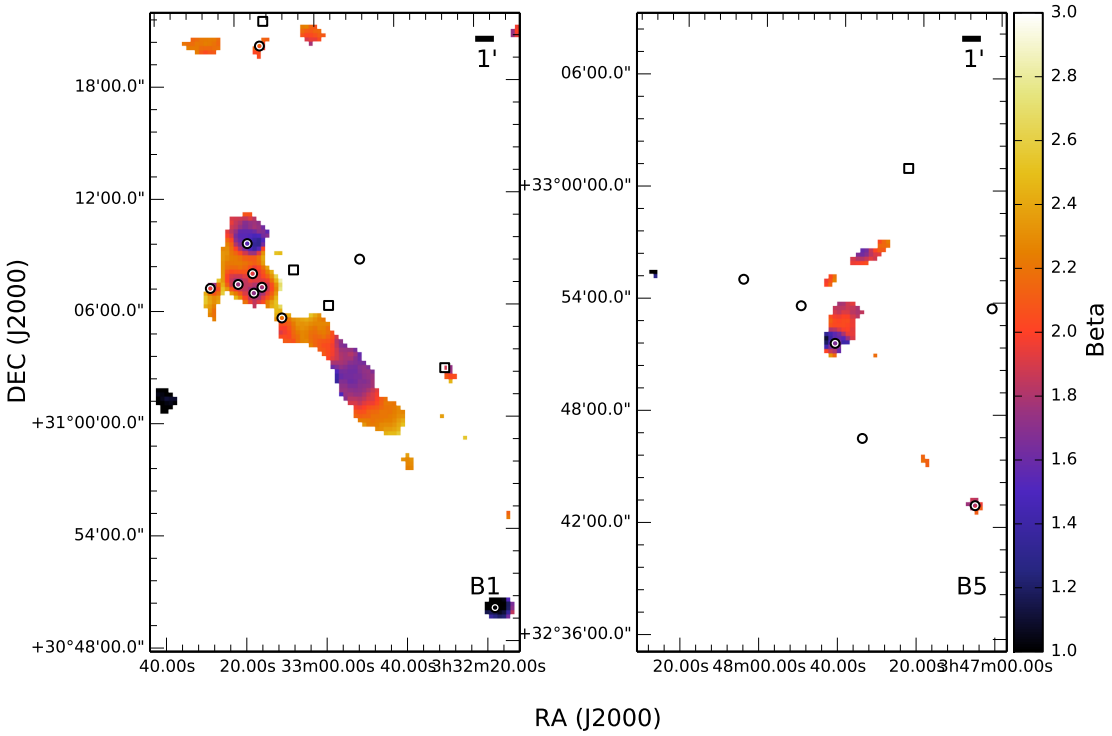

Figure 5.4 (Panels a and b.) Derived β in the B1 and B5 clumps. Class 0/I and I/Flat YSOs are labelled by circles and squares respectively.

is insignificant in Perseus (see Appendix A), the low-β , high-temperature values seen toward these regions are unlikely influenced by CO contamination.

Figure 5.5 shows maps of derived τ_{300} in the B1, B5, IC 348, L1448, and L1455 clumps, overlaid with positions of embedded YSOs. As with NGC 1333, higher τ_{300} structures seen in the B1, L1448, and IC 348 clumps are found along filamentary structures. Due to the SED fitted areas (SNR $>$ 10) in L1455 and B5 being relatively small, we cannot conclude whether τ_{300} peaks seen in these two clumps are also part of a filamentary structure. We found embedded YSOs preferentially towards local τ_{300} peaks. Similar to NGC 1333, however, many of these embedded YSOs are spatially offset from the center of these peaks, often by slightly more than a beam-width of our maps. Interestingly, we did not find any embedded YSOs towards the centers of the highest τ_{300} peaks in all Perseus clumps, with the exception of IC 348, which does not have τ_{300} peaks with particularly high values.

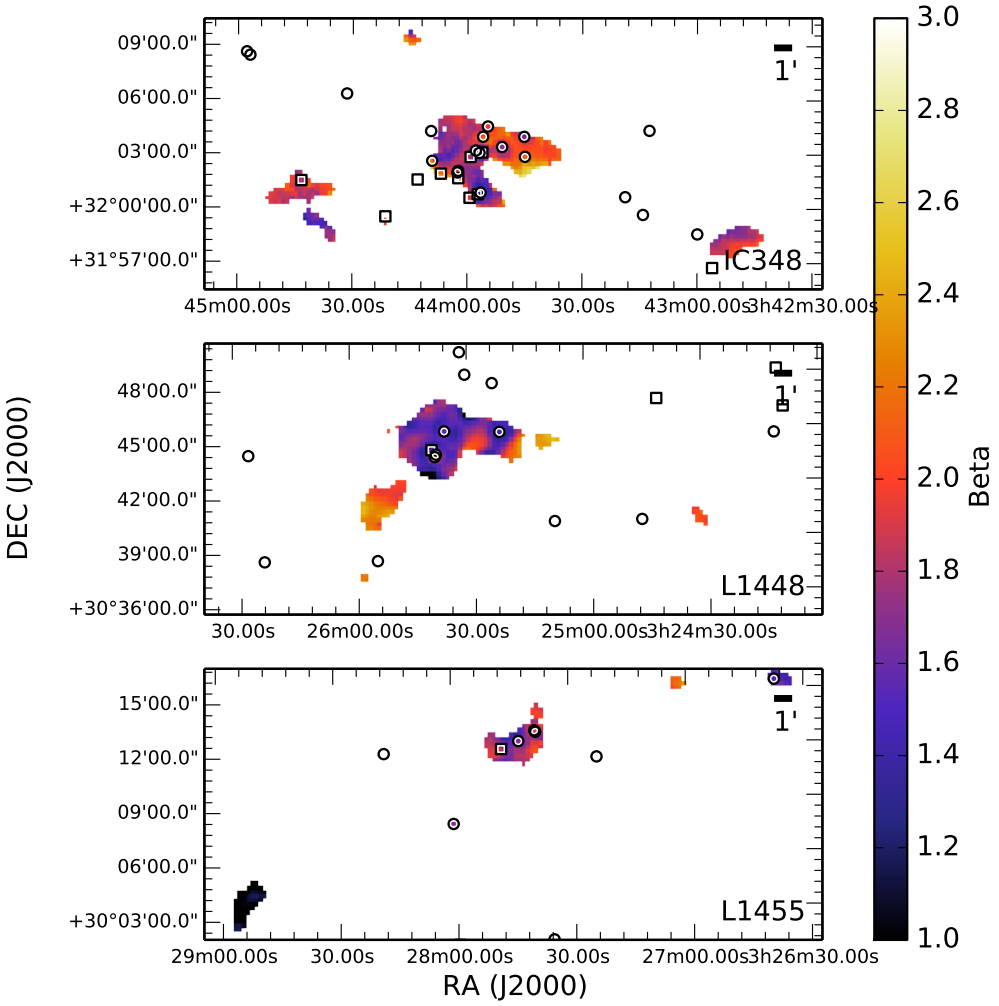

Figure 5.4 (Panels c, d, and e.) Derived β in the IC 348, L1448, and L1455 clumps overlaid with the same symbols as in Figure 5.4a and b.

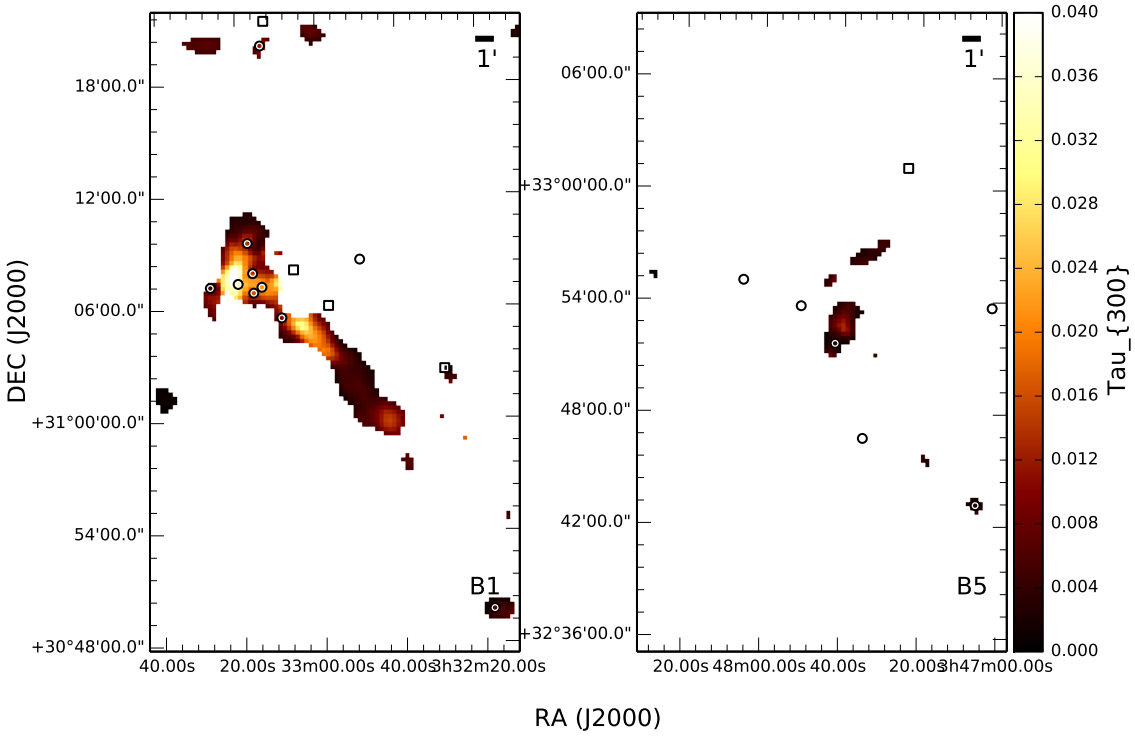

Figure 5.5 (Panels a and b.) Derived τ_{300} in the B1 and B5 clumps. Class 0/I and I/Flat YSOs are labelled by circles and squares respectively.

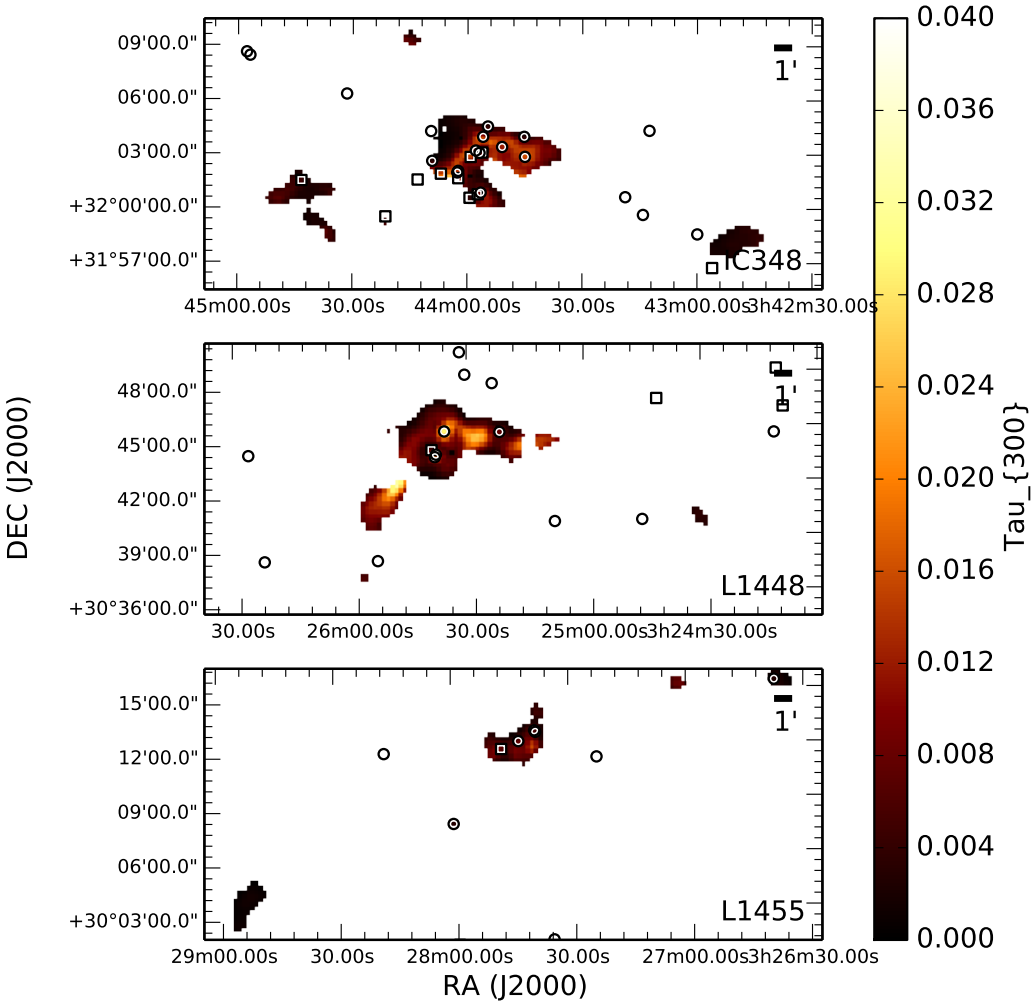

Figure 5.5 (Panels c, d, and e.) Derived τ_{300} in the IC 348, L1448, and L1455 clumps overlaid with the same symbols as in Figure 5.5a and b.

5.3 The β, Temperature, and Column Density Relations

Figure 5.6 shows scatter plots of derived β versus temperature in all six Perseus clumps. Anti-correlations between β and temperature are found in all six Perseus clumps and cannot solely be accounted by the anti-correlated β - T_d uncertainties we illustrated in Figure 4.7. Interestingly, there appears to be a prominent population of pixels in all six clumps that exhibits a fairly linear relationship with a slope of ~ -0.3. This population only contains pixels with temperatures less than 20 K. Two clumps in particular, B1 and B5, seem to consist only of this population. The other four Perseus clumps contain additional populations that have largely spread slopes which are much shallower than -0.3. In the more unique case of L1448, its second population appears to have a well defined slope of zero and a β value of ~ 1.5, independent of temperature.

Figure 5.7 shows scatter plots of derived β versus column density. While we did not find any significant correlation between β and column density for pixels with column densities $> 2 \times 10^{22}$ cm^{-2}, the pixels with column densities $< 2 \times 10^{22}$ cm^{-2} appear to be strongly correlated with β, with the exception of pixels in IC 348. The lack of such a correlation in IC 348 suggests that the correlation found in other clumps is unlikely an artifact, given that systematic uncertainties which may give rise to such a correlation should be common to all our maps. Most of these low β pixels are also located far from map edges, further suggesting that systematic errors associated with spatial filtering is not a concern. Considering that our SEDs were only fitted over data with SNR > 10, noise driven uncertainties are unlikely to be the cause of such an error either.

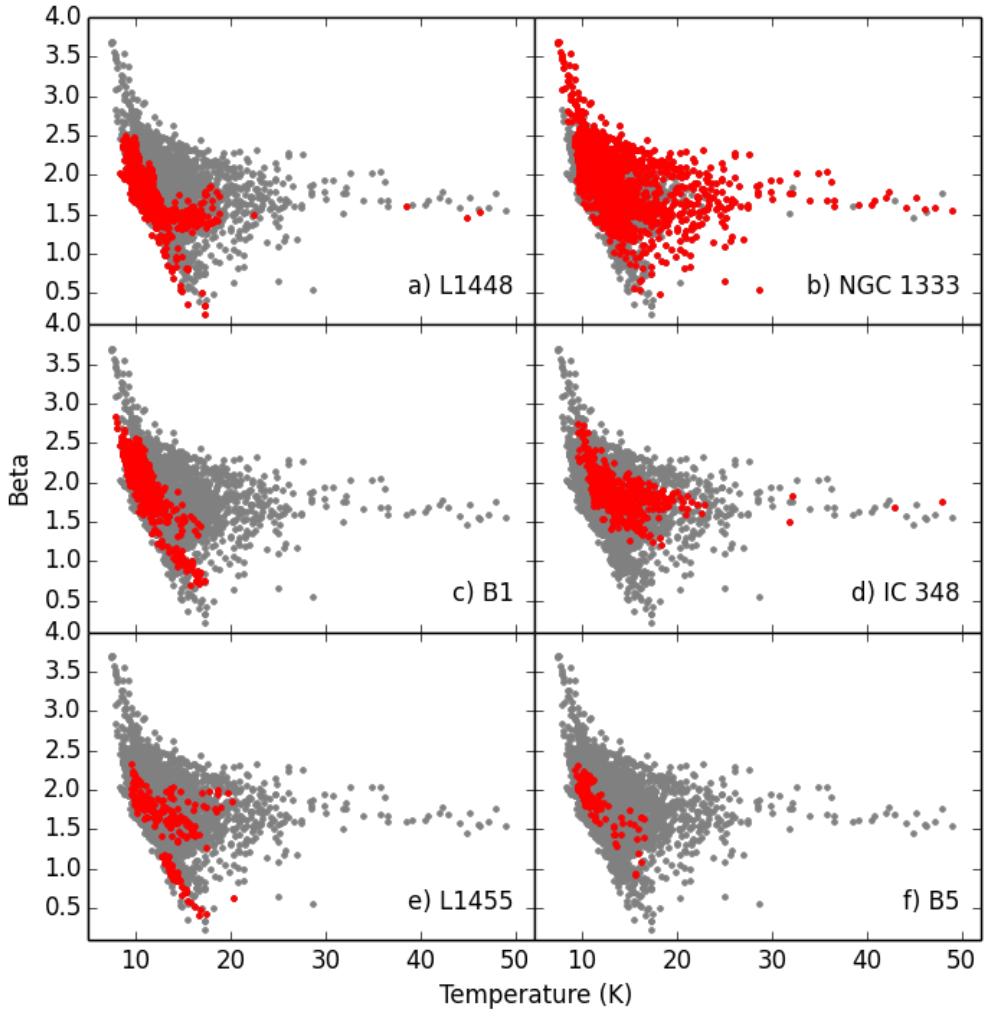

Figure 5.6 Scatter plots of derived β vs. temperature for each Perseus clump (red) overlaid onto all the Perseus clumps combined (grey). Panels a) to f) correspond to the L1448, NGC 1333, B1, IC348, L1455, and B1 clumps, respectively.

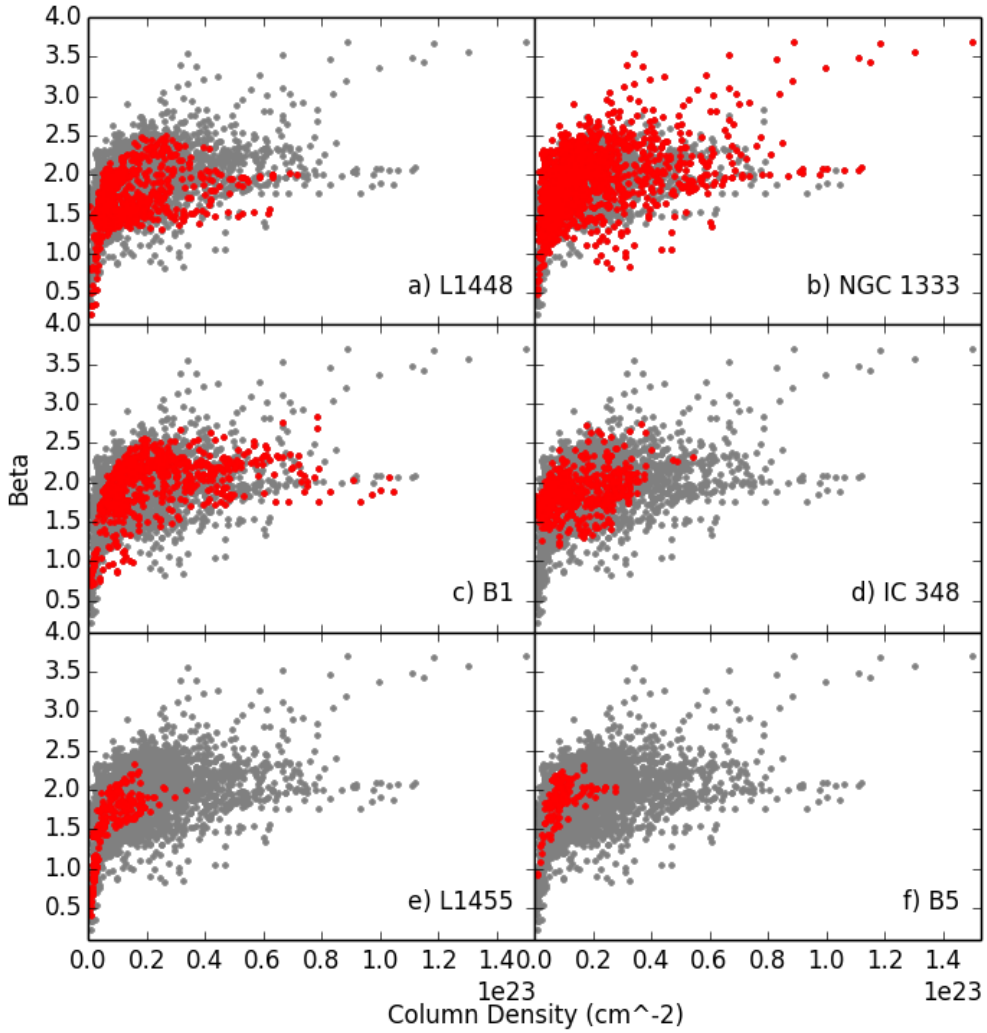

Figure 5.7 Scatter plots of derived β vs. column density for each Perseus clump (red) overlaid onto all the Perseus clumps combined (grey). Panels a) to f) shows correspond to the L1448, NGC 1333, B1, IC348, L1455, and B1 clumps, respectively.

Chapter 6

Discussion

6.1 Radiative Thermal Feedback

Throughout Perseus, we see evidence of embedded YSOs and nearby B stars heating their local environments. In contrast with the most common temperature found in Perseus, 10 K, the temperatures near an embedded YSO are typically between $\sim$ 14 K and 20 K and they can be up to 50 K near a B star. While not all embedded YSOs are associated with local temperature peaks, all the local temperature peaks coincide with locations of embedded YSOs and B stars, with the exception of one case in B1 and one case in IC 348.

The majority of the heated regions centered on embedded YSOs are larger than the FWHM beam of our map (36.6″), often having $T_d \geq 15$ K out to twice the radius of the beam. In NGC 1333, all the locally heated regions with radii nearly twice that of the beam contain at least a Class 0 or I YSO with bolometric luminosity, L_{bol}, between 4 $L_\odot$ and 33 $L_\odot$ (Enoch et al. 2009). In other Perseus clumps, similar regions contain at least a Class 0 or I YSO with bolometric luminosity between 1 $L_\odot$ and 5 $L_\odot$. If we assume our distances to the western and eastern Perseus to be 220 pc (Cernis 1990, Hirota et al. 2008) and 320 pc (Herbig 1998), respectively, then these heated regions would have radii of $\sim$ 8000 AU and $\sim$ 12000 AU, respectively, which is less than the typical size of a dense core ($\sim$15000 AU in radius, Andre et al. 2000).

The core dust temperature profile due to protostellar heating can be modelled with radiative transfer codes. Jørgensen et al. (2006a) have modelled such temperature profiles using *Dusty* (Ivezic et al. 1999[1]) for various core density profiles, protostellar

[1]Ivezic, Z., Nenkova, M., & Elitzur, M. 1999, User Manual for DUSTY, University of Kentucky

bolometric luminosities, and interstellar radiation fields (ISRF), assuming the OH5 dust opacities (Ossenkopf & Henning 1994). For a core with density profile of $n = n_0(r/r_0)^{-1.5}$, where $r_0 = 50$ AU and $n_0 = 2.7 \times 10^8$ cm^{-3} modelled after the MMS9 core in the Orion molecular cloud, its temperature drops down to 15 K at a radius of 2000 AU when an ISRF based on the solar neighborhood value (i.e., the standard ISRF) and a $L_{bol} = 10$ $L_\odot$ for the central source is assumed. The size of this local heating is significantly smaller than what we found in Perseus ($\sim 8000 - 12000$ AU). This result suggest that most of these locally heated regions may contain embedded YSOs with $L_{bol} > 10$ $L_\odot$, which is puzzling given that only two embedded YSOs found in Perseus (i.e., IRAS 2A and SVS 13A in NGC 1333) meet this luminosity criterion. Naively, we can try to reconcile this discrepancy by increasing the intensity of the ISRF in Jørgensen et al.'s model, but such an attempt would increase the inter-core temperatures well above that which we found in Perseus ($\sim$ 10 - 12 K). Further investigation is needed to understand the discrepancy between these temperature profiles.

Regions locally heated by B stars are more extended than regions heated by protostars. In NGC 1333, we found regions with $T > 15$ K to be $\sim 1.6'$ in radius, corresponding to $\sim$ 21000 AU. Since these B stars are not embedded objects, we can reasonably approximate the temperature profile of their surrounding dust in the optically thin limit. An analytic expression of such a temperature profile first derived by Scoville & Kwan (1976) can be generalized as

$$T_d(r) = 50 Q_{abs}^{-q/2} \left(\frac{r}{2 \times 10^{15}\mathrm{m}} \right)^{-q} \left(\frac{L_{bol}}{10^5 \mathrm{L}_\odot} \right) \mathrm{K} \tag{6.1}$$

where Q_{abs} is the absorption efficient of a dust grain at $\lambda = 50$ μm, and $q = 2/(4+\beta)$ (Equation 1, Chandler et al. 1998). For the expected range of β values between 1 and 2, the q parameter does not vary significantly, and the power-law slope of the temperature profile resembles that of Jørgensen et al.'s (2006a) dusty profile at larger radii where the protostellar envelope is expected to be optically thin, before the ISRF heating starts to become dominant.

To model the radial temperature profiles near these two B stars, we assumed $\beta = 1.6$, the typical β we found near the two B stars in NGC 1333, and normalized Equation 6.1 to Wolfire & Churchwell's (1994) dust emission models with $Q_{abs}^{-q/2} = 1.2$,

as Chandler et al. (1998; 2000) and Jørgensen et al. (2006a) have done. Given that the B stars BD +30 549 and SVS3 have luminosities of 42 $L_\odot$ (Jennings et al. 1987) and 138 $L_\odot$ (Connelley et al. 2008), respectively, the temperature of these two stars would drop down to 15 K at radii of ∼10000 AU and 20000 AU, comparable to the distances we have observed.

Star-forming structures can gain additional pressure support through additional heating. The gravitational stability of these structures can be estimated using the Jeans criterion by treating them as an isothermal ideal gas with uniform density. The smallest length at which such an object can become gravitationally unstable due to perturbation is called the Jeans length, λ_J, which is related to the object's temperature by $\lambda_J \propto T^{1/2}$. The total mass enclosed within a Jeans length is known as the Jeans mass, M_J, which scales as $M_J \propto T^{3/2}$. As expected, warmer objects can hold more mass than their cooler counterparts before becoming gravitationally (Jeans) unstable.

Even though protostellar heating is the most common form of local heating observed in Perseus, protostellar cores are likely no longer Jeans stable since they are currently collapsing into protostars. Protostellar heating, however, could provide additional Jeans stability to inter-core gas, but we have found no evidence in Perseus of heating from solar-mass YSOs that extends beyond the typical radius of a core ($\lesssim$ 15000 AU, Andre et al. 2000).

While B stars may not have circumstellar envelopes themselves, they may be capable of heating nearby protostellar cores. Indeed, three SCUBA cores identified by Hatchell et al. (HRF2005, 2005) are located in projection within these B star heated regions: HRF57, HRF56, and HRF54. These cores do not contain known YSOs and have beam averaged temperatures between 19 K and 40 K. At these temperatures, the Jeans masses of theses cores are a factor of $\sim$ 3 - 8 higher than those of their counterparts at 10 K, if we assume that their densities remain unchanged in the process of heating. Such gains in Jeans mass are not particularly significant, especially given our assumption that the core densities remain the same in different temperatures. Thermal feedback, thus, does not appear to be a significant regulator of star formation in Perseus, especially on scales larger than 10000 AU.

6.2 Outflow Feedback

Several studies of dust continuum emission in NGC 1333 (Lefloch et al. 1998; Sandell & Knee 2001; Quillen et al. 2005), as well as other nearby star-forming clumps (e.g., Moriarty-Schieven et al. 2006), have suggested that outflows can play a significant role in shaping the local structure of star-forming clumps. As with these prior studies, we find several τ_{300} cavities that coincide with bipolar outflows, particularly towards the ends of outflow lobes, in NGC 1333 and L1448 (see Figure 6.1). Due to warmer temperatures, which can cause low column density dust to have relatively high flux, some of these regions were not revealed directly by the continuum emission. This situation is particularly true for the valley-like features coinciding with embedded YSOs. The coincidence between outflows and τ_{300} cavities/valleys suggests that the former are carving out the latter. Figure 6.1 shows two such examples, the outflows originating from IRAS 4 (HRF41) in NGC 1333 and L1448-IRS2 (HRF30) in L1448.

In addition to low τ_{300} regions, we also found two high τ_{300} regions in Perseus that may have been formed from compression by nearby outflows. For example, the high τ_{300} region near the starless core HRF51 in NGC 1333 has the highest τ_{300} values in the clump, and is also located towards the southeastern end of the outflow associated with the HH7-11 outflows driven by SVS13 (Snell & Edwards 1981). The high τ_{300} region surrounding the HRF28 and HRF29 cores in L1448 also has the second highest τ_{300} values found in L1448, and is located on the northeastern end of the outflow originating from L1448C (HRF29, a.k.a. L1448-mm) near HH197 (e.g., Bachiller et al. 1990; Bally et al. 1997). The presence of Herbig-Haro objects in these high τ_{300} regions indicates that outflows are indeed interacting with ambient gas in these regions and perhaps compressing it in the process, resulting in the observed high τ_{300} values. Given that the τ_{300} values we found around the starless core HRF51 are unusually high in comparison with the rest of Perseus, HRF51 would be a good candidate for followup observations to determine whether it is truly starless, has high spatial density, and is significantly supported by turbulence.

It is noteworthy that we do not find evidence for shock-heating from outflows in our dust temperature maps. The dominant local influence of outflows appears to be their ability to reshape local structures such as cores and filaments. Indeed, gas compression driven by outflows can stimulate turbulence to form starless cores beyond simple Jeans instability. For example, the extra material being pushed towards a starless core by outflows can provide the needed perturbation to trigger core collapse,

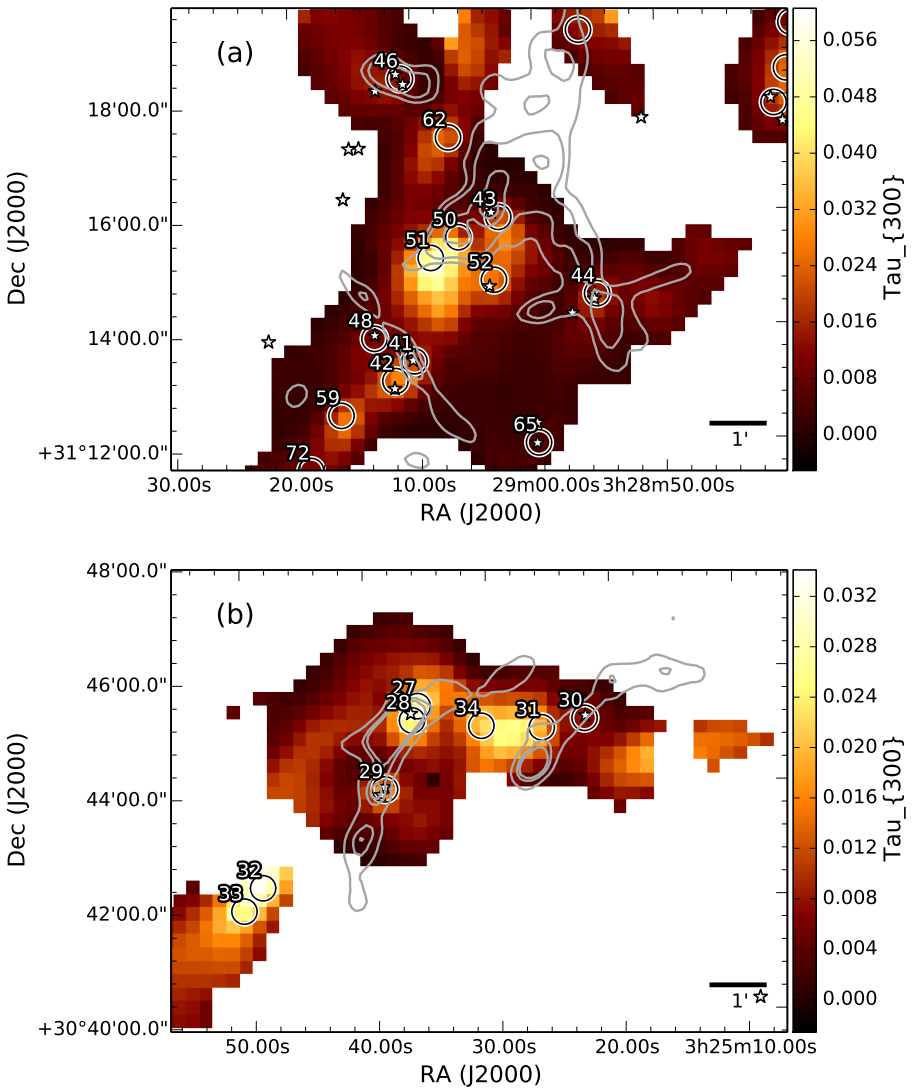

Figure 6.1 Maps of τ_{300} in a) NGC 1333 and b) L1448 overlaid with the SCUBA cores identified by Hatchell et al. (2005; circles), Class 0/I YSOs indentifed by Evans et al. (2009; stars), and contours of spatially filtered, integrated ^{12}CO 3-2 emission. Contours of CO emissions are drawn at 15 mJy/beam, 30 mJy/beam, 80 mJy/beam, and 110 mJy/beam for Figure a) and at 10 mJy/beam, 20 mJy/beam, and 25 mJy/beam for Figure b).

as well as providing the core with extra mass to accrete. On the other hand, these outflows can in principle also inject turbulence into the structures they compress, providing additional pressure support for these dense structures to remain temporarily stable against Jeans instability. The mechanical feedback from outflows, therefore, is likely important in regulating star formation in clustered environments where it can enhance or impede the processes through compression or carving, respectively.

6.3 Beta and Clump Evolution

The global properties of a star-forming clump are expected to evolve significantly as star formation progresses within it. During star formation, the gas within a clump, for example, starts by concentrating into denser structures, which leads to gravitational instability, and ends with dispersal by feedback generated from the stars that formed. Given that dust grains can undergo growth inside cold, dense environments and potentially be fragmented or destroyed in energetic processes, dust grains themselves are expected to evolve with their environment over time. If grain evolution in these environments is dominated by processes that result in a significant change in β, then we should be able to observe the values of β varying from clump to clump, due to the different evolutionary stages of these clumps.

6.3.1 Beta Variation and its Relation to Temperature

Within the individual clumps in Perseus, we have found a significant variation in β. As shown in Figure 5.3, the majority of β values in these clumps range from 1.0 to 2.5, with the exception of NGC 1333 which has a non-negligible number of pixels with β values that go up to 3.0. The spatial distribution of β is not erratic, and appears fairly structured on a local scale, suggesting that β is likely dependent on the properties of the local environment. Furthermore, the spatial transition between pixels with $\beta > 2$ and < 1.6, though relatively sharp, is not abrupt with respect to our beam width ($36.3''$ FWHM). The overall appearance of β maps, as well as their temperature and τ_{300} counterparts, are fairly smooth, suggesting that our derived β values are robust against noise in the data.

As mentioned in Section 5, our derived β and temperature values appear to be anti-correlated, similar to behavior found in prior studies of nearby star-forming regions at lower angular resolutions (e.g., Dupac et al. 2003; Planck Collaboration XXV et al.

2011). The fact that lower β regions tend to be spatially well structured and coincide with locations known to be locally heated further demonstrates that there indeed exists an anti-correlation between β and temperature that is not an artifact of the noise.

Shetty et al. (2009b) have shown that line-of-sight temperature variations can lead to an underestimation of β and an overestimation of density-weighted temperature (column temperature) by fitting a single-component modified blackbody curve to the SEDs of various models of cold cores and warm envelopes that have a single β value. When these synthetic SEDs are noiseless and are equally well sampled in both the Wien's and Rayleigh-Jeans' regimes, Shetty et al. found that systematic exclusion of shorter wavelength data will allow the fitted β values and temperatures to approach the true β value and column temperature. A single-component modified blackbody curve simply does not fit well SEDs with multiple temperature components in the Wien's regime.

In NGC 1333, we found the typical temperature of starless cores to be $\sim$ 10 K. This temperature is consistent with both the typical core temperature found by Evans et al. (2001) and Shetty et al.'s modelled column temperature of 9.6 K, which was itself based on Evans et al.'s core density and dust temperature profiles (Shetty et al. 2009b). If the true β values along the lines of sight of our observations are fairly uniform, then the agreement between our derived temperature and Shetty et al.'s modelled column temperature suggests that our fits for these cold cores' SEDs are robust against line-of-sight temperature variation and our derived β values similarly approach those of the true β. Examination of our SED fits in a few sample pixels have demonstrated that SEDs found in cold cores are indeed well fitted by single component modified blackbody curves.

In warmer regions, however, some of our SED fits have trouble reconciling with the shortest wavelength band (i.e., 160 μm), suggesting that line-of-sight temperature variation may be a concern in these specific regions. Given that preferential sampling towards the Rayleigh-Jeans tail will allow SED fits to place a tighter constraint on β, as Shetty et al. demonstrated, the β values we measured across 160 - 850 μm toward the warmer regions should remain fairly robust against temperature variation along the line of sight as the peaks of these SEDs shift further toward shorter wavelengths. Indeed, the fact that our sampled SED fits only have trouble fitting the 160 μm bands in warmer regions suggest that these SED fits are weighted towards the longer wavelength points where β can be more robustly determined.

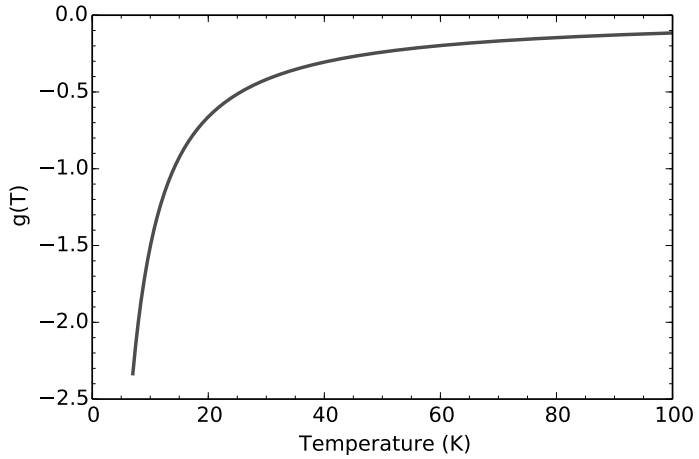

Figure 6.2 The $g_{01}(T_d)$ term of the α function (Equation 6.4) taken at 500 μm and 850 μm.

An alternate way to estimate β or T_d is to take the flux ratio between observations made in the lower frequency bands, typically on the Rayleigh-Jeans side of the SED. Following Equations 1.1, 1.2, and 1.3, the log of the flux ratio taken at frequencies ν_0 and ν_1 can be expressed as

$$\log\left(\frac{I_0}{I_1}\right) = (\beta+3)\log\left(\frac{\nu_0}{\nu_1}\right) + \log\left[\frac{\exp(h\nu_1/k_BT_d)}{\exp(h\nu_0/k_BT_d)}\right]. \tag{6.2}$$

We further define α as the following,

$$\begin{aligned}\alpha_{01} &\equiv \frac{\log(I_0/I_1)}{\log(\nu_0/\nu_1)};\\ &= \beta + 2 + g_{01}(T_d),\end{aligned} \tag{6.3}$$

where,

$$g_{01}(T_d) = \frac{1}{\log(\nu_0/\nu_1)}\log\left[\frac{\exp(h\nu_1/k_BT_d)}{\exp(h\nu_0/k_BT_d)}\right] + 1. \tag{6.4}$$

Then, in the Rayleigh-Jeans limit $g_{01}(T) \to 0$, and α takes the form $\alpha = \beta + 2$, which is commonly adopted in the literature for this specific limit. Figure 6.2 shows the behavior of $g_{01}(T_d)$ measured between 500 μm and 850 μm. As expected, $g_{01}(T_d)$ approaches zero at high temperatures where we sample the Rayleigh-Jeans limit of the SED and diverges towards $-\infty$ as temperature goes to zero (where we sample the

Wien's limit of the SED). Between these particular wavelengths, $g_{01}(T_d)$ is relatively sensitive to T_d at $T_d \lesssim 60$ K.

Figure 6.3 shows the map of α across NGC 1333, calculated from the 500 μm and 850 μm maps. As can be seen, many α peaks are spatially correlated with peaks seen in our temperature map derived from full SED fits (Figure 4.2). Given that $\alpha = \beta + 2 + g_{01}(T_d)$, assuming a fixed β would imply that the changes observed in α are solely due to temperature. Figure 6.2 reveals that higher $g_{01}(T_d)$ measures should occur in warmer environments. Indeed, such behavior is in qualitative agreement with our full SED fits as described above, providing independent confirmation that the warm regions seen in our maps are indeed physical and that they preferentially sample the Rayleigh-Jeans tail of the SED. The temperatures drawn from measuring flux ratios in NGC 1333 with early science SCUBA-2 data (Hatchell et al. 2013) also agree with this finding. We are therefore confident that there exists a true anti-correlation between β and temperature in our data that cannot be accounted for by the anti-correlated uncertainties between β and temperature associated with temperature variations along the line of sight, as well as the noise, as addressed in Section 4.4.

6.3.2 The Cause Behind β Variations

Laboratory measurements have shown that β values can be intrinsically temperature dependent (e.g., Agladze et al. 1996; Mennella et al. 1998; Boudet et al. 2005). Many of these measured dependencies, however, are not significant enough to explain by themselves the anti-correlation seen here. Agladze et al. found two species of amorphous grains with β values that decrease from ~ 2.5 to ~ 1.7 - 2 as the temperature increases from 10 K to 25 K. While these measured temperature dependencies are still not strong enough to be the sole cause of the anti-correlation we see, they are perhaps significant enough to provide a partial contribution.

Dust coagulation models have shown that grain growth can cause β values to decrease significantly from the typical ISM value ($\beta \sim 2$), to as low as zero (e.g., Miyake & Nakagawa 1993; Henning et al. 1995). Since dust coagulation is favored in a denser environment, where the dust collision rates are higher, lower β values may be expected towards the densest regions. Furthermore, since the densest regions that are not internally heated tend to be the coldest regions, one may expect β and temperature to be positively correlated.

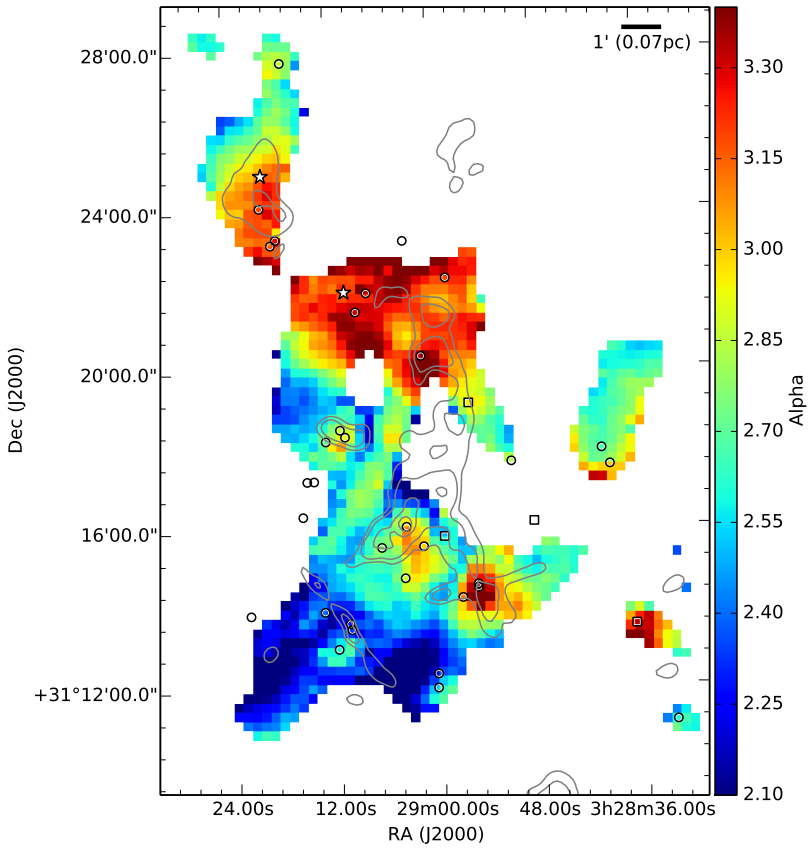

Figure 6.3 Map of α in NGC 1333, calculated from the 500 μm and 850 μm maps with Equation 6.3. The overlaid symbols are the same as in Figure 4.2.

As shown in Figure 5.7, we do not find evidence that β is anti-correlated with column density. In contrast, we find that the highest column density structures in Perseus tend to have $\beta \gtrsim 2$, especially towards the colder regions not associated with localized heating. The lack of decrease in β towards these dense regions, however, is not sufficient to rule out grain growth through coagulation. The presence of an ice mantle on the surface of a dust grain, for example, can increase β from ~ 2 for a bare grain to ~ 3 (Aannestad 1975). Since the growth of ice mantles is also favored in the coldest and densest environments, such growth can, in principle, compete with coagulated grain growth by modifying β in opposite directions, causing the dust in some of the highest column density regions to have $\beta \sim 2$ instead of higher or lower values (see Figure 5.7).

Given that the presence of ice mantles on grain surfaces may be capable of countering the decrease in β caused by coagulated grain growth, we speculate that the β - T_d anti-correlation may be explained by the sublimation of ice mantles in warmer environments. This hypothesis is useful in explaining why internally heated protostellar cores have lower β values than their starless, non-heated counterparts. Measuring the depletion levels of molecules that ice mantles typically consist of towards heated and non-heated cores could help to test this hypothesis, provided that these molecules can themselves survive in these heated environments.

While lower β regions tend to coincide with locally heated regions, we also found that lower β regions tend to be spatially more extended than these heated regions. The low-β region surrounding IRAS 4 in NGC 1333 is a prominent example of this behavior. Interestingly, many lower β regions also coincide with the locations of bipolar outflows, prompting us to suspect that outflows may be capable of carrying lower β grains from deep within a protostellar core out to a scale large enough to be observed with our spatial resolution .

The fact that IRAS 4 is surrounded by some of the lowest β values measured in our maps (~ 1.0) and that it drives one of the most powerful outflows in NGC 1333 helps to support such a hypothesis. Indeed, the low β grains may have originated from the circumstellar disk surrounding the embedded YSO, i.e., where $\beta \sim 1$ has been seen in less embedded (more evolved) systems, and were carried out by a jet originating at the innermost part of the disk. Similarly, lower β grains may have been produced in the densest inner portion of a circumstellar envelope, in addition to the disk, and became entrained with the outgoing outflow. Alternatively, the energetic environments associated with outflows may also cause the sublimation of ice mantles,

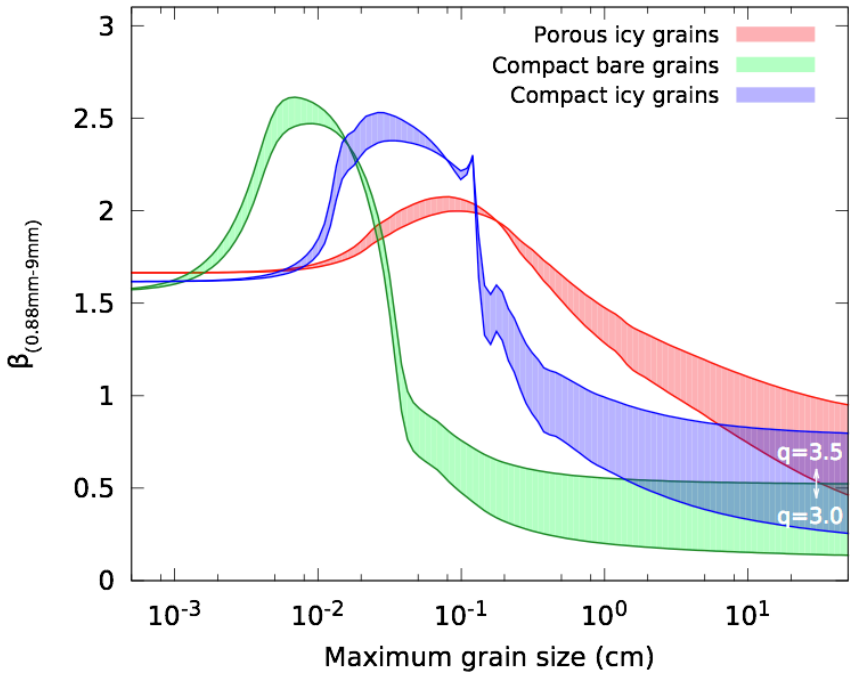

Figure 6.4 The β values calculated for 0.88 mm $\leq \lambda \leq$ 9 mm as a function of the maximum grain size, for a grain size distribution $n(a) \propto a^{-q}$, based on Natta & Testi's (2004) prescription (Fig. 4, Testi et al. 2014). Different colors correspond to grain models with different chemical composition and porosity.

but this effect may be limited only to localized shocked regions and may be insufficient to produce enough low β grains to dominate the β value observed along the line of sight. Very high angular resolution observations of β within protostellar and prestellar cores may help to verify if low β grains are preferentially found deep within a dense core, and whether or not their production is associated with the presence of protostars or disks. Recent high resolution, interferometric studies on the inner regions of a small number of protostellar envelopes have found that $\beta \leq 1$ (Chiang et al. 2012; Miotello et al. 2014), suggesting that dense, inner regions of cores may indeed be a site for significant grain growth.

Interestingly, the dependence of β on the maximum grain size, a_{max}, assuming a power law grain size distribution, i.e., $n(a) \propto a^{-q}$, behaves similarly regardless of other β dependencies (Testi et al. 2014). As shown in Figure 6.4, β values computed by Testi et al. all have values of $\sim$ 1.6 and 1.7 when a_{max} is less than $\sim 10^{-3}$ cm, independent of the chemical composition and the porosity of the dust grain. As a_{max} increases, β values for all three models first increase upwards to a maximum value

of $\sim$ 2.5 for compact grains, or $\sim$ 2 for porous icy grains, and then drop down to values less than 1 at $a_{max} \gtrsim 10^{-1}$ cm. If we assume the β dependency on a_{max} to be the dominant driver of β evolution in a clump, while all other dependencies are only locally significant, then β values observed on the global scale of a clump should be a good proxy to measure the evolution of grain size in a clump.

6.3.3 Beta Variations Between Clumps

The presence of Class 0 YSOs is a good indicator of current star-formation because the Class 0 designation corresponds to the earliest stage of YSO evolution and lasts only $\sim 10^4$ years, much less than other protostellar stages. To quantify how active a clump is in forming stars currently, one can compare the number of Class 0 YSOs to the total number of YSOs and starless cores found in a clump (Sadavoy 2013). In order of the lowest to highest fractional Class 0 YSOs, the Perseus clumps rank as follows: B5, L1455, IC 348, B1, NGC 1333, and L1448. Given that star formation in a clump is expected to ramp up in the early stages of the clump evolution before it winds down in the later stages, both the youngest and the oldest clumps are expected to have low fractions of Class 0 YSOs.

In Figure 5.3, we found that the four clumps with the lowest fractions of Class 0 YSOs (B5, L1455, IC348, and B1) all have a β distribution peak around β = 1.7 - 1.8, consistent with β values computed by Testi et al. (2014) for $a_{max} \lesssim 10^{-3}$ cm. On the other hand, we found the three clumps with the highest fractions of Class 0 YSOs (B1, NGC 1333, and L1448) to all have at least a peak with $\beta \geq 2$, where the β values correspond to intermediate a_{max} values $\sim 10^{-3}$ cm - 1 cm (Testi et al. 2014). This finding is consistent with the view that the star-forming rate is likely to be highest during the intermediate stages of a clump's evolution when the maximum grain size a_{max} is expected to have an intermediate value.

Given that the mean β uncertainty due to flux uncertainties in Perseus is $\sim$ 0.2, and that a large fraction of the dust outside of dense structures is unlikely to undergo significant grain growth, most of the β values are expected to resemble the diffuse ISM values ($\sim$ 1.8 - 2). Thus, a more sensitive method to probe β evolution in a clump is desired.

One way to address this issue is to bin β values into three categories. We adopted bins with β values of 0 - 1.5, 1.5 - 2, and 2 - 3 to represent evolved, pristine, and transitional values of a_{max}, and thus β, respectively. This choice is based on Testi

et al's (2014) modelled β - a_{max} relations, and we extended the upper limit of the pristine, i.e., medium, β bin to a value of 2 to include the observed β values of ~ 2 in the diffuse ISM.

As shown in Figure 6.5, the distributions of binned β values do indeed vary from clump to clump. If we assume the evolution of β values to be driven primarily by grain growth, then based on Testi et al.'s (2014) computations shown in Figure 6.4 we would expect a significant fraction of β values to migrate into the upper bin before making their way down into the lower bin as dust grains grow larger in size. The clumps IC 348 and B5 have the highest fractions of pristine bin values and the lowest fraction of evolved bin values amongst all six Perseus clumps, suggesting that the typical a_{max} value found in IC 348 and B5 are the lowest in Perseus. On the other hand, the β distribution found in L1455 nearly mirrors that of IC 348 or B1, indicating that it has the highest a_{max} values out of the six Perseus clumps. When ranked by their putative respective a_{max} from low to high, the Perseus clumps are ordered as the following: IC 348, B5, B1, NGC 1333, L1448, and L1455.

The a_{max} values of a clump can be viewed as a rough indicator of its age. Older clumps are able to provide more time for dust grains to grow significantly in dense structures and host more dense structures as clump gas becomes more concentrated over time. It may seem surprising at first that the a_{max} indicator would suggest IC 348 as the youngest clump, given that IC 348 has often been considered as an older star-forming clump near the end of its star-forming phase (Bally et al. 2008). The region mapped for our SED fits, however, actually traces a filamentary ridge of higher density gas just southwest of the main optical cluster. This sub-region hosts a higher fraction of Class 0 and I YSOs and a lower fraction of Class II and III YSOs relative to the rest of IC 348 (Herbst 2008). The relatively higher abundance of embedded YSOs in comparison to their more evolved counter parts in this area of IC 348 suggests that this sub-region is indeed quite young, consistent with what is implied by its relatively low a_{max}.

The typical a_{max} value of B5 inferred from its β distribution also suggests that B5 is rather young and similar in age to the sub-region of IC 348 we probed. Indeed, the lack of Class II and Class III YSOs seen towards B5 is consistent with this view (Sadavoy 2013). Conversely, the L1455 clump is likely the oldest clump in Perseus, as indicated by its high corresponding a_{max} values. The relatively higher number of Class II YSOs seen towards L1455 compared to Class 0, I, or Flat YSOs also suggests that L1455 is a more evolved clump where the star-forming rate is winding down.

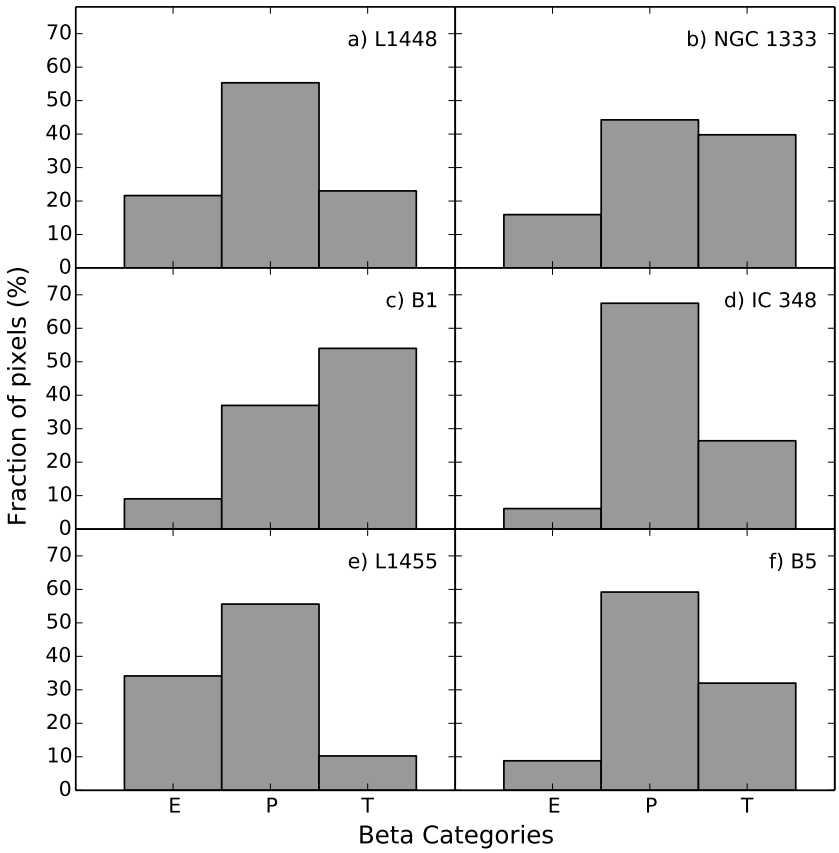

Figure 6.5 Bar graph of derived β of different Perseus clumps binned to three categories based on Testi et al.'s (2014) calculations: evolved (E), pristine (P), and transitional (T). The corresponding β values in these three categories are 0 - 1.5, 1.5 - 2, and 2 - 3, respectively.

It should be noted that the number of YSOs observed in many Perseus clumps is relatively small and we only use the YSO counts for consistency checks on extreme cases (i.e., the youngest and oldest) rather than as an alternate age indicator for star-forming clumps. Given that grain growth is subjected to local factors such as density and temperature over time, which may also differ between clumps, we do not expect the 'age' we inferred from a_{max} to be strictly proportional to time. Our 'age' estimate, therefore, is more representative of the evolutionary stage of a clump rather than the time elapsed in a clump.

From the β - T_d scatter plots of the six Perseus clumps (Fig. 5.6), we have found significant anti-correlations between β and temperature which cannot be accounted for solely by anti-correlated uncertainties associated with noise or temperature variation along the line of sight. Interestingly, there appears to be a population of pixels in all six clumps that are located at the bottom left corner of the β - T_d scatter plots with temperatures less than 20 K. The anti-correlation displayed by this particular population appears fairly linear, and has a slope of ~ -0.3. This population is primarily responsible for the wide range of β values observed in each clump and its presence in all six clumps may suggest a universal dust evolution that is common to all star-forming clumps.

The β - column density distributions (see Fig. 5.7) of Perseus clumps all behave fairly similarly and do not show obvious trends associated with clump evolution. IC 348, though, does distinctly lack the significant drop in β towards low column densities that is present in other Perseus clumps. Given that the region we sampled in IC 348 may be the youngest star-forming clump in Perseus, its lack of lower β values toward the lower column density end may suggest that there has not been enough time for the dust grains within the clump to grow significantly and bring down the β values.

Chapter 7

Conclusion

In this study, we fitted modified blackbody SEDs to combined Herschel and JCMT continuum observations of clumps in the Perseus molecular cloud and simultaneously derived dust temperature, T_d, spectral emissivity index, β, and optical depth at 300 μm, τ_{300}, using the best technique developed by Sadavoy et al. (2013). We further calculated column densities in Perseus by scaling the derived optical depth with an adopted dust opacity, κ_{300}, referenced at 300 μm.

We performed a detailed analysis of the derived T_d, β, and τ_{300} in NGC 1333, the most active and complex star-forming clump in Perseus, and found levels of ^{12}CO 3-2 line emission in the 850 μm SCUBA-2 data to be globally insignificant with respect to flux calibration uncertainties. The ^{12}CO 3-2 line is only significant when bright, small-scale CO structures, such as bipolar outflows, overlap with faint dust emission sources. We removed CO contamination in the 850 μm maps by spatially filtering the HARP ^{12}CO 3-2 maps wherever HARP ^{12}CO 3-2 observations have been made.

In NGC 1333, we also investigated anti-correlated uncertainties between β and T_d, and demonstrated that the β - T_d anti-correlations we found in Perseus are significant and are not artifacts of noise or calibration errors. In addition, we demonstrated that our SED fits are robust against systematic uncertainties associated with temperature variation along lines-of-sight.

We extended our general analysis to the rest of Perseus, and we summarize our main findings as follows:

1. The most common dust temperature seen in Perseus clumps is $\sim$ 10.5 K, except in IC 348 where it is $\sim$ 11.5 K. The former temperature is consistent with the kinetic temperatures of dense cores observed with ammonia emission lines in

Perseus (∼11 K; Rosolowsky et al. 2008; Schnee et al. 2009), and the isothermal dust temperatures of prestellar cores seen in various clouds (∼10 K; Evans et al. 2001). IC 348 being slightly warmer than the rest of Perseus may be due to stellar heating from the nearby young star cluster.

2. Nearly all the local temperature peaks found in Perseus coincide with locations of embedded YSOs (and nearby B stars in the case of NGC 1333), which indicates local heating by these YSOs. The immediate region surrounding an embedded YSO can have temperatures of up to ~ 20 K whereas that near a B star can have temperatures up to ~ 50 K.

3. We found significant β variations over individual star-forming clumps. Most Perseus clumps have β values of $0.8 \lesssim \beta \lesssim 2.5$, similar to what Dupac et al. found in nearby star-forming clouds (2003; $1.0 \leq \beta \leq 2.5$) and what Yang & Phillips found in luminous infrared galaxies (2007; $0.9 \leq \beta \leq 2.4$). In NGC 1333, β values range upward to ~ 3. Maps of β, in general, appear well structured on a local scale, indicating that β is likely a function of its local environment.

4. We found β and T_d to be anti-correlated in all Perseus clumps, and that lower β regions tend to coincide with local temperature peaks. The found anti-correlations cannot be solely accounted by anti-correlated β and T_d uncertainties associated with our SED fitting. The dust grain's intrinsic β dependency on temperature (e.g., Agladze et al. 1996) may be partially responsible for the anti-correlation, but is not strong enough to be the sole cause. The sublimation of surface ice mantles, which can increase β when present on a dust grain (e.g., Aannestad 1975), may provide an explanation for the observed anti-correlation.

5. We also found coincidence between low-β regions and locations of bipolar outflows, suggesting that low-β dust may have originated from deep within a protostellar core, or even a starless core.

6. Similar to prior studies (e.g., Sandell & Knee 2001), we found cavities and peaks in derived column density maps that coincide with the ends of some outflow lobes, suggesting that these structures were carved out or compressed by local outflows, respectively. In addition, we also found lower column density valleys that run along paths of bipolar outflows, providing further evidence that outflows are capable of altering the local landscape of a star-forming clump. The

outflows also potentially provide significant feedback that could self-regulate the star-forming process. Creating column density maps from fitting SEDs with T_d, β, and τ, is important for this analysis.

7. The β distribution varies from one Perseus clump to another (see Figure 5.3). Binning β values into low, medium, and high values according to the behavior of β as a function of maximum grain size, a_{max}, calculated by Testi et al. (2014) revealed that the typical a_{max} value may also differ from clump to clump (see Figure 6.5). This result suggests that dust grain can grow significantly as the result of clump evolution. The high fraction of low β values and low fraction of high β values seen in L1455 suggests that L1455 may be the oldest clump in Perseus while the reverse scenarios seen in IC 348 and B5 may suggest that these two clumps are the youngest in Perseus.

8. By performing SED fits with β fixed at 2, a common value adopted in the literature (e.g., Hildebrand 1983), and T_d fixed at 10 K, the most common temperature we found in Perseus, our mean derived column density in NGC 1333 is a factor of 2.5 larger than that of the mean column density derived with β and T_d as free parameters. Most of the differences between the two derived column density maps were driven by the differences in T_d. This result illustrates that prior studies which assumed fixed β and T_d in deriving column densities, and thus mass, from single wavelength data can have fairly large uncertainties.

Following Sadavoy et al.'s (2013) pioneering work in mapping β values over a star-forming clump at angular resolutions of ~ 0.5 arcminute or less, our study presented here is the first of its kind to extend such analysis to the major star-forming clumps across a molecular cloud. In the Perseus, we found β values which are significantly different from the diffuse ISM values (i.e., ~ 2), indicative of dust grain evolution in the denser, star-forming ISMs. The discoveries of coherent small-scale, low-β regions, and their coincidence with local temperature peaks and outflows have provided some hints on origins of these low-β value grains. Further high-resolution observations of β toward protostellar cores and starless cores will help constrain some of our hypotheses regarding the origins of low-β grains. Studies on potential sublimation of ice mantles may also help to constrain the role of ice mantles on observed β variations. While we are confident that our results are robust against well-studied uncertainties associated with determining β through fitting SEDs, future investigations on how β variations

along the line-of-sight may affect the SED fits will be helpful in providing us with more definitive interpretations of our results.

Appendix A

Uncertainties Associated with CO Contamination

A large fraction of the uncertainty in our SED fits depends on the abilities of our observed flux in each wavelength bands to trace the same source of dust emission. In this appendix, we address the contribution of CO line emission in the SCUBA-2 850 μm band and the uncertainties associated with its removal. In Appendix B, we characterize the uncertainties associated with the spatial filtering of Herschel data, which is performed to ensure that our SCUBA-2 and Herschel data have the same spatial sensitivities. Following the investigation into uncertainties associated with SEDs, we discuss in Appendix C the uncertainties associated with our assumed dust opacity in deriving column densities.

Integrated CO lines are often brightest in active star-forming regions where many powerful outflows can be present. Since NGC 1333 is the most active star-forming region in the Perseus Molecular Cloud (Bally et al. 2008), we have chosen it over B1 as our testbed for determining the uncertainties associated with CO contamination and their removal. Performing tests on the most active star-forming regions should give good upper limit estimates of the effect of CO contamination across a molecular cloud like Perseus.

A.1 CO Contamination Levels

Figure A.1 shows the SCUBA-2 850 μm flux map of NGC 1333 overlaid with contours of the filtered CO map. Interestingly, the brightest CO structures seen in the Figure

have very little resemblance to the 850 μm structures. While the dust emission tends to trace the high column density material in the clump, the CO emission is clearly tracing something else. The bipolar, lobe-like morphologies of many CO features suggest that most of the filtered CO emission is due to outflows. Indeed, many of them were identified as such in earlier studies (e.g., Knee & Sandell 2000; Hatchell & Dunham 2009, Drabek et al. 2012). Most of the bright CO features have fairly broad line widths, typically 5-15 km/s including extended line wings when present. The only brightest CO structure with a narrow line comparable to the thermal line widths has a high peak intensity, e.g., up to ∼60 K measured in peak main-beam temperature. This particular CO structure is located near the B star BD +30 549 and is likely related to gas thermally heated by the B star. In general, the integrated, filtered CO line flux in NGC 1333 is only significant with respect to the SCUBA-2 850 μm flux when the CO 3-2 line has very broad widths or is very bright, consistent with the findings of Johnstone et. al. (2003).

Figure A.2 shows the histogram of the filtered, integrated CO flux as a fraction of the 850 μm flux in NGC 1333. In other words, Fig. A.2 shows the fractional level of CO contamination. Only pixels with 850 μm fluxes equal to or more than 10 times the RMS noise are included in the sample, in accordance with the minimum flux threshold of our SED fittings. As can be seen, over 95% of the pixels have less than 20% CO contamination and about 90% of the pixels have less than 10% CO contamination. These levels of CO contamination are relatively insignificant given that they are comparable to or less than the flux uncertainty of our data (10%). In a few pixels the contamination is significant, i.e., $\sim$ 55%. This finding is consistent with previous studies done by Drabek et al. (2012) in NGC 1333 towards identified sub-millimetre cores observed with SCUBA-2 and HARP. In their study, all the NGC 1333 cores have fluxes with less than 12% CO contamination, and typically below 6% . Drabek et al. did find, however, a few cores with much higher levels of CO contamination in NGC 2071 and NGC 2024 of the Orion B molecular cloud. In those cases, the contamination was as high as $\sim$ 80%. The majority of the cores studied by Drabek et. al., however, had less than $\sim$ 10% CO contamination, across the three regions they studied.

A curious feature seen in Fig. A.2 is the large fraction of pixels (∼40%) with "negative" CO contamination. A large fraction of these "negative" CO pixels are $> -15\%$, indicating that the "negative" CO contributions to these pixels are not insignificant. Figure A.3 shows the filtered CO flux plotted against the 850 μm flux.

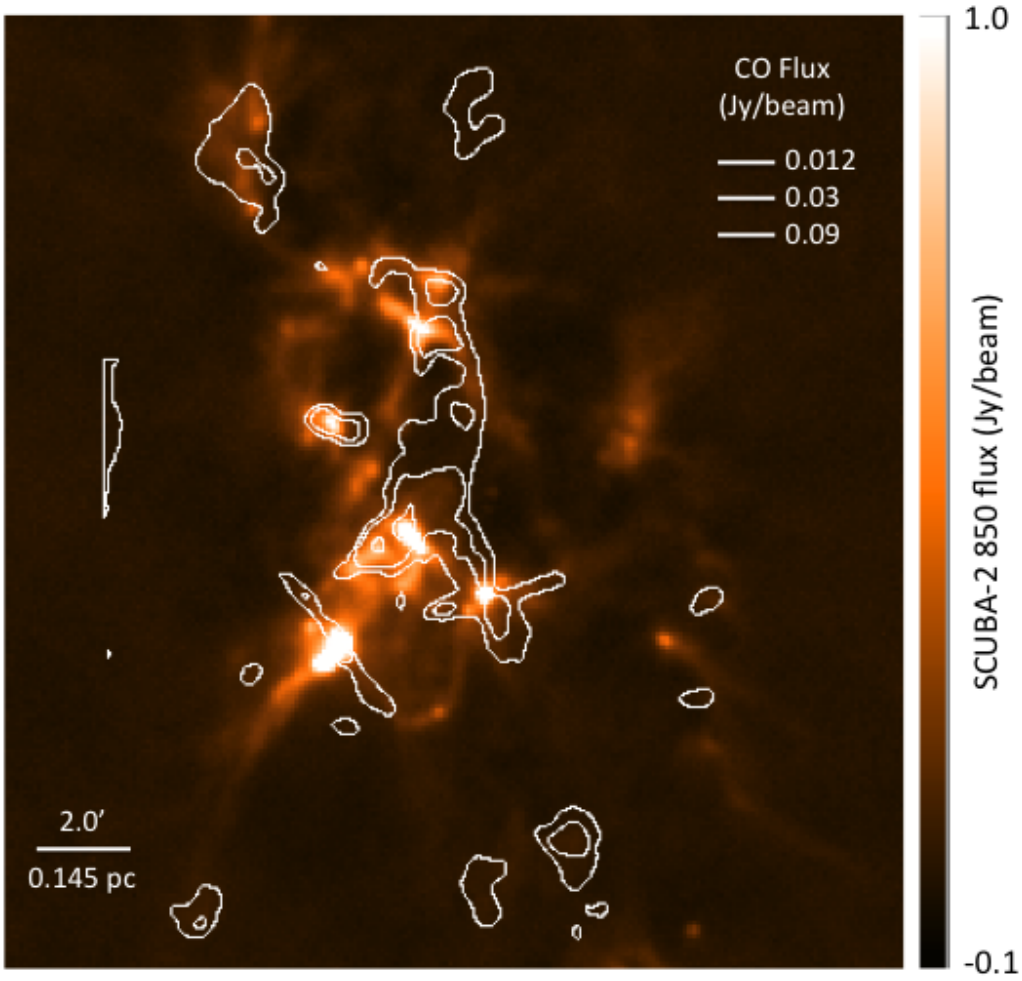

Figure A.1 NGC 1333 observed in the SCUBA-2 850 μm band. The contours show the spatially filtered HARP ^{12}CO 3-2 integrated line intensity map. The contour to the east of the map with a straight, vertical edge is an artifact associated with the edge of the HARP CO observations and is not a real feature.

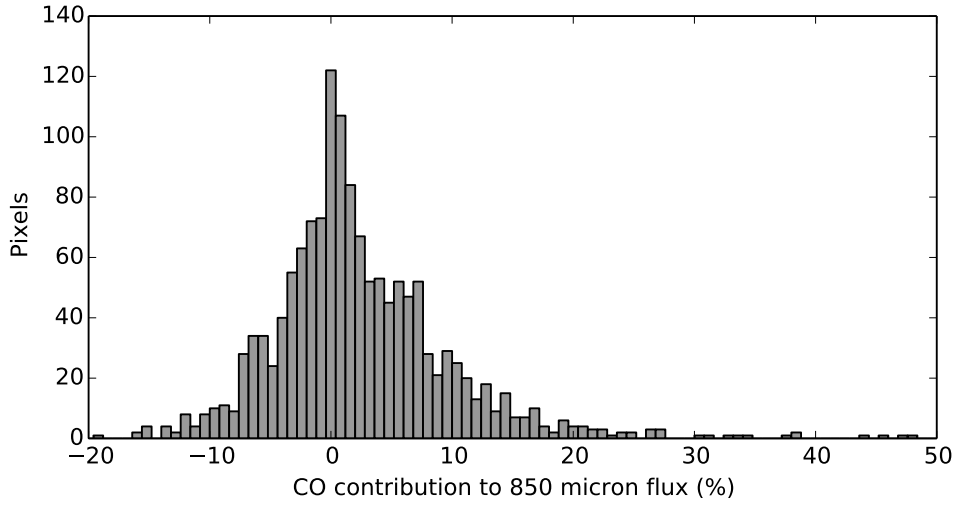

Figure A.2 Histogram of the filtered integrated CO intensity as a fraction of SCUBA-2 850 μm flux. This histogram only samples pixels that have 850 μm fluxes 10 times the RMS noise.

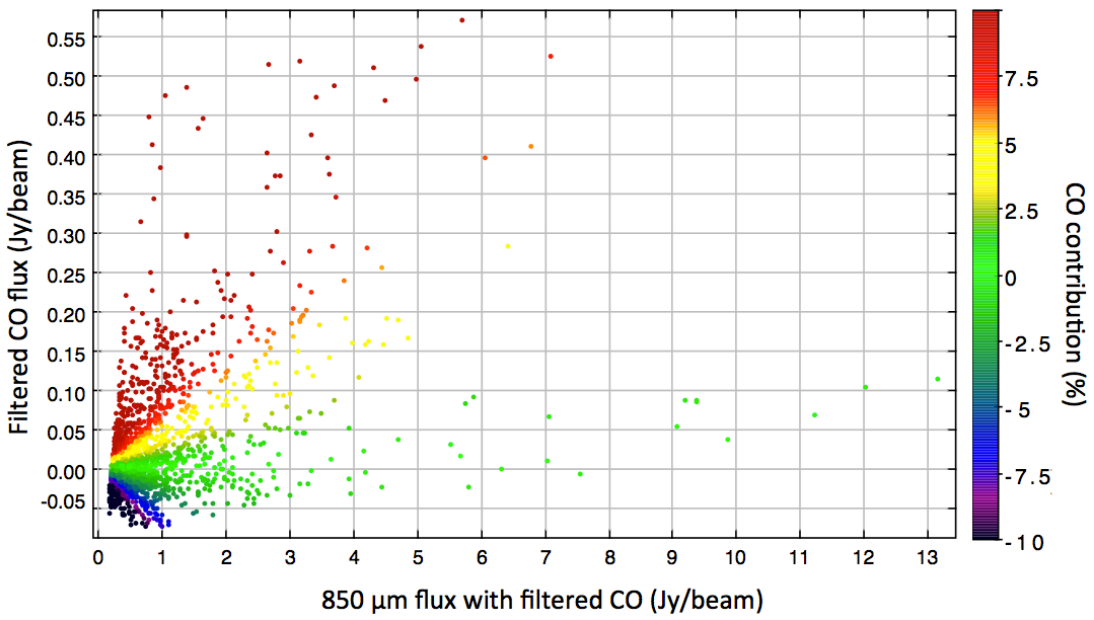

Figure A.3 A scatter plot showing filtered CO flux plotted against the SCUBA-2 850 μm flux. The points are color-coded as the percentage contribution of the filtered CO flux to the 850 μm flux.

As can be seen, the pixels with "negative" fluxes within the $\sim -10\%$ level all have 850 μm fluxes below 0.8 Jy/beam. Positive CO contamination that is above 10% can affect pixels with 850 μm flux that are as high as 7 Jy/beam.

Some of the minor artifacts created by the SCUBA-2 map-maker are the "bowling features," which are regions of apparently negative flux surrounding bright sources. The data reduction process that created these features is likely responsible for over-removing the CO fluxes along with the SCUBA-2 fluxes, resulting in many pixels in the filtered CO map having negative values. While the data reduction recipe developed by the JCMT GBS data reduction team has aimed to minimize these bowling effects, these effects can be still fairly prominent when it comes to filtering integrated CO maps. Additionally, the integrated CO maps typically cover areas smaller than the SCUBA-2 maps, and possess clear, sharp edges since the integrated, unfiltered CO emission can be fairly bright throughout most of a CO map. Filtering near these edges can introduce further minor artifacts. If indeed the case, the regions of molecular clouds with less overall CO contamination should experience less bowling induced by the edge of the integrated CO map.

Since bowling is introduced in both the CO and the SCUBA-2 map together

during the data reduction process as a single map, the additional flux introduced by the removal of "negative" CO flux, to an extent, is compensated by the SCUBA-2 flux removed by the bowling. The error introduced by the bowling seen in the CO map should therefore be relatively small. In the next subsection, we demonstrate why "negative" CO emission in the SCUBA-2 850 μm band does not contribute significantly to the uncertainties of the SED fitting performed on the combined data observed with JCMT and Herschel.

A.2 Effects of CO Contamination on the SED fittings: Towards Bright CO Sources

We studied the effect of CO contamination on the SED fittings by performing tests on three different sets of NGC 1333 data that differ only in the treatment of removing CO emission from the SCUBA-2 850 μm map. In two of these cases, filtered CO and non-filtered CO are subtracted respectively from the 850 μm map. In the third case, no subtraction occurred and the 850 μm map was kept intact. Figure A.4 shows the histograms of the derived temperature, β, and τ_{300} in these three cases. The histogram of the filtered-CO-removed case (filled grey) closely resembles that of the non-CO-removed case (black line) in all three of the fitted parameters. This shows that CO contamination in the 850 μm band is largely insubstantial in deriving the global properties of the NGC 1333 clump, and, as we discuss later, it is only significant in locations with additional heating or bright outflows. Since NGC 1333 is the most CO contaminated clump in Perseus, CO contamination is likely insignificant for other Perseus clumps.

The histograms of the non-filtered-CO-removed case is noticeably different from the histograms of the other two cases. The derived temperature and β values for the non-filtered-CO-removed case are shifted down by $\sim$ 1 K and $\sim$ 0.6, respectively. The overall shape of these histograms are fairly similar to the other two cases, with the β distribution becoming more centrally peaked than its counterparts. The column density histogram shows a redistribution of many pixels from the lower column density peak towards the high column density tail. Overall, the column density increases for the non-filtered-CO-removed case. Interestingly, if the CO emission is removed from the SCUBA-2 850 μm data without being spatially filtered, it can introduce more error to the SED fits than if no CO emission is removed. This behavior suggests

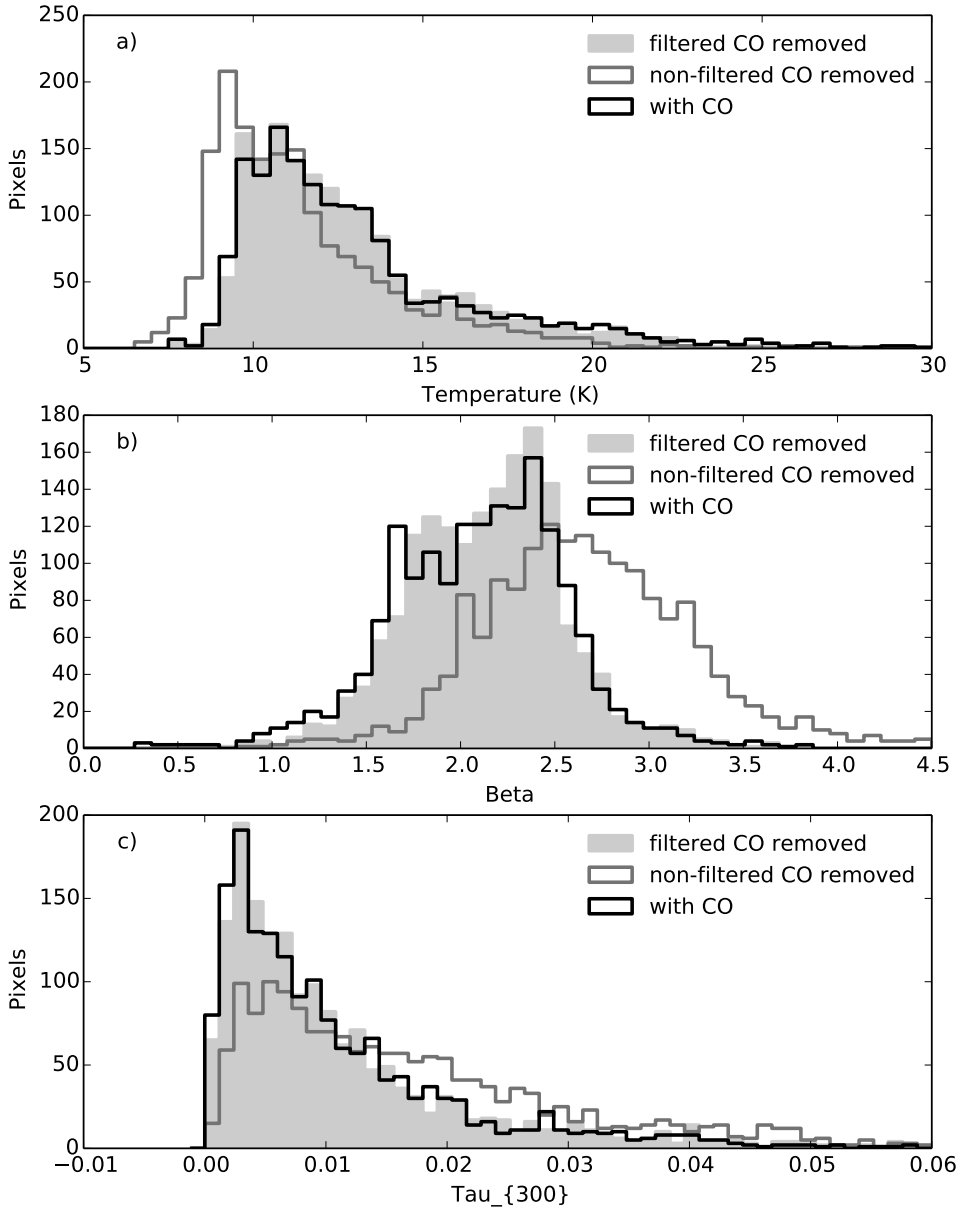

Figure A.4 Histograms of derived a) temperatures, b) β , and c) τ_{300} in NGC 1333 drawn from SED fits in cases where the SCUBA-2 850 μm data had spatially filtered CO removed, non-filtered CO removed, and no CO removed.

that most of the CO emission present in the SCUBA-2 850 μm data were already spatially filtered out during the data reduction process, leaving only the small scale CO emission behind in the reduced SCUBA-2 850 μm maps. The extensive filtering of CO emission is perhaps largely responsible for why the CO contamination appears to be fairly insignificant for the SED fits at the global level. After all, the bright and compact CO emission only occupies a small fraction of the map where SED fits were performed.

It is critical, therefore, that CO emission be spatially filtered in the same way as the SCUBA-2 850 μm data before it is removed from the SCUBA-2 map. The un-filtered CO map clearly overestimates the CO contamination present in the SCUBA-2 map. Attempts to remove un-filtered CO will result in over-subtraction of the CO flux, introducing greater error to the SCUBA-2 map than the original CO contamination present in the SCUBA-2 map.

While CO contamination in SCUBA-2 maps has very little influence on the SED fittings globally across a clump, its influence may be still fairly significant at specific locations within a map. The brightest CO sources, such as bipolar outflows, tend to be fairly compact in nature and thus are unlikely to be filtered out with the large-scale emission. If such bright CO emission happens to be projected over relatively faint dust continuum emission, it can become a significant source of contamination in terms of percentage. To investigate the local effects of these compact CO structures on the SED fits, we focused on the changes to the derived parameters over these compact structures. In particular, we sampled CO emission that appears to be visually associated with the same CO structure or a set of structures that share a common origin, such as the two lobes of a bipolar outflow. Most of the bright CO sources we identified are outflows discussed by Curtis et al. (2010b) in their JCMT HARP survey over the different Perseus clumps. These sources have broad line widths that are expected from outflows. Only two of the bright CO sources we identified have fairly narrow line widths but exceptionally high intensities. As described earlier, these CO sources are likely radiatively heated by nearby B stars.

Figure A.5 shows the increase in derived temperature as the result of CO contamination over several bright CO sources we identified. As can be seen, the change in the derived temperature has a non-linear dependency on the fraction of CO contamination. Pixels that have up to $\sim$ 10% of CO contamination experience changes of $\sim$0.3 - 2 K, which are relatively low given that their respective clumps are typically around 10 K in temperature. The severity of the CO contamination, however,

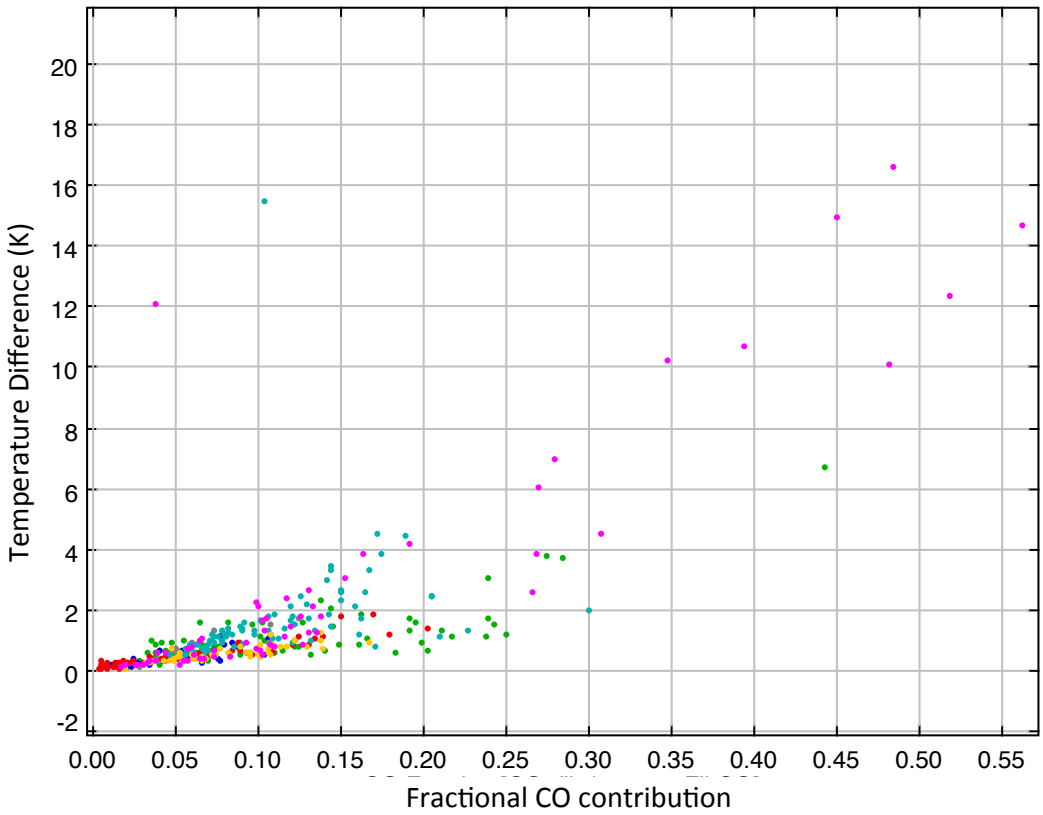

Figure A.5 The change in temperature plotted against the fractional levels of CO contamination sampled over the bright CO regions. The temperature change is the difference of the non-CO removed case subtracting the filtered-CO removed case. The CO fraction is the flux of the filtered CO divided by the flux of the original SCUBA-2 850 μm flux. The 8 bright, distinct CO structures, e.g., outflows, identified by eye are individually colored.

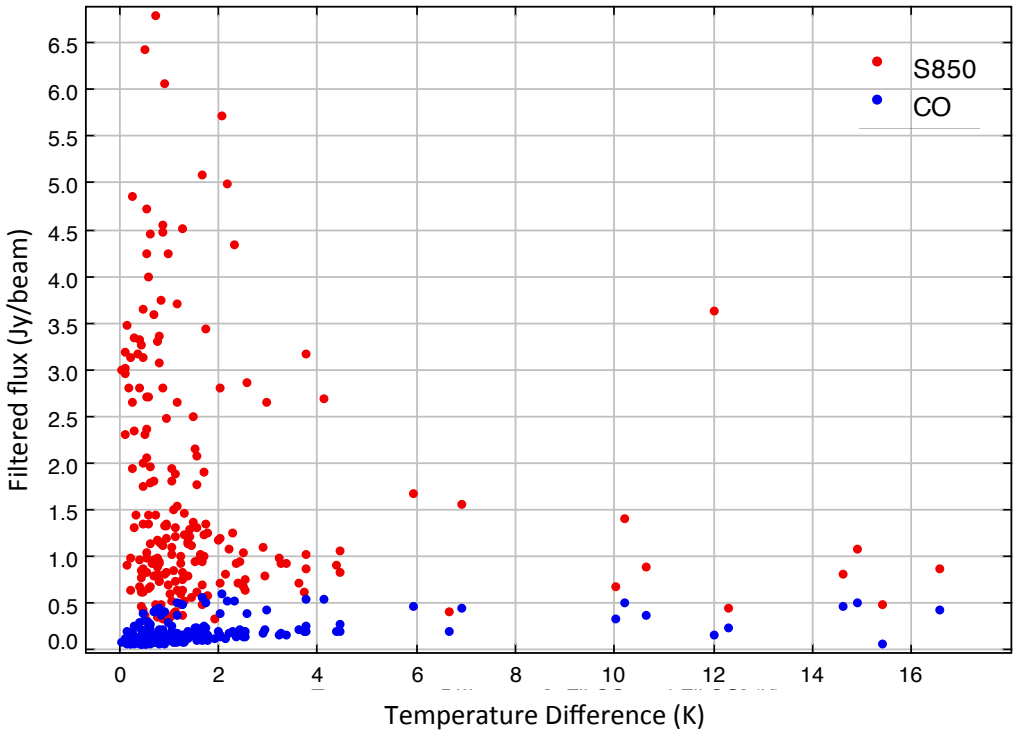

Figure A.6 The filtered CO flux and SCUBA-2 850 μm flux plotted against the increase in temperature due to CO contamination. The filtered CO flux and the SCUBA-2 flux are colored blue and red, respectively. The temperature increase is the difference in temperatures of the non-CO removed case minus the filtered-CO removed case.

increases dramatically above the ∼10% level. The overestimation of temperature can be as high as ∼16 K at a contamination level of ∼50%, the upper end of the CO contamination percentage levels seen in NGC 1333. It should be noted that higher CO contamination percentages have been seen in other star-forming regions before (Drabek et al. 2012). As Figure A.5 shows, however, most of the CO emission coming from the bright CO sources contributes no more than ∼20% of the contamination. Since derived temperature is the parameter most sensitive to CO contamination, we can use it as a proxy to study the effects of CO contamination on SED fits.

Figure A.6 shows the filtered CO flux and SCUBA-2 850 μm flux plotted against the increase in temperature due to CO contamination. As can be seen, some pixels that are the brightest in CO happen to have very bright SCUBA-2 850 μm flux as well. This coincidence explains why most pixels that contain parts of bright CO sources do not experience contamination levels above ∼20%. Contamination percentages only

rise above 20% when CO sources overlap faint 850 μm sources.

A.3 Effects of CO Contamination on the SED fits: Towards Bright SCUBA-2 Sources

Bright and compact dust continuum emission sources are often the focus of many studies because they trace the densest objects in a molecular cloud that may eventually collapse to form stars. Accurate measurements of their dust emission flux is thus crucial for deriving their mass and temperature and consequently assessing their gravitational stability. For these reasons, we specifically sampled many bright SCUBA-2 850 μm sources in NGC 1333 to estimate the level of CO contamination in them. In our sample, we selected individual 'blobs' in the convolved SCUBA-2 850 μm map that contain at least a few pixels above 1 Jy/beam, which is roughly a factor of 50 greater than the RMS-noise in the map. While this criterion does not pick out all the dense cores that are visible in the map, it does provide a good representation of the brightest cores. Seventeen SCUBA-2 sources (i.e., cores) identified by Hatchell et al. (2005) are included in our sample.

Figure A.7 shows the increase in derived temperature as the result of CO contamination over the identified bright SCUBA-2 850 μm sources. All the selected regions containing SCUBA sources identified by Hatchell et al. (2005) have been labeled accordingly. The largest change in temperature at the 10% and the 16% level of CO contamination are ∼2 K and ∼4 K respectively, where 16% is the highest level of CO contamination found towards our sample of bright SCUBA-2 850 μm sources. Out of the nine bright SCUBA-2 sources, only one of them sees a temperature change above ∼2 K. This result shows that CO contamination is a relatively small, but not negligible, source of error for fitting SEDs of the brightest SCUBA-2 sources.

To determine the cause of the spread seen in the temperature difference due to the level of CO contamination shown in Figs. A.5 and A.7, we sampled a few SEDs from the upper and lower ends of the spread, towards higher levels of contamination. We found that SEDs less affected by CO contamination tend to resemble a modified blackbody more when the CO contamination was not removed. Upon closer examination, pixels that have less temperature difference at the same percentage level of contamination tend to have higher SCUBA-2 850 μm fluxes as well. Therefore, the spread in the temperature difference can be largely attributed to the quality of the

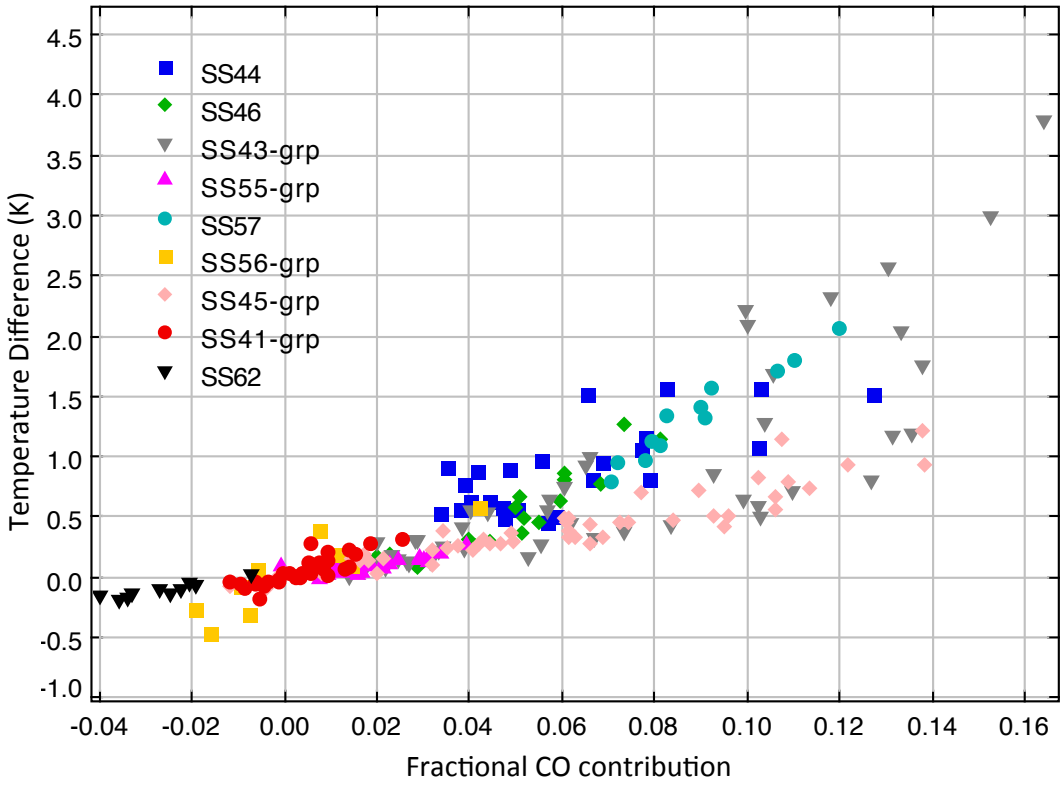

Figure A.7 The change in temperature plotted against the fractional levels of CO contamination sampled over selected bright SCUBA-2 850 μm regions. The temperature change is the difference of the non-CO removed case minus the filtered-CO removed case. The CO fraction is the flux of the filtered CO divided by the flux of the original SCUBA-2 850 μm flux. Distinct SCUBA-2 sources identified by eye are individually color-coded.

data, i.e., the signal-to-noise ratio.

In summary, our testing of the impact of CO contamination on fitting SEDs has revealed the following:

1. CO contamination has a fairly negligible impact on derived parameters on the global scale of a star-forming clump.

2. CO contamination could be a severe problem on the local scale, where the percentage contamination could be much higher than typically found on a global scale.

3. Using derived temperature as a proxy, we found that CO contamination becomes significant for fitting SEDs when the CO flux contributes more than $\sim$10% of the total SCUBA-2 850 μm flux.

4. CO contamination percentages toward the brightest SCUBA-2 850 μm sources tend to be lower than $\sim$10%. Contamination levels are more severe in regions where bright CO structures, such as outflows, overlap with the fainter SCUBA-2 850 μm sources.

Appendix B

Uncertainties associated with filtering Herschel Data

B.1 Uncertainties associated with flux scaling

To quantify the uncertainties associated with the arbitrary scaling factor of the Herschel flux, we performed several tests. To start, upper and lower limits to what the Herschel flux could be scaled were found. These limits are based on rough estimates on how brightly the dust of a typical star-forming clump can emit within typical ranges of reasonable dust temperatures and spectral indices. Assuming a column density of 2.5×10^{22} cm^{-2} (typical for the Perseus B1 clump), a range of β of 1 - 4, and a range of T_{dust} of 5 - 40 K, the flux in the sub-millimetre bands can be factors of $\sim$0.01 - 500 greater than the typical values seen with Herschel. Since fluxes that are lower than 0.01 times of their typical values are most likely below the detection threshold of SCUBA-2, only scale factors from 0.1 - 500 are considered.

Maps of the Perseus B1 region in the Herschel 500 μm band and the 160 μm band were used to see if the shape of the Herschel emission, in addition to scaling factors, has any influence on the filtering process. These bands were chosen because their emission most or least resembles the SCUBA-2 850 μm emission, respectively. The tests filtered the Herschel 500 μm and 160 μms maps using the SCUBA-2 mapmaker in the same way as the standard procedure, with scaling factors set to 0.1, 1, 10, 50, 100, and 500. For convenience, we henceforth refer to these scaling factors as "fakescales."

For the Herschel 500 μm band (Her500), we found the flux differences between the

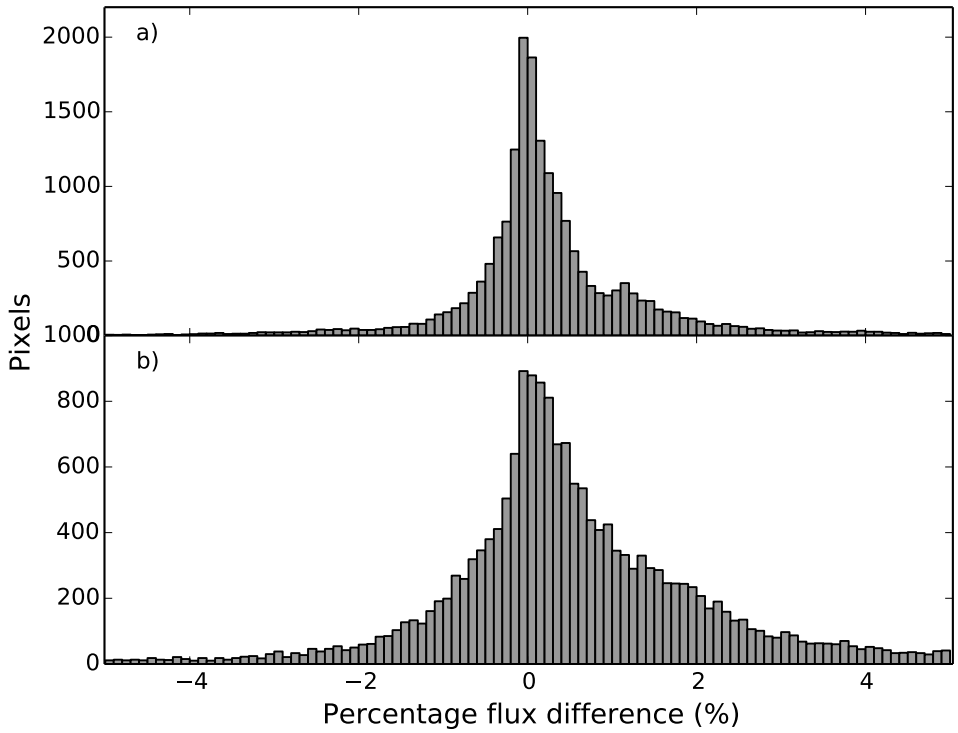

Figure B.1 Histograms of the percentage flux difference, at a) 500 μm and b) 160 μm, between maps filtered with fakescale=500 and fakescale=1, with respect to the maps filtered with fakescale=1.

filtered maps of fakescale=500 case and fakescale=1 case to be less than 3% of the fakescale=1 fluxes. The percentage quoted here corresponds to the half width of the distribution that encompasses roughly 95% of pixels that have the closest percentage differences to zero. The distribution of percentage difference can be seen in Fig. B.1a. It is worth noting that the shape of the flux percentage difference histogram between a given test fakescale and fakescale=1 converges above fakescale=10. At fakescale > 10, the Her500 μm flux dominates over the SCUBA-2 850 flux, making the 850 μm flux negligible to the map making process. For fakescale < 1, the flux difference between the fakescale=0.1 and the fakescale=1 cases is less than 1%.

For the Herschel 160 μm band (Her160), we found the 'typical' flux difference between the filtered maps of fakescale=500 and fakescale=1 to be about 4%. This half width is just slightly greater than its Her500 counterpart. The corresponding percentage flux difference can be seen in Fig. B.1b. The flux difference between fakescale=0.1 and fakescale=1 cases is less than 3%. As expected, the percentage flux

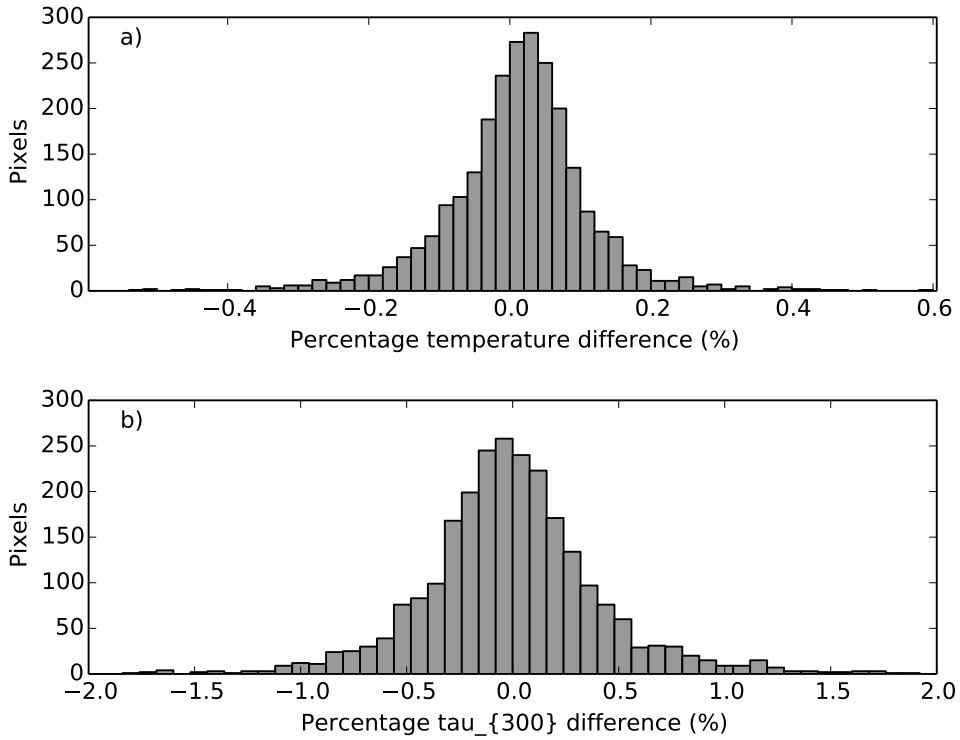

Figure B.2 The percentage a) temperature and b) τ_{300} difference obtained from SEDs drawn from filtered Herschel data with fakescale=0.1 map and fakescale=1, with respect to the values obtained from the fakescale =0.1 case.

differences found in the Her160 case are greater than the Her500 case, but only slightly. The difference is likely because the Her160 emission resembles less the SCUBA-2 850 μm emission than does the Her500 emission. Thus, when the Herschel + SCUBA-2 map is being reduced with the map-maker, it will deviate further from the SCUBA-2 map at 160 μm than at 500 μm.

From these tests, we conclude that the flux uncertainties associated with using an arbitrary fakescale for Herschel data filtering is typically around 4% for imaging dust emission in nearby star-forming regions. As demonstrated, these uncertainties will be slightly lower for the Herschel bands at longer wavelengths since these uncertainties are associated with how well each Herschel band resembles the SCUBA-2 850 μm map. Thus, if the emission seen in the Herschel bands traces a very different dust population than the SCUBA-2 850 μm map, these uncertainties are expected to be higher.

To test how the fakescale uncertainties affect fitting SEDs drawn from filtered maps, we fit SEDs containing only filtered Herschel data with fakescale = 1 and fakescale = 0.1. Since we do not include the SCUBA-2 data here, we have set $\beta = 2$ to constrain better the fitting with only the temperature and the optical depth being the free parameters. The resulting differences between the two fakescale cases are small, with the typical temperature difference being less than 0.5% and the typical optical depth difference being about 1% (encompassing >95% of the pixels difference closest to zero percent). Histograms of these percentage differences are shown in Fig. B.2a and B.2b, respectively. As can be seen, the uncertainties of the SED fitting attributed to the choice of scaling factor is very small, and we adopted a scaling factor of 0.1 for all our analyses.

B.2 Uncertainties associated with the choice of mask

As mentioned in Section 2.1, the SCUBA-2 map-maker uses masks when reconstructing astronomical signals in a map. The JCMT GBS SCUBA-2 maps were reduced twice, first using the SNR based masks that were automatically generated at each iteration of the map-making process, and again with the SNR-based mask generated from the mosaicked map of the first reduction, with some manual modifications. Naively, the same procedure can be applied to the Herschel filtering process to ensure that small-scale astronomical signals found in the Herschel bands but not in the SCUBA-2 band are not filtered out along with large-scale structures. A potential problem with this approach, however, is that there is not a clearly defined way to scale the Herschel data when they are inserted into the SCUBA-2 data for filtering. Indeed, the auto-mask can vary drastically depending on the scaling factor, because auto-masks are estimated using the SNR found in the SCUBA-2 + Herschel map.

To see if the auto-masking option should be entirely avoided for the Herschel filtering, we performed a few tests to quantify the uncertainties associated with using the auto-masking option under two different Herschel scaling factors (fakescales). As discussed earlier in Appendix B.1, a fakescale of 1 and 100 are good values to test because the two respectively represent the typical values and the upper limits of the flux that one would expect to observe in star-forming clouds with SCUBA-2. Since Herschel 500 μm emission (Her500) resembles the SCUBA-2 850 μm (S850) emission the most, we picked its map for this particular filtering test. Due to this similarity, the uncertainties estimated from this test should only be regarded as lower limits. As

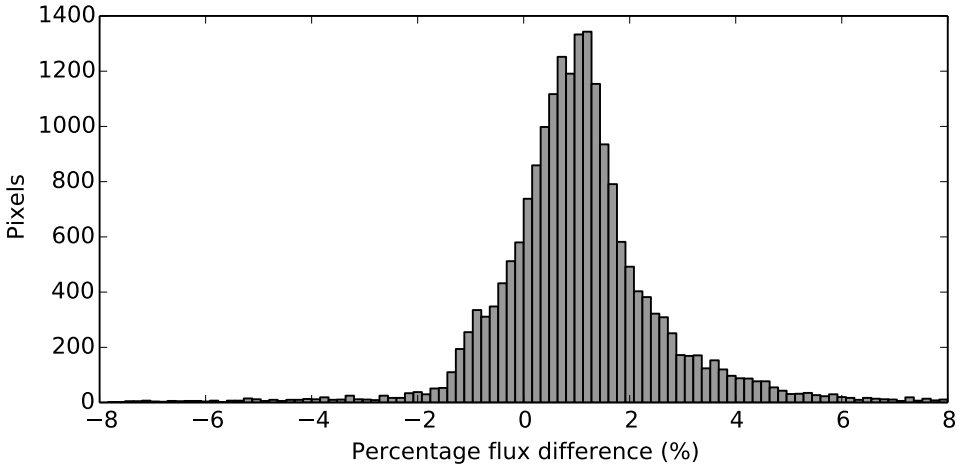

Figure B.3 A histogram of the percentage flux difference between Herschel 500 μm maps filtered with auto-mask with fakescale=100 and fakescale=1, with respect to the fakescale=1 case.

before, the reductions were run until the map-making iterations converged.

Figure B.3 shows the percentage difference between the masked and unmasked 500 μm maps found within the 1-σ auto-masked region of the fakescale=1 map. The distribution of these flux differences has a half width of about 3% in which more than 95% of the pixels fall within. This value is just slightly higher than the largest uncertainties associated with the filtering of Her500 maps using a fixed external mask ($< 3\%$), and a bit lower than ones associated with the same filtering method used on the Her160 maps (4%). Correspondingly, the width of the percentage difference distribution is probably a bit worse than $\sim 4\%$ for the most extreme case of the Her160 band.

In addition to the $\sim 4\%$ uncertainty associated with the fakescale, the offset of the distribution from centring at zero to 1% demonstrates a systematic uncertainty, suggesting an increase in fakescale can result in an increase in the flux retained after filtering. This result is unsurprising given that auto-masks were generated based on the SNR seen in the map. When the fakescale is increased, the inserted Herschel map becomes brighter with respect to the rest of SCUBA-2 map. This increase in brightness allows more Herschel flux to rise above the SNR threshold of the auto-mask, thus making the auto-masked region larger. Since the mapmaker treats emission within the mask as being astronomical in nature, a larger mask results in less filtering.

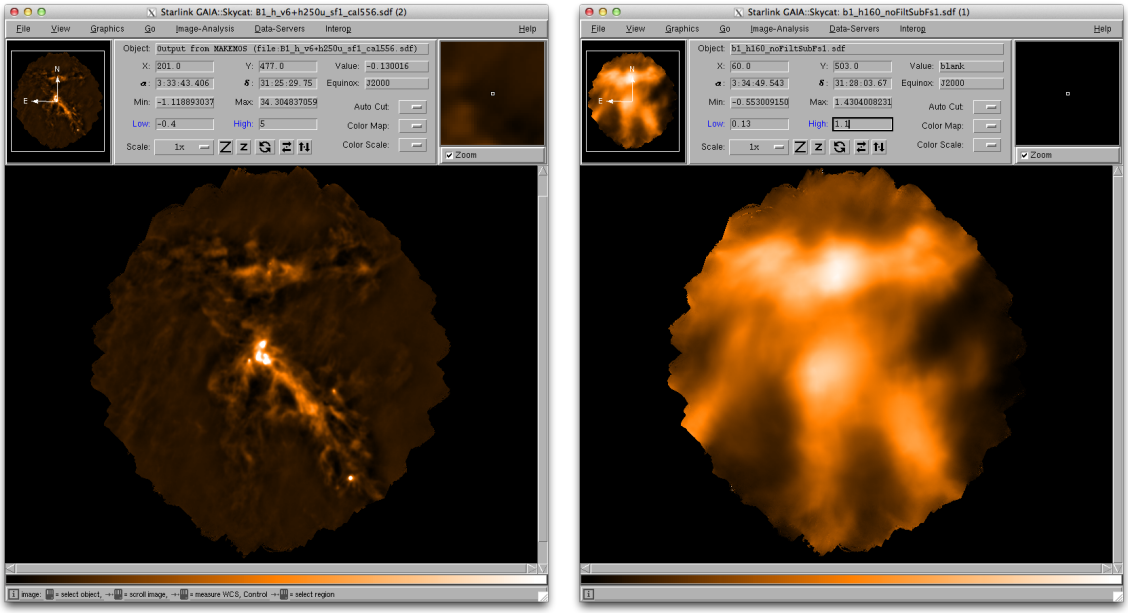

(a) (b)

Figure B.4 Left: The Herschel 250 μm map after spatial filtering through SCUBA-2 map-maker; Right: The Herschel 250 μm flux *removed* by the spatial filtering of SCUBA-2 map-maker. The color scale of the two panels are different from each other. The color scale of the left panel is stretched between -0.4 and 5 Jy/beam while the color scale of the right panel is stretched between 0.13 and 1.1 Jy/beam.

Even though a systematic error of 1% is small relative to the other uncertainties found in our data, the behavior of this error has not been well understood or quantified. In the absence of a reliable way to correct or constrain this uncertainty, we have thus decided to omit the usage of auto-masking in our Herschel filtering process. The external masks that were used to produce the final JCMT GBS SCUBA-2 maps were used instead. This eliminates the two-fold uncertainties of the auto-masking across the filtered Herschel bands and ensures that the error associated with masking is at least consistent over the pixels where we fit SEDs.

B.2.1 The effects of filtering Herschel flux

The lack of atmospheric effects in Herschel observations allowed the large-scale continuum emission found in star-forming regions to be detected. This large-scale emission traces the more extended and diffuse dust (and associated gas) compared to the more compact structures. Figure B.4 shows the compact Herschel 250 μm emission that is

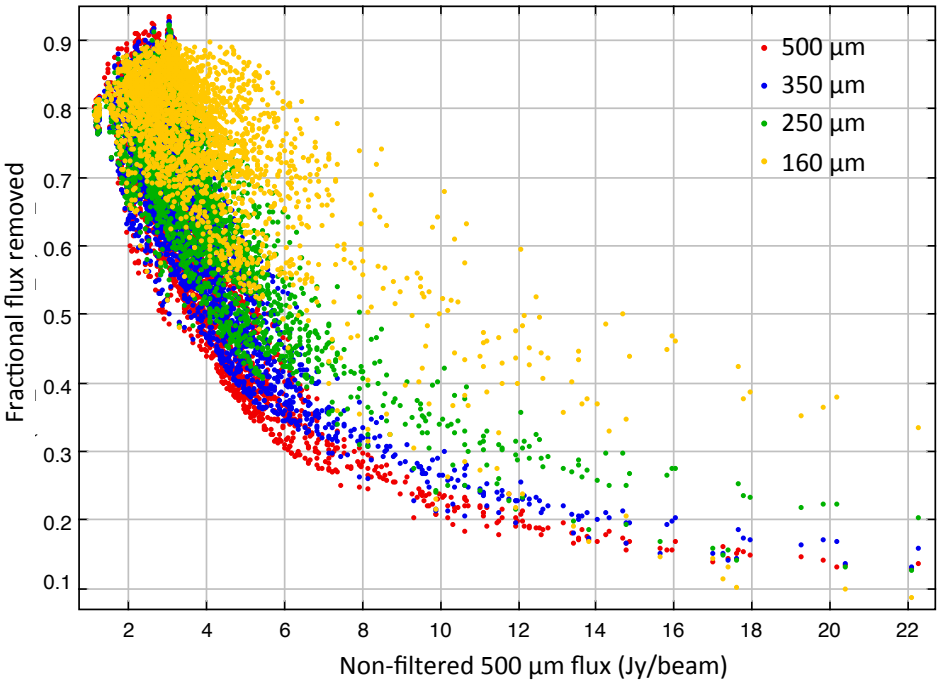

Figure B.5 The filtered-out emission, as a fraction of non-filtered flux, plotted against the non-filtered 500 μm fluxes. The filtered-out fluxes are color-coded by their respective Herschel bands. The fluxes plotted here are those observed in the B1 region. Only pixels with fluxes 10 sigma above the RMS noise are included in this sample.

retained after filtering through SCUBA-2 map-maker, as well as large-scale emission removed by the filtering.

The dust traced by the more compact emission may be expected to be colder because it is mixed with denser gas and better shielded from the local interstellar radiation field. Intuitively, filtering out the large-scale emission should then preferentially filter out warmer dust. Since the modified blackbody function behaves very similarly to the Planck function, the warmer dust should contribute more flux at shorter wavelengths than at longer ones. Hence, if the large-scale emission does indeed trace warmer dust, then the large-scale filtering should preferentially filter out more flux at shorter wavelength bands. Indeed, Fig. B.5 where the removed fluxes, expressed as a fraction of the non-filtered fluxes, are plotted against the non-filtered 500 μm fluxes for each of the wavelength bands observed in B1 regions demonstrates this expectation. Since the dust temperature derived from SED fits represents a weighted average along the line-of-sight, spatial filtering should make the derived

temperatures lower compared to those derived from the non-filtered maps.

B.3 The effects of filtering on SED-derived parameters

SEDs drawn from the filtered and the non-filtered Herschel maps of B1 were fit separately to examine the impact of spatial filtering on derived parameters. SCUBA-2 data were not included because spatial filtering is a necessary part of their data reduction. Without SCUBA-2 data as a needed constraint, we again assumed a β value of 2 throughout the map. The derived temperature and β values for both cases are shown in Figures B.6. As expected from reasons described in B.2.1, Fig B.6a shows an overall drop of derived temperature by about 1.5 K after spatial filtering. Interestingly, pixels with derived temperatures above 15 K appear to be relatively unaffected. As can be seen in Figure 5.2, the hottest regions found in B1 are locally heated by embedded YSOs, and thus are unaffected by the spatial filtering due to their intrinsic compactness.

Since spatial filtering removes emission coming from larger structures, a drop in the derived column density would be expected after spatial filtering. As seen in Fig B.6b, this situation is indeed the case. The convergence of the two distributions towards the higher column density end shows that the highest column density regions are relatively unaffected by the spatial filtering. Indeed, the highest column density regions tend to be the brightest and most compact structures and so tend to remain relatively unaffected by spatial filtering. Physically, most of the larger-scale structures removed by the filtering process are likely emitted by dust found in diffuse gas in the foreground and background of the denser, more compact gas that tends to contain most of the mass along the line of sight. In light of this, the derived column densities may differ significantly between the filtered and non-filtered cases at locations with lower column densities.

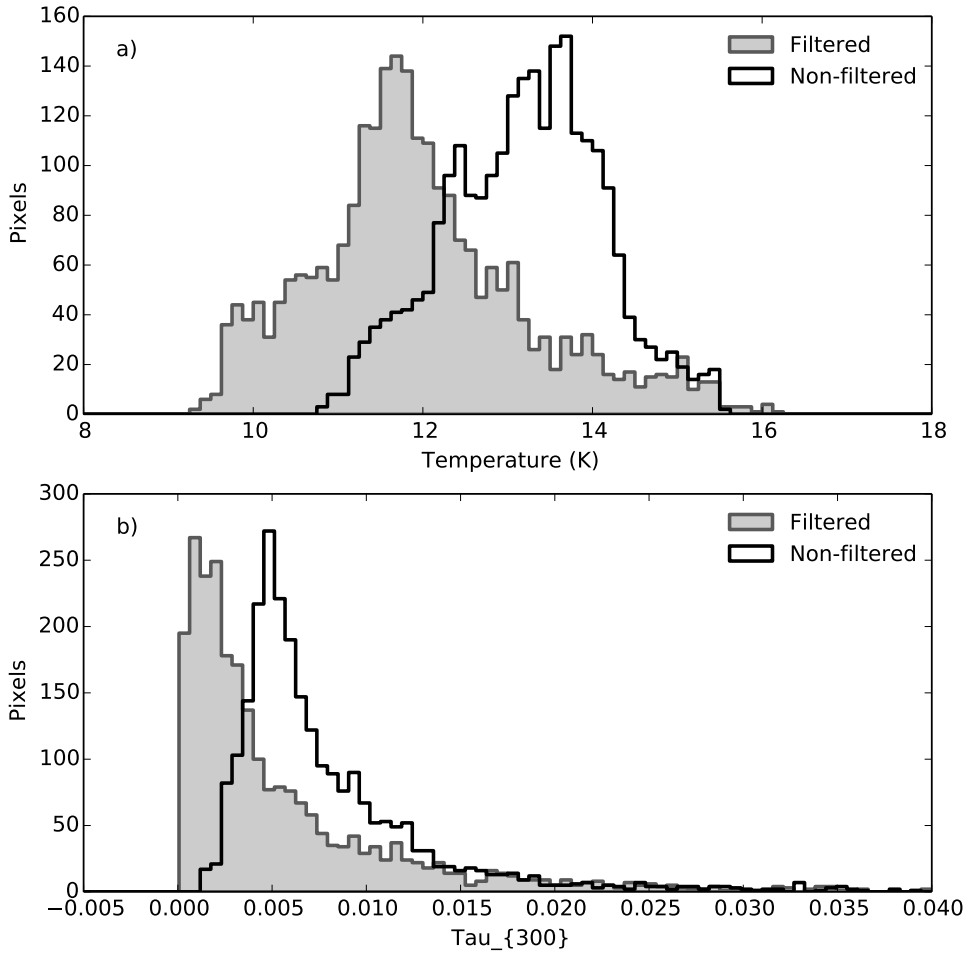

Figure B.6 Histograms of a) temperatures and b) τ_{300} derived from fits to SEDs drawn from filtered and non-filtered, Herschel-only data.

Appendix C

Uncertainties Associated with Dust Opacity

Equation 3.2 shows that deriving column density from the fitted optical depth $\tau_{\nu 0}$ requires assumptions on two additional parameters: the mean molecular weight μ and the reference dust opacity κ_{ν_0}. Out of these two, κ_{ν_0} is much more uncertain.

Figure C.1 shows the commonly used Ossenkopf & Henning's dust opacity model (OH5, 1994) as a function of wavelength for various conditions for grain growth, assuming a gas-to-dust mass ratio of 100. Without prior knowledge on the thickness of ice mantles, the modelled dust opacity at a given wavelength, κ_{ν_0}, can differ by as much as factors of 3 to 7 at a given wavelength within the range between 100 μm and 1000 μm. Most of these differences in the calculated dust opacities are contributed by the no-ice mantle model. If that particular model is excluded, then the differences between modelled dust opacities are typically between factors of 1.5 and 3.

The mean κ_{ν_0} value for different models with a given ice mantle thickness intersects near 280 μm, making this wavelength a good place to reference κ_{ν_0} without biasing towards any specific ice mantle thickness. The value of $\kappa_{300} = 0.1$ cm^{-2}g^{-1}, assumed by us and many others including the Herschel GBS team (André et al. 2010), is referenced fairly close to this wavelength and closely resembles the case of thin ice mantle grain growth inside an environment with gas densities of 10^5 cm^{-3}. At this wavelength, the modelled κ_{300} can range between 0.08 - 0.3 cm^{-2} g^{-1}, which equals differences of up to -20% and 200% when compared to the assumed 0.1 cm^{-2}g^{-1}. Since column density is inversely proportional to κ_{ν_0}, as seen in equation 3.2, our derived column density will have uncertainties correspondingly in the range of $\sim$

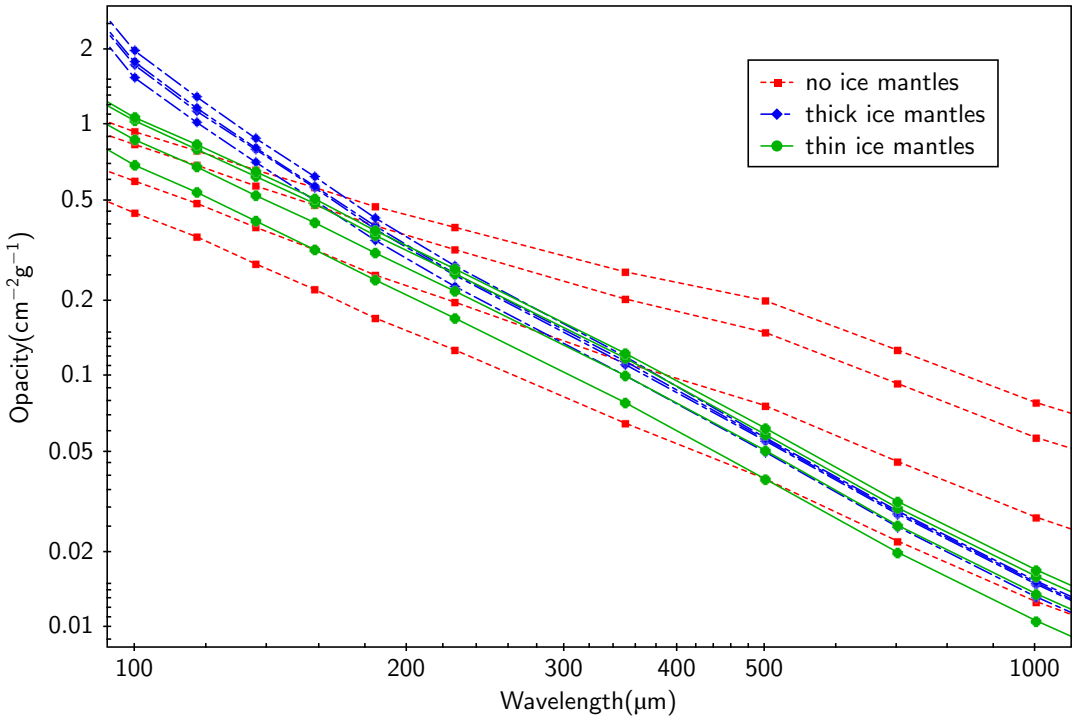

Figure C.1 Ossenkopf & Henning's model of dust opacity per unit (dust + gas) mass plotted as a function of wavelength over the sub-millimetre range (1994). Models of dust grains with no ice mantles (red), with ice mantles 0.5 times the volume of the bare grain (green), and with ice mantles 4.5 times the same volume (blue) are labelled with different colors and symbols. The opacities shown are calculated after 10^5 years of coagulation in gas with densities of 10^5 cm^{-3}, 10^6 cm^{-3}, 10^7 cm^{-3}, and 10^8 cm^{-3}, which are shown in separate curves starting from the bottom respectively. A gas-to-dust mass ratio of 100 is assumed.

-70% and $\sim +30\%$ based on the OH5 model.

Bibliography

Aannestad, P. A. 1975, ApJ, 200, 30

Abergel, A., Boulanger, F., Mizuno, A., & Fukui, Y. 1994, ApJ, 423, L59

Agladze, N. I., Sievers, A. J., Jones, S. A., Burlitch, J. M., & Beckwith, S. V. W. 1996, ApJ, 462, 1026

Alves, J. F., Lada, C. J., & Lada, E. A. 2001, Nature, 409, 159

André, P., & Saraceno, P. 2005, in ESA Special Publication, Vol. 577, ESA Special Publication, ed. A. Wilson, 179–184

Andre, P., Ward-Thompson, D., & Barsony, M. 2000, Protostars and Planets IV, 59

André, P., Men'shchikov, A., Bontemps, S., et al. 2010, A&A, 518, L102

Anglada, G. 1996, in Astronomical Society of the Pacific Conference Series, Vol. 93, Radio Emission from the Stars and the Sun, ed. A. R. Taylor & J. M. Paredes, 3–14

Bachiller, R., Guilloteau, S., Gueth, F., et al. 1998, A&A, 339, L49

Bachiller, R., Martin-Pintado, J., Tafalla, M., Cernicharo, J., & Lazareff, B. 1990, A&A, 231, 174

Bally, J., Devine, D., Alten, V., & Sutherland, R. S. 1997, ApJ, 478, 603

Bally, J., Langer, W. D., Stark, A. A., & Wilson, R. W. 1987, ApJ, 312, L45

Bally, J., Walawender, J., Johnstone, D., Kirk, H., & Goodman, A. 2008, The Perseus Cloud, ed. B. Reipurth, 308

Bazell, D., & Desert, F. X. 1988, ApJ, 333, 353

Beckwith, S. V. W., & Sargent, A. I. 1991, ApJ, 381, 250

Blain, A. W., Barnard, V. E., & Chapman, S. C. 2003, MNRAS, 338, 733

Blake, G. A., Sandell, G., van Dishoeck, E. F., et al. 1995, ApJ, 441, 689

Boudet, N., Mutschke, H., Nayral, C., et al. 2005, ApJ, 633, 272

Buckle, J. V., Hills, R. E., Smith, H., et al. 2009, MNRAS, 399, 1026

Cambrésy, L. 1999, A&A, 345, 965

Cavanagh, B., Jenness, T., Economou, F., & Currie, M. J. 2008, Astronomische Nachrichten, 329, 295

Cernis, K. 1990, Ap&SS, 166, 315

Chandler, C. J., Barsony, M., & Moore, T. J. T. 1998, MNRAS, 299, 789

Chandler, C. J., & Richer, J. S. 2000, ApJ, 530, 851

Chapin, E. L., Berry, D. S., Gibb, A. G., et al. 2013, MNRAS, 430, 2545

Chiang, H.-F., Looney, L. W., & Tobin, J. J. 2012, ApJ, 756, 168

Choi, M., Kang, M., Tatematsu, K., Lee, J.-E., & Park, G. 2011, PASJ, 63, 1281

Connelley, M. S., Reipurth, B., & Tokunaga, A. T. 2008, AJ, 135, 2496

Currie, M. J. 2013, in Astronomical Society of the Pacific Conference Series, Vol. 475, Astronomical Data Analysis Software and Systems XXII, ed. D. N. Friedel, 341

Curtis, E. I., Richer, J. S., & Buckle, J. V. 2010a, MNRAS, 401, 455

Curtis, E. I., Richer, J. S., Swift, J. J., & Williams, J. P. 2010b, MNRAS, 408, 1516

de Zeeuw, P. T., Hoogerwerf, R., de Bruijne, J. H. J., Brown, A. G. A., & Blaauw, A. 1999, AJ, 117, 354

Dempsey, J. T., Friberg, P., Jenness, T., et al. 2013, MNRAS, 430, 2534

Di Francesco, J., Myers, P. C., Wilner, D. J., Ohashi, N., & Mardones, D. 2001, ApJ, 562, 770

Drabek, E., Hatchell, J., Friberg, P., et al. 2012, MNRAS, 426, 23

Draine, B. T. 2003, ARA&A, 41, 241

Draine, B. T., & Lee, H. M. 1984, ApJ, 285, 89

Dupac, X., Bernard, J.-P., Boudet, N., et al. 2003, A&A, 404, L11

Enoch, M. L., Evans, II, N. J., Sargent, A. I., & Glenn, J. 2009, ApJ, 692, 973

Enoch, M. L., Evans, II, N. J., Sargent, A. I., et al. 2008, ApJ, 684, 1240

Erickson, E. F., Knacke, R. F., Tokunaga, A. T., & Haas, M. R. 1981, ApJ, 245, 148

Evans, II, N. J., Rawlings, J. M. C., Shirley, Y. L., & Mundy, L. G. 2001, ApJ, 557, 193

Evans, II, N. J., Dunham, M. M., Jørgensen, J. K., et al. 2009, ApJS, 181, 321

Friesen, R. K., Johnstone, D., Naylor, D. A., & Davis, G. R. 2005, MNRAS, 361, 460

Goldsmith, P. F., Bergin, E. A., & Lis, D. C. 1997, ApJ, 491, 615

Griffin, M. J., Abergel, A., Abreu, A., et al. 2010, A&A, 518, L3

Gutermuth, R. A., Megeath, S. T., Myers, P. C., et al. 2009, ApJS, 184, 18

Hatchell, J., & Dunham, M. M. 2009, A&A, 502, 139

Hatchell, J., Richer, J. S., Fuller, G. A., et al. 2005, A&A, 440, 151

Hatchell, J., Wilson, T., Drabek, E., et al. 2013, MNRAS, 429, L10

Henning, T., Michel, B., & Stognienko, R. 1995, Planet. Space Sci., 43, 1333

Herbig, G. H. 1974, Lick Observatory Bulletin, 658, 1

—. 1998, ApJ, 497, 736

Herbig, G. H., & Jones, B. F. 1983, AJ, 88, 1040

Herbst, W. 2008, Star Formation in IC 348, ed. B. Reipurth, 372

Hildebrand, R. H. 1983, QJRAS, 24, 267

Hirota, T., Bushimata, T., Choi, Y. K., et al. 2008, PASJ, 60, 37

Holland, W. S., Bintley, D., Chapin, E. L., et al. 2013, MNRAS, 430, 2513

Jenness, T., Berry, D., Chapin, E., et al. 2011, in Astronomical Society of the Pacific Conference Series, Vol. 442, Astronomical Data Analysis Software and Systems XX, ed. I. N. Evans, A. Accomazzi, D. J. Mink, & A. H. Rots, 281

Jenness, T., Cavanagh, B., Economou, F., & Berry, D. S. 2008, in Astronomical Society of the Pacific Conference Series, Vol. 394, Astronomical Data Analysis Software and Systems XVII, ed. R. W. Argyle, P. S. Bunclark, & J. R. Lewis, 565

Jenness, T., & Economou, F. 2014, ArXiv e-prints, arXiv:1410.7509

Jennings, R. E., Cameron, D. H. M., Cudlip, W., & Hirst, C. J. 1987, MNRAS, 226, 461

Johnstone, D., & Bally, J. 1999, ApJ, 510, L49

Johnstone, D., Boonman, A. M. S., & van Dishoeck, E. F. 2003, A&A, 412, 157

Jørgensen, J. K., Johnstone, D., van Dishoeck, E. F., & Doty, S. D. 2006a, A&A, 449, 609

Jørgensen, J. K., Harvey, P. M., Evans, II, N. J., et al. 2006b, ApJ, 645, 1246

Kauffmann, J., Bertoldi, F., Bourke, T. L., Evans, II, N. J., & Lee, C. W. 2008, A&A, 487, 993

Keene, J., Hildebrand, R. H., Whitcomb, S. E., & Harper, D. A. 1980, ApJ, 240, L43

Kelly, B. C., Shetty, R., Stutz, A. M., et al. 2012, ApJ, 752, 55

Kirk, H., Johnstone, D., & Di Francesco, J. 2006, ApJ, 646, 1009

Knee, L. B. G., & Sandell, G. 2000, A&A, 361, 671

Kruegel, E., & Siebenmorgen, R. 1994, A&A, 288, 929

Kwon, W., Looney, L. W., Mundy, L. G., Chiang, H.-F., & Kemball, A. J. 2009, ApJ, 696, 841

Lada, C. J., Alves, J., & Lada, E. A. 1996, AJ, 111, 1964

Lada, C. J., Lada, E. A., Clemens, D. P., & Bally, J. 1994, ApJ, 429, 694

Lefloch, B., Castets, A., Cernicharo, J., Langer, W. D., & Zylka, R. 1998, A&A, 334, 269

Liseau, R., Sandell, G., & Knee, L. B. G. 1988, A&A, 192, 153

Luhman, K. L., Rieke, G. H., Lada, C. J., & Lada, E. A. 1998, ApJ, 508, 347

Mannings, V., & Emerson, J. P. 1994, MNRAS, 267, 361

Martin, P. G., Roy, A., Bontemps, S., et al. 2012, ApJ, 751, 28

Mathis, J. S., & Whiffen, G. 1989, ApJ, 341, 808

Mennella, V., Brucato, J. R., Colangeli, L., et al. 1998, ApJ, 496, 1058

Men'shchikov, A., André, P., Didelon, P., et al. 2010, A&A, 518, L103

Miotello, A., Testi, L., Lodato, G., et al. 2014, A&A, 567, A32

Miyake, K., & Nakagawa, Y. 1993, Icarus, 106, 20

Moriarty-Schieven, G. H., Johnstone, D., Bally, J., & Jenness, T. 2006, ApJ, 645, 357

Muench, A. A., Lada, E. A., Lada, C. J., et al. 2003, AJ, 125, 2029

Natta, A., & Testi, L. 2004, in Astronomical Society of the Pacific Conference Series, Vol. 323, Star Formation in the Interstellar Medium: In Honor of David Hollenbach, ed. D. Johnstone, F. C. Adams, D. N. C. Lin, D. A. Neufeeld, & E. C. Ostriker, 279

Ossenkopf, V., & Henning, T. 1994, A&A, 291, 943

Ott, S. 2010, in Astronomical Society of the Pacific Conference Series, Vol. 434, Astronomical Data Analysis Software and Systems XIX, ed. Y. Mizumoto, K.-I. Morita, & M. Ohishi, 139

Pezzuto, S., Elia, D., Schisano, E., et al. 2012, A&A, 547, A54

Pineda, J. E., Arce, H. G., Schnee, S., et al. 2011, ApJ, 743, 201

Planck Collaboration XXV, Abergel, A., Ade, P. A. R., et al. 2011, A&A, 536, A25

Poglitsch, A., Waelkens, C., Geis, N., et al. 2010, A&A, 518, L2

Quillen, A. C., Thorndike, S. L., Cunningham, A., et al. 2005, ApJ, 632, 941

Racine, R. 1968, AJ, 73, 233

Rodríguez, L. F., Anglada, G., & Curiel, S. 1997, ApJ, 480, L125

Rosolowsky, E. W., Pineda, J. E., Foster, J. B., et al. 2008, ApJS, 175, 509

Sadavoy, S. I. 2013, PhD thesis, University of Victoria

Sadavoy, S. I., di Francesco, J., André, P., et al. 2012, A&A, 540, A10

Sadavoy, S. I., Di Francesco, J., Johnstone, D., et al. 2013, ApJ, 767, 126

Sadavoy, S. I., Di Francesco, J., André, P., et al. 2014, ApJ, 787, L18

Sajina, A., Scott, D., Dennefeld, M., et al. 2006, MNRAS, 369, 939

Sandell, G., & Knee, L. B. G. 2001, ApJ, 546, L49

Sandell, G., Knee, L. B. G., Aspin, C., Robson, I. E., & Russell, A. P. G. 1994, A&A, 285, L1

Schnee, S., Mason, B., Di Francesco, J., et al. 2014, MNRAS, 444, 2303

Schnee, S., Rosolowsky, E., Foster, J., Enoch, M., & Sargent, A. 2009, ApJ, 691, 1754

Schnee, S., Enoch, M., Noriega-Crespo, A., et al. 2010, ApJ, 708, 127

Schwartz, P. R. 1982, ApJ, 252, 589

Scoville, N. Z., & Kwan, J. 1976, ApJ, 206, 718

Shetty, R., Kauffmann, J., Schnee, S., & Goodman, A. A. 2009a, ApJ, 696, 676

Shetty, R., Kauffmann, J., Schnee, S., Goodman, A. A., & Ercolano, B. 2009b, ApJ, 696, 2234

Shirley, Y. L., Evans, II, N. J., & Rawlings, J. M. C. 2002, ApJ, 575, 337

Shirley, Y. L., Mason, B. S., Mangum, J. G., et al. 2011, AJ, 141, 39

Shirley, Y. L., Nordhaus, M. K., Grcevich, J. M., et al. 2005, ApJ, 632, 982

Shull, J. M., & Beckwith, S. 1982, ARA&A, 20, 163

Snell, R. L., & Bally, J. 1986, ApJ, 303, 683

Snell, R. L., & Edwards, S. 1981, ApJ, 251, 103

Stahler, S. W., & Palla, F. 2005, The Formation of Stars

Strom, S. E., Vrba, F. J., & Strom, K. M. 1976, AJ, 81, 314

Sun, K., Kramer, C., Ossenkopf, V., et al. 2006, A&A, 451, 539

Swinyard, B. M., Ade, P., Baluteau, J.-P., et al. 2010, A&A, 518, L4

Testi, L., Birnstiel, T., Ricci, L., et al. 2014, Protostars and Planets VI, 339

Ungerechts, H., & Thaddeus, P. 1987, ApJS, 63, 645

van den Bergh, S. 1966, AJ, 71, 990

Walawender, J., Bally, J., Francesco, J. D., Jørgensen, J., & Getman, K. . 2008, NGC 1333: A Nearby Burst of Star Formation, ed. B. Reipurth, 346

Walawender, J., Bally, J., & Reipurth, B. 2005, AJ, 129, 2308

Ward-Thompson, D., & Whitworth, A. P. 2011, An Introduction to Star Formation

Ward-Thompson, D., Di Francesco, J., Hatchell, J., et al. 2007, PASP, 119, 855

Williams, J. P., Blitz, L., & McKee, C. F. 2000, Protostars and Planets IV, 97

Wolfire, M. G., & Churchwell, E. 1994, ApJ, 427, 889

Yang, M., & Phillips, T. 2007, ApJ, 662, 284